UNIVERSITY OF BIRMINGHAM

A NEW STOCHASTIC BACKSCATTER MODEL FOR LARGE-EDDY SIMULATION OF NEUTRAL ATMOSPHERIC FLOWS

JAMES JOSEPH O'NEILL

A thesis submitted to the University of Birmingham for the degree of DOCTOR OF PHILOSOPHY

School of Geography, Earth and Environmental Sciences (GEES)
College of Life and Environmental Sciences (LES)
University of Birmingham
June 2016

Abstract

A stochastic backscatter (SB) approach to subgrid-scale (SGS) modelling for large-eddy simulation (LES) of the neutral atmospheric boundary layer (ABL) has previously been shown to reduce excessive velocity shear, as seen with the popular Smagorinsky SGS model, in the under-resolved surface layer. However, previous SB models exhibit unwanted grid-dependency issues, and the range of atmospheric flows tested remains limited. Here, a new SB model is proposed that uses a grid-adaptive filter to control the length-scale, anisotropy and momentum flux of the backscatter fluctuations, independently of the model grid. Model performance is confirmed to be grid-independent in simulations of the neutral ABL, in which an 80% reduction in excessive near-surface velocity shear is achieved.

The model is also applied to street canyon flow, where the shear layer that separates the recirculating vortex within the canyon from the external flow is again typically under-resolved in most LES set-ups. The backscatter acts to increase momentum transfer across the shear layer, bringing the simulated vortex intensity significantly closer towards wind-tunnel observations. A passive tracer is also released to model traffic emissions, and the pollutant exchange velocity between the canyon and the external flow is again found in better agreement with wind-tunnel data. This information can be used to improve operational urban dispersion models.

For Andreea

Big whorls rise from little whorls

Through merging of the latter,

And big whorls merge to greater whorls

And so on with backscatter.

Acknowledgements

I am enormously grateful to my primary supervisor, Xiaoming Cai, and my secondary supervisor, Rob Kinnersley, for their continued support over these last 3.5 years. Xiaoming, you were always available when I needed help, nurturing towards my academic improvement, and quick and thorough in responding to my (many) queries. Rob, our progress meetings provided the ideal setting for lucid exchanges of thought, and always acted to remind me of the bigger picture of this research.

I am also very grateful to the UK Natural Environment Research Council and the English Environment Agency for their financial support of this research.

I would like to personally thank a few of my fellow research colleagues, namely Tasos Matsikaris for proof-reading much of my work, Mike Grocott for his moral support (mostly through the purchasing of beer), Sally Rangecroft for her thesis tips, and the rest of Room 425 (and adopted others) for countless enjoyable lunch and tea breaks.

The computations described herein were performed using the University of Birmingham's BlueBEAR HPC service (http://www.bear.bham.ac.uk).

Finally, to my family, friends and girlfriend, who supported me at every step along the way, I thank you all from the bottom of my heart.

Table of Contents

List of figures

List of tables

List of symbols

Symbol	Description [units]
$\boldsymbol{a}, a_i$	Backscatter acceleration field (vector, components) [m s^{-2}]
A	Filter weights coefficient
A_{SC}	Area of street canyon opening (in plan-view) [m^2]
α	Constant ($0 \leq \alpha \leq 1$) to control correlation between $\hat{\phi}_x$ and $\hat{\phi}_z$
α_{sgs}	SGS eddy-diffusivity [m^2 s^{-1}]
B_{r}	Theoretical energy backscatter rate [m^2 s^{-3}]
$\hat{B}_{\mathrm{r}}$	Actual (modelled) energy backscatter rate [m^2 s^{-3}]
C_{S}	Smagorinsky constant
C_{ϵ}	Constant in dissipation equation
C_{B}	Backscatter coefficient (momentum)
$C_{\mathrm{B}\theta}$	Backscatter coefficient (scalars)
C	Scalar concentration [$\mu g\ m^{-3}$]
C_0	Quasi-steady scalar concentration [$\mu g\ m^{-3}$]
$\overline{C}_{\mathrm{can}}$	Mean concentration within the street canyon [$\mu g\ m^{-3}$]
Δ	Local grid scale [m]
$\Delta x, \Delta y, \Delta z$	Grid spacing in x, y, z [m]
Δ_{eq}	Equivalent grid scale ($\Delta_{\mathrm{eq}} = (\Delta x \Delta y \Delta z)^{1/3}$) [m]
Δ_{AR}	Grid aspect ratio ($\Delta x / \Delta z$)
Δ_-, Δ_+	Distance to adjacent grid point in –/+ direction [m]
Δt	Model time-step [s]
Δ_{SL}	Surface layer depth [m]
E	Turbulent kinetic energy (per unit mass) [m^2 s^{-2}]
ϵ	Dissipation rate [m^2 s^{-3}]
f	Coriolis parameter [s^{-1}]
$\widehat{\boldsymbol{\phi}}, \hat{\phi}_i$	Filtered random field (vector, components) [m^2 s^{-2}]
$\boldsymbol{\phi}, \phi_i$	Scaled, filtered random field (vector, components) [m^2 s^{-2}]
Φ_{M}	Mean nondimensional velocity shear
g_k	Vertical scaling factor at grid level k

$g_{i,j,k}$	Point-wise scaling factor at grid point i, j, k
$h(x, y, z)$	3-D filter kernel
$h_x(x)$	1-D filter kernel in x
H	Vertical scaling height { Neutral ABL flow: Building height [m]; Street canyon flow: Boundary layer scaling height [m] }
i, j, k	Indices of discrete model grid-points in x, y, z
k	Wave-number
κ	Von-Kármán constant
l	SGS mixing length [m]
l_0	Maximum of l in well-resolved regions [m]
l_f	LES filter width [m]
l_B	Backscatter length-scale [m]
l_B^ζ	Backscatter length-scale component (filter width) in ζ dimension [m]
$\hat{l}_\mathrm{B}$	Backscatter length-scale in the flow interior [m]
L_x, L_y, L_z	Domain extent in x, y, z [m]
λ	Tuning parameter of $\mathcal{O}(1)$ to control backscatter length-scale
$\overline{M}_\mathrm{sc}$	Mean pollutant mass within the street-canyon [µg]
$\overline{M}_\mathrm{bg}$	Mean background pollutant mass (outside the street-canyon) [µg]
n	Exponent in SGS mixing length equation
Nx, Ny, Nz	Number of grid points in modelling domain in x, y, z
ν	Kinematic viscosity [$m^2\ s^{-1}$]
ν_C	Molecular diffusivity [$m^2\ s^{-1}$]
ω	Vorticity [s^{-1}]
ω_PE	Primary eddy intensity metric [s^{-1}]
p	Pressure [Pa]
Q_s	Single line-source emission rate [$\mu g\ m^{-1}\ s^{-1}$]
Q	Total line-source emission rate [$\mu g\ m^{-1}\ s^{-1}$]
Q_tot	Total emission rate [$\mu g\ s^{-1}$]
$\boldsymbol{r}, r_i$	Random number field (vector, components) [$m^2\ s^{-2}$]
Re	Reynolds number
ρ	Density [$kg\ m^{-3}$]

$\rho_{i,j,k}^{\Delta x}$	Autocorrelation coefficient between $\hat{\phi}^{i,j,k}(x,y,z)$ and $\hat{\phi}^{i,j,k}(x+\Delta x,y,z)$
S	Shorthand for $(\Phi_{\mathrm{M}})_{\max}$
S_{ij}	Rate-of-strain tensor [s^{-1}]
$S_{\Delta z}$	Vertical grid stretch factor
Sc	Schmidt number
Src	Scalar source term [$\mu g\ m^{-3}\ s^{-1}$]
σ_i	Turbulent SGS scalar fluxes [$\mu g\ m^{-2}\ s^{-1}$]
σ_X, σ_X^2	Standard deviation, variance of property X
t	Time [s]
T	Reference time-scale [s]
T_{B}	Backscatter timescale [s]
τ	'e-folding' time-scale [s]
τ_{tr}	Transition period time-scale in SC flow [s]
τ_{ij}	Turbulent SGS stress tensor [$m^2\ s^{-2}$]
u, v, w	Velocity components in x, y, z [$m\ s^{-1}$]
u_*	Friction velocity [$m\ s^{-1}$]
$u'_{i_{\mathrm{B}}}$	Backscatter velocity fluctuation in x_i dimension [$m\ s^{-1}$]
$\overline{u'_i u'_j}_B$	Backscatter stresses [$m^2\ s^{-2}$]
U_{ref}	Reference velocity scale [$m\ s^{-1}$]
U_{g}	Geostrophic wind speed [$m\ s^{-1}$]
U_∞	Far-field free-stream velocity in SC flow [$m\ s^{-1}$]
v_{sgs}	SGS eddy-viscosity [$m^2\ s^{-1}$]
v_{e}	Pollutant exchange velocity [$m\ s^{-1}$]
V	Volume of street canyon (below roof-level) [m^3]
$\mathrm{VMF}_{\mathrm{B}}$	Backscatter vertical momentum flux factor
w_ξ	Filter weight at distance ξ normalised by its filter coefficient
W_ξ	Filter weight at grid point at distance of ξ from filter centre
W	Street width [m]
x, y, z	Streamwise, spanwise and vertical directions [m]
$\overline{X}$	Overbar denotes a time average of property X

$\langle X \rangle$	Angled brackets denote a horizontal average of property X
X'	Prime denotes fluctuation about mean of property X
ξ	Distance from filter centre [m]
ξ_-, ξ_+	Lower and upper bound of Gaussian function integral [m]
z_0	Surface roughness [m]
z_1	Height of lowest model grid level [m]
$z_{\mathrm{B_{max}}}$	Maximum height of backscatter acceleration field [m]
ζ_f	Location of filter centre in ζ dimension [m]

List of abbreviations

Abbreviation	Description
§	Section
1-D / 2-D / 3-D	One/Two/Three-dimensional
ABL	Atmospheric boundary layer
ACH	Air exchange rate [$m^3 s^{-1}$]
BC	Boundary condition
CA	Cellular automaton
CFD	Computational fluid dynamics
CFL	Courant–Friedrichs–Lewy
CPU	Central processing unit
DNS	Direct numerical simulation
DRM	Dynamic reconstruction model
ECMWF	European Centre for Medium-Range Weather Forecasts
EDQNM	Eddy-damped quasi-normal Markovian
GCM	General circulation (or global climate) model
LAM	Limited area model
LASD	Lagrangian-averaged scale-dependent
LES	Large-eddy simulation
MT92	Mason and Thomson (1992)
N/A	Not applicable
NBA	Non-linear backscatter anisotropy
NWP	Numerical weather prediction
PCH	Pollutant exchange rate [$\mu g\ s^{-1}$]
PE	Primary eddy
PGF	Pressure gradient force
RAMS	Regional Atmospheric Modelling System
RANS	Reynolds-averaged Navier–Stokes
RL	Roof level
RMS	Root-mean-square
RS-TKE	Resolved-scale turbulent kinetic energy

SB	Stochastic backscatter
SC	Street canyon
SGS	Subgrid-scale
SKEB	Stochastic kinetic energy backscatter
SMAG	Smagorinsky
TKE	Turbulent kinetic energy
VMF	Vertical momentum flux
WRF	Weather Research & Forecasting
WM08	Weinbrecht and Mason (2008)
WT	Wind-tunnel
w.r.t.	With respect to

1. INTRODUCTION

A deeper knowledge of atmospheric motion offers a number of significant benefits. Among others, it guides our ability to predict future weather events, aids our placement of wind turbines for energy production, and improves our understanding of pollutant transport and dispersion after emission. The physical processes that govern the evolution of atmospheric motion are already well understood, and the set of equations that underpin these processes are thought to be comprehensive and accurate. Unfortunately, however, this set of equations consists of nonlinear partial differential equations (including the Navier–Stokes equations) that have no known analytical solution. As a result, atmospheric modellers are forced to use numerical methods to approximate solutions on discretised model grids. The nonlinear nature of the atmosphere also means that kinetic energy is continuously transferred across the various scales of motion, in a process known as the *energy cascade*. Thus, in order to faithfully reproduce the exact evolution of any atmospheric state, all scales of motion – from the largest planetary scale to the smallest molecular scale – must be simulated simultaneously. Clearly, the grid resolution required for such a simulation is unfeasible for any modern-day, or future, computer.

As a consequence, atmospheric modellers must decide *a priori* the most important range of scales (which will be situation-dependent) that are to be explicitly resolved by their model; the upper bound of this range is set by the extent of the modelling domain, and the lower bound by the model's grid resolution. The influence of any scales greater than the largest resolved scales must then enter the simulation by way of appropriate boundary conditions, and the influence of all scales smaller than the smallest resolved scales – the so-called *subgrid scales* (SGS) – must be parameterised by the SGS model. The work undertaken in this thesis

looks to improve an SGS model used for simulating neutral atmospheric flows from the *boundary-layer scale* down to the *urban micro-scale*. This range of scales is particularly important to us as humans. The atmospheric boundary layer (ABL), defined by Stull (1988) to be the lowest part of the atmosphere that is directly influenced by the presence of the earth's surface, is the region in which we all live and breathe. The urban micro-scales encompass the flow patterns found within the urban canopy layer, where the *street canyon* forms the main building block (Oke, 1987). The World Health Organisation (WHO, 2015) estimates that over half the world's population currently lives in urban areas (a fraction that is set to continue to rise), and so a firm knowledge of how the urban environment affects atmospheric flow and pollutant dispersion is also important.

The boundary-layer and urban micro-scales both fall within the broader *turbulence scales*, in which individual atmospheric motions, or *eddies*, are fully three-dimensional (3-D) (as opposed to, for example, the synoptic scale, in which individual structures such as cyclones and anticyclones are quasi 2-D). From the boundary-layer scale to the urban micro-scale, pollutant dispersion will thus be large in both the horizontal and the vertical directions. There are a number of available flow-field and dispersion models for simulating pollutant dispersion at these scales, which cover a range of complexities. Operational models, which must be cost- and time-effective, typically opt for a lower-complexity approach, in which 'bulk' parameters determine the level of mixing by atmospheric processes. For example, the Gaussian plume approach, often used for boundary-layer-scale dispersion modelling (e.g. ADMS, Carruthers *et al.* (1994)), adopts a bulk parameter to describe plume spread, and the box-model approach, often used for street canyon dispersion modelling (e.g. OSPM, Berkowicz (2000)), adopts a bulk parameter to describe the pollutant mass exchange between the air within the canyon and the boundary-layer atmosphere above it. At the higher end of model complexity spectrum lies

the computational fluid dynamic (CFD) modelling approach, in which a numerical solution to the (smoothed) momentum equations is sought directly.

Large-eddy simulation (LES) is a subset of CFD modelling in which all the turbulent scales of motion that can be explicitly resolved by the model grid are prognosed (in space and time). Another, less computationally expensive, approach known as Reynolds-averaged Navier–Stokes (RANS) parameterises *all* turbulence scales in order to obtain the mean flow-field solution. Although LES requires substantial computational resources that are typically unavailable to operational modellers, it remains a very useful tool in terms of: (i) increasing our understanding of turbulent processes by offering far greater spatiotemporal coverage than that possible by field or laboratory experiment, and (ii) guiding our choice of input parameters for the simpler operational models through calculated bulk statistics from its numerical output. The importance of improving the accuracy of LES is therefore made apparent.

Simulation accuracy is particularly dependent on the SGS model, which must faithfully parameterise the effect of all interactions between the resolved scales of motion and the subgrid (unresolved) scales. The *net* effect of these interactions is to drain energy from the resolved scales to the unresolved scales, and many SGS models, including the Smagorinsky (1963) model (the most popular SGS model in use in LES today), only seek to represent this net energy drain. However, this net drain is in fact the result of many forward-scatter events (energy transfer from resolved to unresolved scales) and *backscatter* events (energy transfer from unresolved to resolved scales), which typically occur with similar frequency in any given turbulent flow-field (Geurts, 2004). In many situations, the simplified ‘net drain’ approach adopted by, e.g., the Smagorinsky model can still produce adequate simulation accuracy; however, in other cases – in particular, the cases where backscatter at the grid scale is large – simulation accuracy can be significantly compromised.

As a result, more sophisticated SGS models that attempt to represent the forward and backscatter processes separately have also been proposed. One notable approach, pioneered by Mason and Thomson (1992), uses additional *stochastic* motions to 'inject' energy back into the flow at the smallest resolved scales, as a way of mimicking these random backscatter events. This approach has already proven very successful in alleviating discrepancies seen in simulation output with the Smagorinsky model for the case of boundary layer flow, due to its ability to represent important grid-scale backscatter occurring in the under-resolved surface layer. However, two research gaps can be identified, namely that: (i) the existing methodologies for the way in which the backscatter energy is stochastically injected into the modelled flow-field suffer from unwanted grid-dependency issues, meaning that there is scope for the implementation of a new and improved methodology; and (ii) applications of the stochastic backscatter (SB) modelling approach have so far been limited to simulations of boundary-layer flow, and not to other scales such as the urban micro-scale, or, to the author's knowledge, to simulations that test the subsequent impact on the dispersion of a passive scalar. Both these research gaps are addressed in this thesis, in which it is shown that a new SB methodology can help improve the dynamics and dispersion characteristics in a number of LES applications, including (finally) a fundamental street canyon flow configuration. It is hoped that this will constitute a first step towards providing a more comprehensive database of improved input parameters for operational street canyon models.

The thesis is organised as follows. This introduction (Chapter 1) provides a general overview of the research topic, and is followed by a more in-depth scientific review of the relevant literature to date, ending with a list of clear research objectives (Chapter 2). The following chapter details the methodology behind the new SB model (Chapter 3). The three chapters that follow then present the results from three different applications of the new SB model. The

first application is to the previously tested case of the neutral ABL (Chapter 4). This is done in order to compare the new SB model's performance with that of previous SB models to assess for improvement; in particular, to test the new model's ability to overcome the grid-dependency issues of the previous models. The second application of the SB model is to the simulation of street canyon flow (Chapter 5), in which model output is compared against that obtained with the Smagorinsky model, using a suitable wind-tunnel dataset for validation. This is followed by a third application of the model, which assesses the subsequent impact on the prediction of traffic-related pollutant dispersion and removal from the street canyon (Chapter 6). Finally, a conclusions section (Chapter 7) summarises the main findings, implications and limitations of the research, as well as suggesting steps for future work.

2. LITERATURE REVIEW

This literature review is structured as follows. Current knowledge of neutral atmospheric flows (including the physical process of backscatter) is first summarised, with particular attention paid to neutral ABL and street canyon flow (§2.1). The fundamentals of LES and SGS modelling are then covered, followed by a summary of previous LES of the neutral ABL and street canyon flow/dispersion, including issues of simulation accuracy related to the SGS model (§2.2). A more detailed look is then taken at the stochastic backscatter SGS modelling approach, including its advantages and disadvantages over other approaches, similar approaches used within other modelling communities, and current issues and research gaps associated with the technique (§2.3). Finally, the specific objectives of the current research project are identified (§2.4).

2.1 Neutral atmospheric flows

2.1.1 Foundations

Before tackling the literature, a brief theoretical overview of neutral atmospheric flows is first provided. In this thesis, the phrase ‘neutral atmospheric flow’ is used to mean a high-Reynolds-number (Re) (i.e. fully turbulent) flow in which there is no heat energy input, and thus the potential temperature is constant everywhere. In this case, the generation of turbulence occurs through velocity shear alone, which results from the interaction of the flow with a surface (or any other source of friction). Although perfectly neutral atmospheric conditions are rarely observed in reality, so-called ‘near-neutral’ conditions occur frequently and the neutral case is thus still regarded as a useful subject of study. It also provides a simplified starting point from which added complexity can be later explored.

If one also assumes a dry and incompressible gas (the latter is typically valid in the lower atmosphere), then the governing equations of motion are completely described by the continuity (conservation of mass) and Navier–Stokes (conservation of momentum) equations. Using tensor notation, these are given (in an inertial frame) by:

$$\frac{\partial u_i}{\partial x_i} = 0, \tag{1}$$

$$\frac{\partial u_i}{\partial t} + u_j \frac{\partial u_i}{\partial x_j} = -\frac{1}{\rho}\frac{\partial p}{\partial x_i} + \nu \frac{\partial^2 u_i}{\partial x_j \partial x_j}, \tag{2}$$

where u_i ($= u, v, w$ for $i = 1, 2, 3$) is the velocity component in the direction x_i ($= x, y, z$ for $i = 1, 2, 3$), t is time, p is pressure, ρ is the air density, and ν is the kinematic viscosity. The second term in Eq. (2), the so-called advection term, is the nonlinear term responsible for momentum transfer across scales, i.e. the energy cascade, which occurs both from larger to smaller scales (forward scatter) and from smaller to larger scales (backscatter – see next section, §2.1.2, for more details).

It is also useful to give a few more equations here, which will be quoted at later points in the thesis. Firstly, the equation for the conservation of a passive scalar released into the flow-field:

$$\frac{\partial C}{\partial t} + u_j \frac{\partial C}{\partial x_j} = \nu_C \frac{\partial^2 C}{\partial x_j \partial x_j} + Src, \tag{3}$$

where C is the scalar concentration, ν_C the molecular kinematic diffusivity, and Src a scalar source term. Secondly, it is possible to use a Reynolds decomposition and the rules of Reynolds averaging to obtain the governing equations for the mean fluid motion (utilising the existence of a spectral gap (Stull, 1988)). The dependent variables are decomposed as $u_i = \overline{u_i} + u_i'$, where the overbar denotes an ensemble average (which, if the flow is

stationary, is equivalent to a time average) and the prime denotes the turbulent fluctuation from this value. Substituting into Eqs. (1) and (2) leads to:

$$\frac{\partial \overline{u_i}}{\partial x_i} = 0, \tag{4}$$

$$\frac{\partial \overline{u_i}}{\partial t} + \overline{u_j}\frac{\partial \overline{u_i}}{\partial x_j} = -\frac{1}{\rho}\frac{\partial \overline{p}}{\partial x_i} - \frac{\partial\left(\overline{u_i{'}u_j{'}}\right)}{\partial x_j}. \tag{5}$$

The final term in Eq. (5) describes the influence of the so-called Reynolds stresses, i.e. momentum fluxes caused by turbulent motions, on the mean flow. For high-Re flows such as in the atmosphere, this is several orders of magnitude larger than the influence of viscous stresses, hence why the term involving ν in Eq. (2) has now been dropped. Finally, a similar Reynolds decomposition for scalars yields:

$$\frac{\partial \overline{C}}{\partial t} + \overline{u_j}\frac{\partial \overline{C}}{\partial x_j} = \overline{Src} - \frac{\partial\left(\overline{u_j' C'}\right)}{\partial x_j}, \tag{6}$$

where $\overline{u_j' C'}$ describes the turbulent scalar flux in the x_j direction.

2.1.2 Backscatter

Backscatter refers to the physical process in which turbulent energy is transferred from smaller to larger scales. This is in contrast to forward-scatter, which refers to the transfer of energy from larger to smaller scales. Backscatter is perhaps conceptually harder to visualise than forward-scatter – it is easier to conceptualise smaller eddies being generated from the shearing of larger eddies, as eloquently described in the poem by Lewis F. Richardson (1920):

Big whorls have little whorls

That feed on their velocity,

And little whorls have lesser whorls

And so on to viscosity.

Although the net effect of turbulence is to drain energy from the larger to the smaller scales, in reality, the frequency of forward and backscatter events occurring within a turbulent flow are typically almost equal (Geurts, 2004). Conceptually, an individual backscatter event may be thought of as two or more small-scale eddies merging to produce larger scales. A riposte to Richardson's poem might therefore read:

Big whorls rise from little whorls
Through merging of the latter,
And big whorls merge to greater whorls
And so on with backscatter.

Although the full 3-D picture is far more complex, backscatter may be demonstrated mathematically using a 1-D spectral representation of turbulence. Consider two simple cosine waves U_1 and U_2, with respective wave-numbers k_1 and k_2, i.e.:

$$U_1 = \cos k_1 x, \tag{7}$$

$$U_2 = \cos k_2 x. \tag{8}$$

Following Pielke (2002), a nonlinear interaction between these two waves can be represented by their product, i.e.:

$$U_1 U_2 = \cos k_1 x \cos k_2 x = \frac{1}{2}[\cos(k_1 + k_2)x + \cos(k_1 - k_2)\, x], \tag{9}$$

i.e. two further waves are produced, one with a higher wave-number than the original two waves $(k_1 + k_2)$ and, if $k_1 < 2k_2$, one with a lower wave-number than the original two waves $(k_1 - k_2)$. In the latter case, energy has been transferred from smaller to larger scales, i.e. backscattered. Again, the above analysis only serves as a simplified example of upscale

energy transfer; in reality, backscatter within a 3-D turbulent flow-field is a result of a triple interaction between two smaller-scale eddies and a larger-scale one (Schumann, 1995).

Chasnov (1991) provided a clear demonstration of backscatter in his direct numerical simulation (DNS) of freely decaying turbulence. The relevant figure from this paper, reproduced below (Figure 2.1), shows how the turbulent kinetic energy (TKE) spectrum changes with time. As there is no turbulence generation, the total TKE in the system must be decreasing with time due to viscous dissipation, i.e. the area under the TKE curve, $E(k,t)$, when plotted on linear axes (rather than logarithmic axes, as here) must decrease with time. If only forward-scatter was occurring in the flow, one would expect to see the energy at the largest scales decrease with time as the forward cascade transferred energy across to the smaller scales. However, it is seen that the redistribution of energy occurs in both the forward direction, resulting in the well-known $k^{-5/3}$ spectrum at the smaller scales (Kolmogorov, 1941), as well as the reverse direction (backscatter), giving a tendency towards a k^4 spectrum at the larger scales. The above experiment provides an empirical demonstration of backscatter. However, it is also possible to demonstrate analytically that backscatter occurs across a given length-scale via the theoretical equation for the resolved-scale energy budget, which contains one distinct term describing the drain of energy to smaller scales and another distinct term describing the reverse energy transfer (i.e. backscatter) process (Leslie and Quarini, 1979).

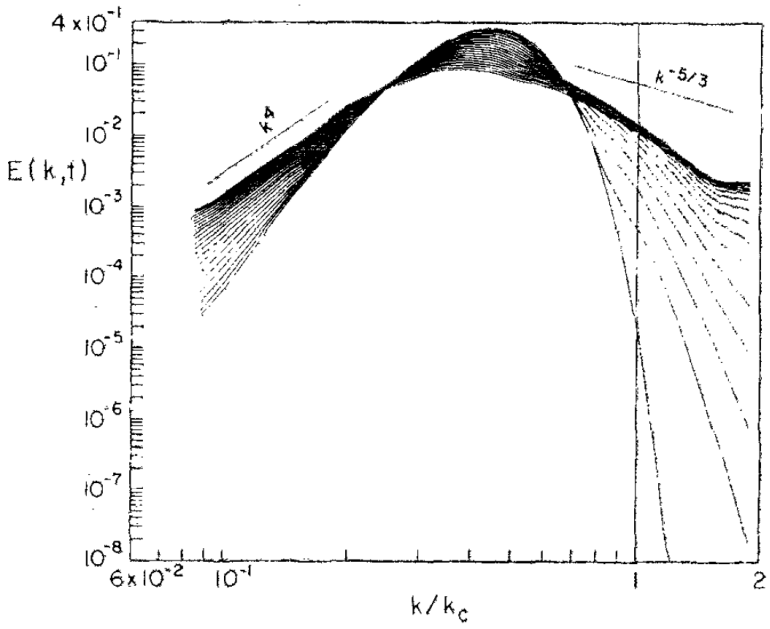

Figure 2.1 – Demonstration of backscatter from DNS
Taken from Chasnov (1991), Fig. 2: "Time evolution of the energy spectrum computed from the DNS of freely decaying turbulence. Time steps 0-200 by 10 [later curves tend towards k^4 and $k^{-5/3}$ spectrum at low and high k respectively]; [cut-off wavenumber] $k_c = 16$."

Consider the 'cut-off' wave-number k_c shown in Figure 2.1 with the vertical line. Schumann (1995) notes that the backscatter contribution from scales of motion smaller than k_c (i.e. larger wave-numbers) falls off with k^{-6}; this means that only those scales of motion that are slightly smaller than k_c contribute to the backscatter across that wave-number. Work has been done to try to quantify the magnitude of backscatter across smaller-scale wave-numbers (i.e. within the 'inertial subrange' - see §2.2.1 for more details). Leslie and Quarini (1979) showed that, in isotropic turbulence, the backscatter rate across wave-numbers within this range is proportional to the local dissipation rate, ϵ, (i.e., the net energy flux towards smaller scales), with the constant of proportionality being of order unity but varying with the type of filter (e.g. cut-off, top-hat, Gaussian) used to separate the smaller and larger scales for a given wave-number. For a cut-off filter, they found that the rate of backscatter was given by $B_r = 1.37\epsilon$. Chasnov (1991) also attempted to quantify the backscatter rate for isotropic

turbulence using eddy-damped quasi-normal Markovian (EDQNM) theory, and found a similar relationship with the dissipation rate of $B_\mathrm{r} = 1.4\epsilon$ (for an infinite inertial subrange). Soon after, Mason and Thomson (1992) attempted to quantify B_r for the case of wall-bounded shear flow. Using fairly simplified physical and dimensional reasoning to obtain an estimate for the fluctuating stress gradients, they were able to derive the following relationship:

$$B_\mathrm{r} = C_\mathrm{B}\left(\frac{l}{l_0}\right)^5 \epsilon, \tag{10}$$

where C_B is the so-called backscatter coefficient (of order unity), and l is the mixing length of the sub-filter scales, with a maximum value of l_0. Thus, far from any surface (where $l = l_0$), the direct proportionality between B_r and ϵ, as derived for isotropic flow, is recovered. However, closer to surfaces (where $l < l_0$), the backscatter rate is strongly attenuated (due to the effect of the 5$^{\mathrm{th}}$ exponent). This is consistent, at least in principle, with the previous observation that only scales slightly smaller than the filter scale contribute to backscatter; thus, if these scales are simply not present (due to being suppressed) close to surfaces, then the backscatter there will be negligible.

It is also possible to derive estimates of the backscatter rate across a given length-scale numerically, by performing DNS (i.e. resolving down to the smallest scales of turbulent motion) and then explicitly filtering the DNS data (i.e. averaging the forward and reverse energy contributions over wave-number shells of a specified radius), as done by, e.g., Kosović *et al.* (2002). However, DNS-calculated backscatter estimates often deviate from those predicted by theory (Domaradzki and Saiki, 1997). Furthermore, DNS is restricted to relatively low-Re flows because of the requirement to resolve down to the dissipative scales, and so backscatter-rate estimates for atmospheric (high-Re) flows are not practically possible.

2.1.3 The neutral ABL

The neutral ABL is an example of a wall-bounded turbulent shear flow. Hinze (1972) and Davidson (2004) both provide general theoretical summaries for this type of flow, and the theory relating more specifically to the ABL can be found in, e.g. Stull (1988) or Garratt (1994). Von Kármán (1931) helped show that within the *surface layer* (the lowest 100m or so) of the neutral ABL, the mean wind profile (over flat terrain) takes the following logarithmic form:

$$U(z) = \frac{u_*}{\kappa} \ln\left(\frac{z + z_0}{z_0}\right), \tag{11}$$

where u_* is the friction velocity, z_0 the surface roughness, and κ the von-Kármán constant. The exact value of κ is debated, and furthermore varies for different types of flow. Businger *et al.* (1971) analysed surface layer observations from the famous measurement campaign in Kansas (1968), suggesting a value of $\kappa = 0.35$ in neutral conditions. Frenzen and Vogel (1995) and Andreas *et al.* (2006) suggest slightly larger values, with an upper limit of $\kappa = 0.41$ proposed by the former. Alternatively, Cai and Steyn (1996) used LES to determine a value of $\kappa = 0.36$.

The logarithmic wind profile provides a similarity condition against which atmospheric modellers often validate their numerical output. This log-profile is obtained by integrating the velocity shear profile, which itself provides an alternative similarity condition:

$$\frac{dU}{dz} = \frac{u_*}{\kappa(z + z_0)}. \tag{12}$$

This is typically rearranged into non-dimensional form to give the normalised velocity shear profile, Φ_M:

$$\Phi_{\mathrm{M}} = \frac{dU}{dz}\frac{\kappa(z+z_0)}{u_*} = 1. \tag{13}$$

Modellers may thus check how closely their profile for Φ_{M} matches the unit profile (Lu and Porté-Agel, 2014); this is a validation tool that will be used for the new SB model later in the thesis (Chapter 4).

2.1.4 Street canyon flow

With over half of the world's population living in urban areas (WHO, 2015), it is important to understand the effects of the densely built environment on wind flow and pollutant dispersion. Street canyons – the gap formed between two rows of buildings either side of a street – form a key constituent part of the urban fabric (Oke, 1988). A street canyon is characterised by the ratio of the building height, H, to the street width, W. Particular concern surrounds the case of vehicular emissions released within deep street canyons ($H/W \gtrsim 1$), which has been observed to lead to poor ventilation, and thus poor air quality, in the real world (DePaul and Sheih, 1985, Xie *et al.*, 2003). An extreme case occurs when the oncoming wind is perpendicular to the street axis; a *skimming flow* regime is established (Oke, 1987), in which the bulk flow passes over the street canyon, leaving pollutants largely trapped within the canyon and thus susceptible to build up to potentially harmful levels (see Figure 2.2(c)). Figure 2.2(a) and (b) also characterise the 'isolated roughness flow' regime (no interaction between adjacent wakes) and 'wake interference flow' regime (some interaction but still distinct), respectively, which can occur in shallower street canyons.

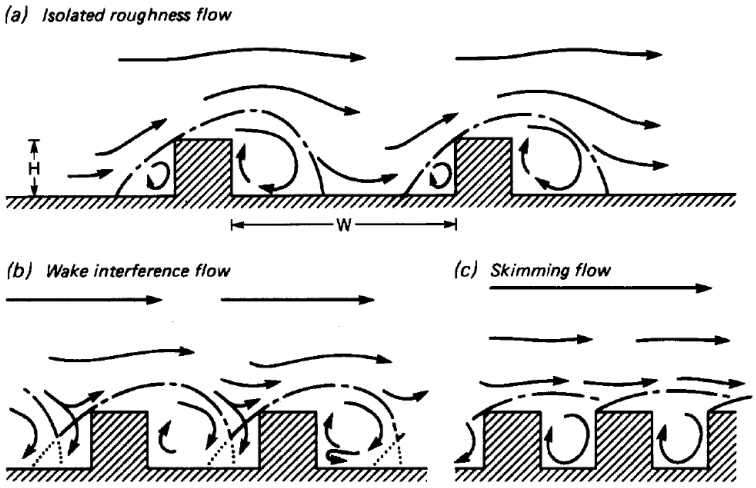

Figure 2.2 – Schematic of skimming flow
Taken from Oke (1988), Fig. 1: "The flow regimes associated with air flow over building arrays of increasing H/W."

In skimming flow, a sharp velocity gradient exists between the relatively fast moving air above the street canyon and the relatively slow moving air inside it. This creates a narrow but energetic shear layer at roof-level, characterised experimentally by a narrow peak in TKE and momentum flux ($\overline{u'w'}$) measurements at that height, e.g. Louka *et al.* (2000), Blackman *et al.* (2015). This shear layer represents a plane mixing layer, as it is formed at the boundary of two co-directional flows of differing speeds (Letzel *et al.*, 2008). Louka *et al.* (2000) analysed the TKE budget equation for neutral flow to reveal that the peak in $\overline{u'w'}$ is a result of a maximum in the shear-production term at roof-level.

The slow-moving air within near-unit-aspect-ratio street canyons typically forms a large-scale rotating vortex that continually recirculates the air (and any pollutants) around the canyon (Lee and Park, 1994, Baik and Kim, 1999, Huang *et al.*, 2000). In addition to this primary eddy (PE), smaller secondary counter-rotating vortices typically form near the corners of the canyon (Liu and Barth, 2002, Cui *et al.*, 2004). Advective transport by each isolated eddy acts to smooth out local gradients of scalar concentration within them, whilst scalar transport

between each eddy is largely controlled by the slower turbulent diffusion process (Liu and Barth, 2002). For deeper canyons, more than one large-scale eddy can form inside the canyon; these eddies are vertically aligned and counter-rotate with the adjacent eddies (Liu *et al.*, 2004). This results in even poorer ground-level air quality (Zhong *et al.*, 2015), as the decreasing strength of each eddy with decreasing height makes it increasingly more difficult for any pollutants to be transported upward and removed from the canyon (Li *et al.*, 2008b, Li *et al.*, 2009).

2.2 Large-eddy simulation

2.2.1 Foundations

Large-eddy simulation is just one of a number of models used to simulate atmospheric flow. Like most of these models, LES numerically solves the dynamic equations of atmospheric motion (which are essentially universal) on a discretised grid. However, the major differences between LES and the other types of model include the spatio-temporal scales of motion typically simulated, and the processes parameterised. For example, general circulation (or global climate) models (GCMs) employ grids that cover the entire globe and are used to simulate the planetary and synoptic scales (i.e. the largest wavelengths of the atmosphere's kinetic energy spectrum). To resolve these scales, a GCM might typically employ a horizontal grid resolution and model time-step of around 100 km and 30 mins, respectively, whilst the important unresolved processes (subgrid motions, radiation, cloud cover, convection, etc.) must be parameterised. Limited area models (LAMs) employ finer spatio-temporal resolutions to simulate 'intermediate' atmospheric motions (i.e. the mesoscales of the kinetic energy spectrum) over a specific region of the globe. Depending on the flow phenomena of interest, the horizontal grid resolution might typically fall within the range 1-50 km and the model time-step between 1-10 min, and the important subgrid processes must again be

parameterised. LES, on the other hand, is typically used to simulate even smaller regions of the atmosphere (within the boundary layer), in which the turbulence scales dominate. To resolve boundary-layer-scale eddies, for example, a (3-D) grid resolution and model time-step of around of 100 m and 1 second, respectively, might be required. The simulation domain is usually small enough to elicit the assumption of horizontally homogeneity for many atmospheric processes, thus reducing the number of parameterisations required by the model. For example, simulation of the dry neutral ABL requires no parameterisation for thermal or moisture effects.

LES numerically solves the filtered Navier-Stokes and continuity equations on a discretised model grid. The technique was first proposed by Smagorinsky (1963) in the context of general circulation experiments, and later developed by Deardorff (1970a) for application to the neutral ABL. The LES filter separates the larger eddies, which are resolved by the model, from the smaller eddies, which are not resolved and must therefore be parameterised. Formally, the filtering procedure can be regarded as a convolution of the velocity field, $\boldsymbol{u}(\boldsymbol{x},t)$, with the (normalised) filter kernel, G, to produce a filtered velocity field, $\tilde{\boldsymbol{u}}(\boldsymbol{x},t)$:

$$\tilde{\boldsymbol{u}}(\boldsymbol{x},t) = G * \boldsymbol{u}(\boldsymbol{x},t) = \int_{-\infty}^{\infty}\int_{-\infty}^{\infty} \boldsymbol{u}(\boldsymbol{x}',t')G(\boldsymbol{x}-\boldsymbol{x}',t-t')dt'd\boldsymbol{x}', \tag{14}$$

where the symbol $*$ denotes the convolution of one function with another. Application of the LES filter to the governing equations of motion (Eqs. (1) and (2)) gives:

$$\frac{\partial \tilde{u}_i}{\partial x_i} = 0, \tag{15}$$

$$\frac{\partial \tilde{u}_i}{\partial t} + \tilde{u}_j\frac{\partial \tilde{u}_i}{\partial x_j} = -\frac{1}{\rho}\frac{\partial \tilde{p}}{\partial x_i} - \frac{\partial \tau_{ij}}{\partial x_j}, \tag{16}$$

where $\tilde{u}_i$ ($= \tilde{u}, \tilde{v}, \tilde{w}$ for $i = 1, 2, 3$) is now the *filtered* velocity component in the direction x_i ($= x, y, z$ for $i = 1, 2, 3$), $\tilde{p}$ is the *filtered* pressure, and τ_{ij} is the turbulent SGS stress tensor. Again, molecular viscosity is assumed to be negligible compared with the SGS stresses for large-Re flow. Note that the application of the filter to the advection term in Eq. (2) has generated two terms in Eq. (16): the filtered advection term (i.e. the advection of momentum by the resolved velocity field), which is known, and the term involving τ_{ij}, which represents the effects of the unresolved velocity field on the resolved field. Since knowledge of the unresolved velocity field is irrecoverably lost during the filtering process, these effects are unknown and must therefore be parameterised. This is the job of the SGS model, as discussed in the next section (§2.2.2). For the sake of brevity, the tilde (~) is dropped throughout the rest of the thesis (unless stated explicitly); Eqs. (15) and (16) thus become:

$$\frac{\partial u_i}{\partial x_i} = 0, \tag{15a}$$

$$\frac{\partial u_i}{\partial t} + u_j \frac{\partial u_i}{\partial x_j} = -\frac{1}{\rho}\frac{\partial p}{\partial x_i} - \frac{\partial \tau_{ij}}{\partial x_j}. \tag{16a}$$

In addition, the filtered transport equation for a passive scalar C can be solved to represent the dispersion of a passive scalar:

$$\frac{\partial C}{\partial t} + u_j \frac{\partial C}{\partial x_j} = -\frac{\partial \sigma_i}{\partial x_i} + Src, \tag{17}$$

where C is now the *filtered* scalar field, and σ_j are the SGS scalar fluxes, which again must be handled by the SGS model.

The scale of the LES filter that separates the larger eddies from the smaller ones should typically lie within the *inertial subrange* of the TKE spectrum (Geurts, 2004). This range falls between the larger production scales and the smallest dissipation scales (see Figure 2.3,

adapted from Garratt (1994)). Eddies within the production scales are typically highly anisotropic and are formed from the mean flow; they thus contain most of the turbulent energy. This energy is then transferred down to smaller scales via the turbulent cascade, until (at the dissipation scales) individual eddies are small enough that their kinetic energy is converted into internal energy by molecular viscosity (Wallace and Hobbs, 2006). Within the inertial subrange, energy is thus neither input into or removed from the flow, but simply passed across the different scales via eddy interactions. These eddies are typically fairly isotropic. Using dimensional analysis, Kolmogorov (1941) was able to show that the inertial subrange of the TKE spectrum follows a behaviour proportional to $k^{-5/3}$. This, and other aspects of Kolmogorov theory, later helped steer LES modellers towards successful modelling of the unresolved scales (i.e. those smaller than the LES filter – see §2.2.2, 'Subgrid-scale modelling').

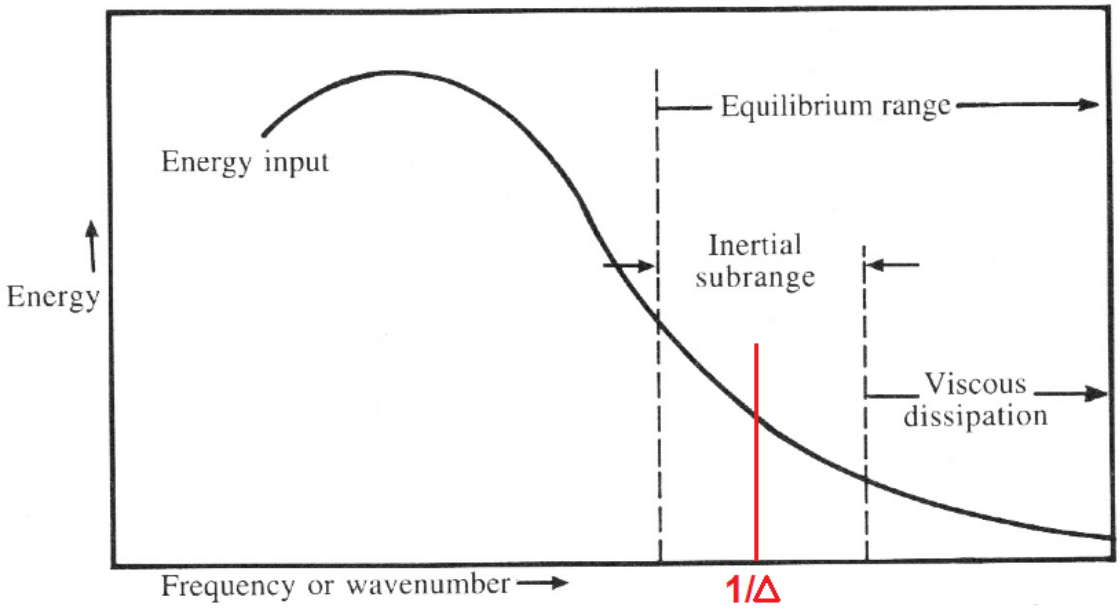

Figure 2.3 – Schematic of TKE spectrum
Adapted from Garratt (1994), Fig. 2.1: "Schematic representation of the energy spectrum of turbulence." The red line indicates a typical 'cut-off' wavenumber for LES, which should ideally lie within the inertial subrange. This wavenumber is the inverse of the LES cut-off wavelength Δ, i.e. the length-scale of the LES filter.

Due to the chaotic nature of the atmosphere, the time evolution of a given flow-field can only be accurately predicted out to a time-scale that scales on that of the largest individual structures within the flow (e.g. cyclones, boundary-layer eddies, etc.). Thus, unlike numerical weather prediction (NWP) which can be expected to predict, with reasonable accuracy, the evolution of synoptic-scale motions over a few days or so, the time evolution of the atmospheric flows that are typically simulated by LES would only be predictable out to a few seconds or minutes. However, this is typically not the purpose of LES; instead, the technique is used to derive time-averaged statistics (over periods much longer than those of the largest eddies) for a given turbulent flow-field. In fact, whilst the accuracy of an NWP forecast is directly dependent on the accuracy of the initial condition, the statistical data derived from LES are independent of the initial condition. LES models are thus typically validated against time-averaged statistical or theoretical profiles rather than the measured instantaneous data.

2.2.2 Subgrid-scale modelling

It is recalled that the purpose of the SGS model in LES is to parameterise the effects of the unresolved scales on the resolved ones. The majority of SGS models are purely dissipative, implying that they seek to represent the net energy drain (from resolved to unresolved scales) rather than forward and backscatter separately (Leslie and Quarini, 1979). This is typically achieved through a 'net' eddy-viscosity, ν_{sgs}, in an analogous way to molecular diffusion. With the popular Smagorinsky (1963) model, the magnitude of ν_{sgs} follows from a local energy balance equation in which quantities on the smallest resolved scales are used to facilitate closure:

$$\tau_{ij} - \frac{1}{3}\delta_{ij}\tau_{kk} = -2\nu_{\mathrm{sgs}}S_{ij}, \tag{18}$$

$$S_{ij} = \frac{1}{2}\left(\frac{\partial u_i}{\partial x_j} + \frac{\partial u_j}{\partial x_i}\right), \tag{19}$$

$$v_{\text{sgs}} = (C_S\Delta)^2\sqrt{2S_{ij}S_{ij}}, \tag{20}$$

where δ_{ij} is the Kronecker delta ($\delta_{ij} = 1$ for $i = j$, $\delta_{ij} = 0$ for $i \neq j$), C_S is the so-called Smagorinsky constant, and $\Delta = (\Delta x \Delta y \Delta z)^{1/3}$ is the local grid-scale. Physically, S_{ij} (the 'rate of strain' tensor) describes the local rate of change of fluid deformation, and is calculated from the resolved velocity field. Thus, in order to close the model, only one parameter (C_S) must be prescribed. Typical values of C_S employed for LES of turbulent atmospheric flows fall within the range 0.1 – 0.2; larger values lead to greater dissipation of energy from the resolved-scale flow, and thus suppress more of the turbulent motions. The isotropic part of the SGS stresses (the 2nd term on the left-hand side of Eq. (18)) is absorbed into the pressure gradient term in Eq. (16). Similarly, the SGS scalar fluxes are modelled using an eddy-diffusivity, α_{sgs}:

$$\sigma_i = -\alpha_{\text{sgs}}\frac{\partial C}{\partial x_i}, \tag{21}$$

$$\alpha_{\text{sgs}} = \frac{v_{\text{sgs}}}{Sc}, \tag{22}$$

where Sc is the Schmidt number; another model parameter. Larger values of α_{sgs} (i.e. smaller Sc) correspond to greater scalar mixing by subgrid motions, thus leading to a more rapidly diffusing scalar within the flow-field. Despite known deficiencies, the Smagorinsky model is often adequate in many simple flows, and remains the most popular choice for SGS modelling due, in part, to its computationally low cost.

The Smagorinsky model is an example of a *first-order* closure, as it parameterises the (unknown) SGS fluxes directly, thus retaining only three prognostic equations (for u, v, w).

Alternatively, it is possible to write down six further prognostic equations for the six unknowns (i.e. the unique components of the tensor $\widetilde{u_i u_j}$, using the tilde again temporarily). However, these equations contain an even larger number of unknowns, $\widetilde{u_i u_j u_k}$; this pattern continues so that an infinite set of prognostic equations would be required to fully describe a turbulent flow – the so-called closure problem (Keller and Friedmann, 1924). Despite this problem, the sophistication of the SGS model still increases with the number of prognostic equations explicitly solved. Thus, second-order SGS models, which parameterise the third moments ($\widetilde{u_i u_j u_k}$) whilst explicitly prognosing the second moments ($\widetilde{u_i u_j}$), typically give more accurate LES than with first-order models. Such models, however, are rarely formulated due to their complexity. One-and-a-half-order SGS models are far more common, e.g. Schumann (1975), Moeng (1984). These models still employ an SGS eddy-viscosity, but solve a further prognostic equation for the SGS energy to calculate its point-wise value; they are thus often referred to as *TKE-1.5* models.

Another method for calculating the point-wise values of ν_{sgs}, proposed by Germano *et al.* (1991), is known as the *dynamic* SGS modelling approach. Dynamic models use a separate explicit 'test' filter, with a width that is slightly larger than that of the LES-filter, to obtain the eddy-viscosity model coefficient (e.g. C_S in Eq. (20)) measured from the smallest resolved scales. The assumption of scale-invariance is then invoked by applying this value of C_S directly to the SGS model. Since the resolved scales vary in space and time, so do the calculated values of C_S, hence the reason for the name 'dynamic model'. As the equation set that must be solved for C_S is over-determined, this later led Lilly (1992) to propose a minimum least-square error method for obtaining C_S. Disadvantages of the dynamic model include the extra computational effort required over the standard Smagorinsky (i.e. constant coefficient) model, as well as the fact that it is possible to obtain negative values of C_S, which

can lead to flow instabilities (Kirkil *et al.*, 2012). Volume averaging of the calculated SGS constants is often performed to reduce the risk of such instabilities, as done, e.g., in the Lagrangian-averaged scale-dependent (LASD) model (Bou-Zeid *et al.*, 2005).

Finally, so-called backscatter SGS models, that *do* attempt to represent the forward and backscatter processes separately, have also been proposed. These are covered in more detail in §2.3 ('Backscatter modelling').

2.2.3 Previous LES of the neutral ABL

LES was first used to simulate the neutral ABL by Deardorff (1970a). This seminal work provided a wealth of information on many aspects of the flow, including the characteristic structure of the large-scale eddies, the effect of varying wind direction on TKE, and variations in the profiles of mean wind, wind shear and other dimensionless turbulence statistics. This was soon followed by the first LES of a dispersing tracer in the neutral ABL (Deardorff, 1972), in which the vertical transportation rate of particles released near the ground was calculated via Lagrangian integrations. Moeng (1984) later continued Deardorff's pioneering work using a new spectral LES code to systematically investigate different turbulent ABL flows. Mason and Thomson (1987) also revisited LES of the neutral ABL, comparing simulations of different grid resolutions in order to assess the dependence of output statistics on the SGS model. It was also shown that the large-scale eddies are elongated in the direction of the mean wind, and that the characteristic eddy size increases with height above the ground.

In well-resolved regions of the ABL, the energy carried by the SGS motions accounts for only a small portion (the exact value of which depends on the grid resolution adopted) of the total available energy, and previous studies have indicated that simulation performance is largely

unaffected by the choice of SGS model in such cases (Mason, 1994). In less well-resolved regions, however, the SGS model carries a more appreciable fraction of the available energy, and the potential consequences of a lack of modelled backscatter can be more severe. Poorly resolved regions in LES should therefore be avoided. However, due to limited computational resources, this is not possible close to solid surfaces, where the characteristic length-scale of the largest eddies becomes increasingly smaller (Mason, 1994).

Numerous LES studies of the ABL have shown that SGS models that do not account for important grid-scale backscatter almost invariably lead to over-prediction of near-surface velocity shear (Mason and Thomson, 1992, Andren *et al.*, 1994, Michioka and Chow, 2008, Kirkil *et al.*, 2012, Talbot *et al.*, 2012). In the neutral surface layer, this is seen as a deviation from the expected logarithmic velocity profile (Eq. (11)), or from the expected constant velocity shear profile (Eq. (12)). Brasseur and Wei (2010) refer to this as the *overshoot* issue, and reference several further examples of studies in which this issue has been observed. The relevant figure from their paper has been reproduced below (Figure 2.4), showing the different profiles of normalised velocity shear, Φ_M, which should equal 1 in the surface layer (see Eq. (13)).

Despite being localised to the near-surface region, any associated simulation deficiencies can be fed up into, and subsequently infect, the larger turbulent length-scales away from the surface, leading to further deterioration in simulation accuracy (Chamecki, 2010). In the surface layer itself, these errors will directly affect the transportation and dispersion of fluxes and scalars, to the detriment of LES-driven dispersion models.

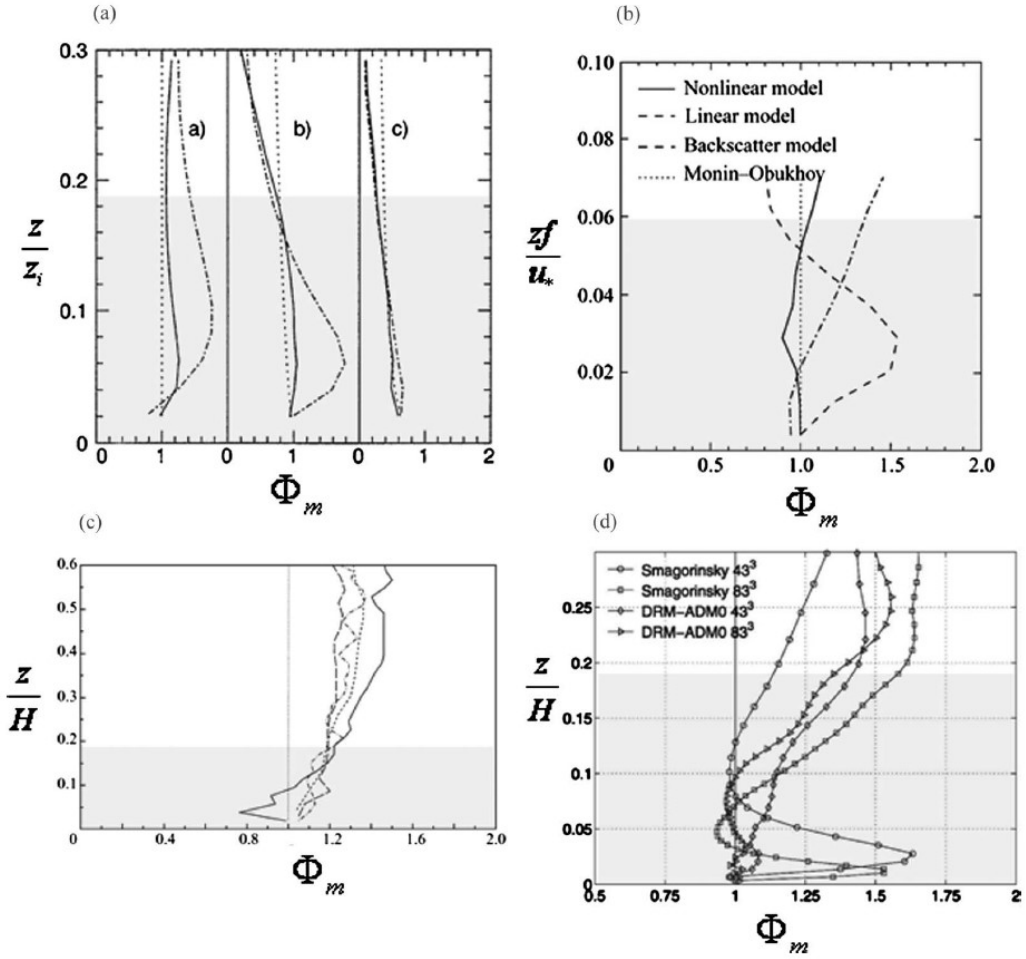

Figure 2.4 – Examples of the 'overshoot'
Taken from Brasseur and Wei (2010), Fig. 1: "Examples of the overshoot in mean shear from previous LES studies: (a) Sullivan *et al.* (1994), (b) Kosović (1997), (c) Porté-Agel *et al.* (2000), and (d) Chow *et al.* (2005). … The shaded regions indicate the surface layer."

Brasseur and Wei (2010) further showed that this overshoot can be reduced with systematic adjustments to the simulation that include increasing the grid resolution (in all 3 dimensions), allowing for more of the turbulence scales to be explicitly resolved, and thus imposing less reliance on the SGS model itself. However, the resolution required to enter the so-called 'high accuracy zone', in which the overshoot becomes negligible, is only computationally feasible for LES of 'engineering-type' flows, in which the Reynolds number is typically much lower than in atmospheric flows. This has prompted atmospheric modellers to seek viable alternatives. As it will be seen in §2.3, SGS models that attempt to account for important

backscatter in the under-resolved surface layer can help significantly alleviate the overshoot problem in simulations of the neutral ABL.

2.2.4 Previous LES of street canyon flow

Street canyon flow and dispersion have been extensively studied by means of controllable simplified experiments, including reduced-scale wind-tunnel (Meroney *et al.*, 1996, Kastner-Klein and Plate, 1999, Pavageau and Schatzmann, 1999, Brown *et al.*, 2000, Simoëns and Wallace, 2008, Salizzoni *et al.*, 2009, Blackman *et al.*, 2015) and water-channel (Baik *et al.*, 2000, Li *et al.*, 2008a, Di Bernardino *et al.*, 2015) testing, as well as numerical CFD modelling (Baik and Kim, 1999, Baik and Kim, 2002, Liu and Barth, 2002, Walton and Cheng, 2002, Cui *et al.*, 2004, Li *et al.*, 2005, Liu *et al.*, 2005, Cai *et al.*, 2008, Cheng and Liu, 2011a, Michioka *et al.*, 2011, Cai, 2012a, Liu and Wong, 2014). CFD models offer a number of advantages over laboratory experiments, including lower set-up and running costs, significantly better spatial coverage, and the ability to test a variety of urban configurations with relative ease. These CFD models must, however, be well validated to instil confidence in their efficacy. They fall into one of two categories: RANS models, which parameterise all turbulence length-scales in search of the mean flow and dispersion patterns; and LES models, which parameterise only the smallest turbulence length-scales (whilst resolving the larger scales) and retrieve the mean spatial patterns by time-averaging the instantaneous model output record (Li *et al.*, 2006). LES is computationally more expensive than RANS but offers greater simulation accuracy.

In particular, LES is well-equipped to model the dynamics of single-recirculation skimming flow, where a largely isolated primary eddy forms within a street canyon of aspect ratio $H/W \approx 1$ when the mean wind is perpendicular to the street axis (Oke, 1987). Unlike the time-averaged RANS modelling approach, used for such flows by, e.g., Baik and Kim (1999)

and Jeong and Andrews (2002), LES is able to capture important unsteadiness in the roof-level turbulence field (Li *et al.*, 2006). The strengths of LES compared with RANS are also demonstrated in many other studies, e.g., Xie and Castro (2006), Dejoan *et al.* (2010), Tominaga and Stathopoulos (2010), Salim *et al.* (2011a) and Salim *et al.* (2011b). Among the first to apply LES to an individual (reduced-scale) street canyon of unity aspect ratio were Liu and Barth (2002); an analysis of subsequent driven scalar transport showed good agreement between predicted mean concentration profiles within the canyon and measured values. Soon after, Cui *et al.* (2004) conducted LES within a full-scale street canyon of unity aspect ratio. Mean normalised streamwise velocity, vertical velocity and resolved-scale turbulent kinetic energy (RS-TKE) profiles, generated at five locations across the canyon, gave a noteworthy reproduction of the main features observed in the corresponding wind-tunnel data of Brown *et al.* (2000). More recently, Cheng and Liu (2011a) and Liu and Wong (2014) utilised larger computing resources to consider 3 and 12 adjacent street canyons, respectively, rather than the one canyon of Cui *et al.* (2004).

A shared deficiency amongst these LES modelling studies of street canyon dynamics, however, is an under-prediction of the PE intensity within the street canyon. Since the background flow is typically prescribed by applying a constant mass flow rate above the canopy level, the total momentum flux within the street canyon comes entirely from the free-stream flow above it; this deficiency thus indicates insufficient entrainment of high-momentum air across the roof-level shear layer. Given that LES is well validated in its representation of turbulence scales that are not too close to either the domain size or the grid resolution (Mason, 1994), it is likely that the LES models are failing to accurately represent either (or both) the large-scale eddies within the free-stream flow that bring momentum into the street canyon via large ‘sweep’ events (Inagaki *et al.*, 2012), or the small (grid-scale and

below) eddies within the roof-level shear layer that mix momentum down into the street canyon via turbulent diffusion (Letzel *et al.*, 2008). The LES domain size limits the size of the large-scale eddies in the free-stream flow; their vertical extent is restricted by the domain lid height and their horizontal extent confined to half the domain width (assuming periodic lateral boundary conditions). Interestingly, however, Cheng and Liu (2011a) and Liu and Wong (2014) observed no significant change in their normalised velocity profiles (and, by inference, in their simulated PE intensity) compared with Cui *et al.* (2004), despite modelling more than one adjacent street canyon (the domain size was also increased in the span-wise and vertical directions). This will have allowed for significantly larger free-stream eddies to form, which suggests that a significant portion of their simulation degradation was attributable to the misrepresentation of the grid-scale (and smaller) eddies.

Improving simulation accuracy of the smaller turbulence scales at roof-level is a challenging task. In this region, the narrow shear layer that exists due to the sharp reduction in streamwise velocity between the fast-moving free-stream air above the street canyon and the relatively slow-moving air within it, continually produces small (yet energetic) eddies through Kelvin-Helmholtz instability (Louka *et al.*, 2000). Very fine grid spacing is therefore required in order to explicitly resolve much of this roof-level turbulence. The LES simulations performed by Letzel *et al.* (2008) suggest that a resolution of at least 100 across-canyon grid points is required in order to explicitly resolve these Kelvin-Helmholtz waves. However, their associated large computational demands necessitated a rather low domain lid height of only $1.5H$. Indeed, the computational resources available to most industrial end-users are typically far smaller than those available to research institutions, and resolution sacrifices are often unavoidable.

In the majority of cases, then, limited computational resources will necessitate the treatment of a significant portion of this roof-level turbulence by the LES's SGS model. The under-prediction of the PE intensity in the aforementioned LES studies suggests that the SGS models used are over-dissipative (i.e. have excessively large SGS viscosities), leading to a lack of turbulent mixing between the free-stream air above and the air within the street canyon (i.e. through the roof-level shear layer). The SGS models used included: the dynamic model (Germano *et al.*, 1991), adopted by Liu and Barth (2002); the Smagorinsky (1963) model, adopted by Cui *et al.* (2004); and the one-equation model (Schumann, 1975), adopted by Cheng and Liu (2011a) and Liu and Wong (2014).

It is noted that none of these SGS models are able to *directly* model the effects of backscatter. In theory, dynamic models are able to account for 'partial' backscatter through locally reduced eddy viscosities, which act to reduce the energy drain from the resolved scales. However, the only way to account for 'strong' backscatter is by imposing locally negative eddy-viscosity values (i.e. local energy input to the resolved scales), whereas in practice, negative values are typically prohibited to avoid numerical instability, e.g. Basu and Porte-Agel (2006). As discussed by Mason and Thomson (1992), backscatter is most significant in regions of the flow where small (grid-scale) but energetic eddies are present. Such eddies are also present in the under-resolved roof-level shear layer, and backscattered energy is thus also likely to be large here. A research gap that therefore exists is to test whether a SGS model that *can* model backscatter directly could help improve the simulation accuracy of street canyon flow.

Just as LES provides important advantages over RANS for street canyon flow-field modelling, the same is true for related dispersion modelling. For example, Walton and Cheng (2002) compared the performance of RANS and LES for simulating pollutant dispersion in a

street canyon of unity aspect ratio and found the LES results to be in much better agreement with a wind-tunnel pollution dataset. This was again due to the model's ability to capture important unsteadiness in the canyon's primary recirculating vortex, which was observed to lead to puffs of pollution being intermittently ejected from the canyon rather than being steadily dispersed away, as simulated by RANS. The dominating influence of intermittent events on tracer release from a street canyon was also observed in the wind-tunnel experiment of Simoëns and Wallace (2008), who concluded that a simple mean concentration gradient model applied to the Reynolds-averaged transport equation would be insufficient to model scalar fluxes. For these reasons, LES is often used to generate databases of input parameters for simpler urban-scale operational (e.g. Gaussian plume or box-model) dispersion models (Vardoulakis *et al.*, 2003).

Even within the LES framework, careful attention is required to ensure optimal simulation accuracy. Again, the choice of SGS model can have a significant impact on the simulation's dispersion characteristics. Letzel *et al.* (2008) showed that the Kelvin-Helmholtz waves generated within the roof-level shear layer, whose dynamics are typically largely handled by the SGS model due to computational limitations, can significantly affect the behaviour of a dispersing tracer. Again, since backscatter is a potentially important process within the under-resolved roof-level shear layer, there is a strong argument to say that it should be explicitly considered in the SGS model. In the next section, the different approaches by the SGS modelling community towards accounting for backscatter are reviewed.

2.3 Backscatter modelling

The apparent need to account for important backscatter across the LES cut-off scale in certain atmospheric regions has led to the formulation of a variety of backscatter SGS models, each offering a different approach to the problem. These models may be categorised into one of

two types; deterministic and stochastic. Deterministic models calculate the subgrid stresses and fluxes using only the information stored on the model grid (and fixed parameters). Thus, given an initial model state, the simulation is uniquely determined. Conversely, stochastic models incorporate randomly generated data into their calculation of the subgrid stresses and fluxes, and so every simulation (even those with the same initial state) will be different. Each type is discussed in turn below.

2.3.1 Deterministic backscatter models

The dynamic SGS modelling approach (Germano *et al.*, 1991), which allows the constant in an eddy-viscosity (e.g. Smagorinsky) model to vary in space and time depending on the local behaviour of the smallest-resolved scales (more details were given in §2.2.2), is often considered partly able to account for backscatter effects. For the case of ABL simulation, a reduced model constant close to the surface essentially allows for more mixing of momentum and a corresponding reduction in vertical velocity shear, which explains why this approach can help alleviate the overshoot issue seen with standard eddy-viscosity models in the neutral surface layer. However, 'strong' backscatter can only be explicitly represented in such models through a locally negative eddy-viscosity, whereas this is typically prohibited in practice (e.g. Basu and Porte-Agel (2006)) as it can lead to the growth of flow instabilities (Kirkil *et al.*, 2012). Dynamic models might therefore be said to allow for 'partial' rather than 'full' energy backscatter, which cannot be simulated with reduced eddy viscosities alone (Schumann, 1995).

The dynamic reconstruction model (DRM) (Chow *et al.*, 2005), in which there is both an eddy-viscosity term (with the model constant dynamically calculated as with 'standard' dynamic models) and a term for the resolved sub-filter scale stress derived using a deconvolution method and assuming scale-similarly, is also able to capture energy

backscatter. However, use of this scheme has been reported to result in underprediction of near-surface stress (Kirkil *et al.*, 2012).

Deterministic SGS models accounting for backscatter that are not based on the dynamic model concept have also been proposed. Kosović (1997) formulated the so-called non-linear backscatter anisotropy (NBA) model, in which a backscatter coefficient is used to apportion the stress contribution from both linear and non-linear sources. In effect, this coefficient again acts to vary the dissipative strength of the SGS motions and hence limits the amount of mixing. However, the backscatter coefficient is fixed at a value representative of the average backscatter rate, whereas theory suggests that the point-wise backscatter rate changes significantly within, e.g., a wall-bounded flow. Kirkil *et al.* (2012) compared the performance of the DRM, LASD and NBA models in a simulation of the neutral ABL, using the Weather Research & Forecasting (WRF)-LES model. With all three SGS models, the simulated velocity profile was brought closer to the expected logarithmic profile, with the two dynamic models (DRM and LASD) performing slightly better than the non-linear model (NBA). However, small discrepancies away from the theoretical profile still existed with each model.

Other deterministic SGS models of note include that of Sullivan *et al.* (1994), who suggested a two-part eddy-viscosity approach in which the well-resolved regions of the ABL (above the surface layer) are treated with a 'standard' TKE-1.5 eddy-viscosity model, whereas closer to the surface a RANS-like approach is used, with an explicit contribution from the mean flow (the two models are smoothly blended through the surface layer). Like the dynamic model approach, this reduces the turbulent SGS dissipation near the surface and thus increases local mixing, which acts to alleviate the velocity shear overshoot seen with standard eddy-viscosity models. Domaradzki and Saiki (1997) proposed a model for the nonlinear term in the energy equation that describes the effects of backscatter (in vorticity form) across the LES cut-off

scale. This requires a model for the subgrid vorticity, which is formulated using the similarity concept. Model output was compared to filtered DNS data and found to show good agreement in the case of isotropic turbulence, and reasonable agreement in the case of channel-flow turbulence. However, with the only adjustable parameter in the model being the filter length, the ability to control the backscatter spatially is limited.

2.3.2 Stochastic backscatter models

Unlike deterministic SGS models, stochastic models are able to *directly* mimic the effects of backscatter (i.e. upscale energy transfer) across the LES cut-off scale by imposing random fluctuations in the subgrid stresses that inject energy into the flow at the smallest resolved scales. Since the subgrid scales are, by design, unknown (the information is unavoidably lost during the application of the LES filter), a stochastic approach is also arguably a more natural choice than a deterministic one (Domaradzki and Saiki, 1997). Among the first to apply a stochastic backscatter (SB) approach to LES was Leith (1990), who simulated a plane shear mixing layer by superimposing non-divergent random accelerations on top of the Smagorinsky SGS model. This is equivalent to imposing fluctuations in the subgrid stresses, as the full term that appears in the filtered LES momentum equation (Eq. (16)) is the spatial derivative of these stresses (i.e. $\partial \tau_{ij}/\partial x_j$), which has units of acceleration. He found that his random fluctuations provided the natural seeds from which large-scale turbulent structures grew, without the need of initial random perturbations.

The SB model of Mason and Thomson (1992) (hereafter, MT92) extended the Leith (1990) model concept to be more applicable to LES of the (neutral) ABL. This case was considered because the SGS motions near the ABL surface contain a significant portion of the total energy and thus backscatter there is important. The model proved remarkably successful in reducing the excessive velocity shear within the neutral surface layer as seen with the

Smagorinsky model alone. Andren *et al.* (1994) later compared this SB model against three other non-backscatter SGS models and re-confirmed that only the SB model was able to significantly reduce excessive velocity shear. Westbury *et al.* (2004) also analysed the model against a DNS dataset for turbulent channel flow and found that it was able to represent the physical characteristics of backscatter in the surface layer well. Brown *et al.* (1994) revised the MT92 model for application to the stable ABL by additionally considering buoyancy effects. The revised model was able to faithfully reproduce various theoretical/empirical profiles over a range of stabilities, again providing a marked improvement over equivalent simulations performed without backscatter.

With the MT92 model, the acceleration fields that augment the momentum equation are forced to be divergence-free by taking the curl of a vector potential (since for any vector field $\boldsymbol{A}$, we have the identity $\nabla \cdot (\nabla \times \boldsymbol{A}) = 0$), which ensures that the adjusted LES fields continue to satisfy mass conservation. They are also locally scaled to ensure that the point-wise backscattered energy matches the theoretically expected value (as given by Eq. (10)). However, the model still has its limitations. Firstly, since a new (independent) random field is generated every other model time-step (which is linked to an adopted leap-frog discretisation scheme), the backscatter fluctuations lack a physically appropriate time-scale (although Mason and Brown (1994), and separately Grooms *et al.* (2015), later showed empirically that such lack of physicality in the backscatter time-scale does not seem to greatly affect model performance). Secondly, the length-scale of the backscatter fluctuations is intended to scale on the LES filter width, which is attempted by applying a 3-D 1:2:1 filter to random numbers defined on the model grid. However, this aim is only achieved when an isotropic (or, at most, mildly anisotropic) grid mesh is employed. If using a vertically refined grid (as is customary in LES, especially in the surface layer), application of the 1:2:1 filter in all three dimensions

means that the backscatter length-scale in the wall-normal direction is reduced, which causes an inappropriately high level of anisotropy to be introduced into the backscatter acceleration fields. Practically, this adds disproportionately large backscatter signals to the flow-field in the horizontal (and little in the vertical) plane, leading to a reduction in the ability of the backscatter model to enhance vertical momentum flux and thus smooth out vertical velocity gradients within the surface layer.

This led Weinbrecht and Mason (2008) (hereafter, WM08) to propose a further modification to the MT92 scheme. Their idea was to first generate the backscatter acceleration fields on a secondary isotropic grid (with Δ scaled on the LES filter width in the well-resolved flow interior), followed by an interpolation onto the (anisotropic) model grid. Although this scheme is successful in generating isotropic backscatter fields, and thus gives grid-independent model performance, a couple of new issues arise. Firstly, since the theoretical backscatter rate profile changes sharply in the surface layer, its representation on the sparse isotropic grid is poor. Secondly, the method imposes that the backscatter fluctuations have a fixed length-scale and are spatially isotropic throughout the flow. In reality, however, such spatial uniformity is not always physically appropriate in the surface layer (Kosović, 1997). Although in well-resolved interior regions of the flow one can expect the backscatter from the unresolved scales to be fairly isotropic and grid-scale, conversely, as the surface is approached, the local turbulence production length-scale approaches (and eventually falls below) the LES filter width, and the assumption of isotropy in the subgrid scales is no longer appropriate. In this near-surface region, one would also expect the backscatter anisotropy to vary in accordance with the physical anisotropy of the subgrid scales, and the backscatter length-scale to reduce with the turbulence production length-scale once it falls below the grid scale. Furthermore, the applicability of the model is limited to simple grid geometries in

which the LES filter width is assumed fixed throughout the domain. In practice, however, many urban or engineering flow set-ups make use of local 3-dimensional grid refinement (in contrast to vertical grid stretching alone) in order to ensure computationally efficient resolution of the most important turbulence length-scales. Indeed, even the comparatively simple geometries associated with horizontally homogeneous ABL flow require the resolution of a multitude of scales for accurate simulation, and adaptive mesh refinement techniques have often been adopted in such cases (Vanella *et al.*, 2008). Since, for an implicit LES filter, a locally refined grid mesh implies a spatially varying LES filter width, the backscatter length-scale should also vary in accordance with the local LES filter width. For nested grids (i.e. sudden grid refinement) it might be possible to define a separate isotropic grid within each sub-domain; however, in order to minimise associated commutation errors, the LES filter width is typically varied gradually, either by employing gradual grid refinement (Kravchenko *et al.*, 1996) or by using an explicit filter to decouple the LES filter width from the grid mesh size, which can then be varied smoothly across grid discontinuities (Piomelli *et al.*, 2006). In this case, the WM08 model could not ensure a physically appropriate backscatter length-scale everywhere. The lack of control over the local backscatter length-scale and anisotropy with both the MT92 and WM08 models calls for an alternative method to be sought; this forms one of the main objectives of the current research (see §2.4).

Other SB modelling approaches than those of the MT92-type have also been proposed. For example, Schumann (1995) proposed a scheme that again augments a simple eddy-viscosity model (in this case the Smagorinsky-Lilly model) with fluctuating random fields. However, rather than adding random accelerations to the momentum equation, random stresses are added to the SGS model itself. These stresses are assumed isotropic everywhere, have zero ensemble mean, and are obtained from the product of random velocity fields taken from a

Gaussian distribution and scaled by the SGS kinetic energy. Unlike previous models, Schumann imposed an appropriate time-scale on the random stress fields, choosing one that is proportional to the turnover time of SGS motions. A spatial filter of characteristic length 2Δ is applied to the random velocity fields to mimic the effect of the implicit LES filter on a staggered grid, and the divergence-free condition is ensured using the Poisson equation. This scheme was only tested for isotropic turbulence, and so its ability to improve predictions of near-surface velocity shear profile in simulations of the ABL is unknown. The scheme is again formulated on the assumption of a uniform grid and it is likely that similar issues will arise as with the MT92 model when employing a refined near-surface grid.

Chasnov (1991) also proposed another 'mixed-model' (i.e. an eddy-viscosity term and a separate stochastic forcing term) approach. He used a spectral closure model based on EDQNM theory, which derives the terms of the subgrid model from a representation of the Navier–Stokes equations and thus diminishes the loss of information associated with a model based on the averaged energy equation. The 'Markovian' element stems from the replacement of the time derivative in the deterministic EDQNM model with a simpler algebraic relationship, which ensures the realizability of the energy spectrum over all wavelengths, at the expense of realistic evolution of the larger eddies (Davidson, 2004). Westbury *et al.* (2004) point out that EDQNM-based closures only provide an estimate of backscatter in the flow interior, due to the assumption of isotropic inertial sub-range turbulence, thus limiting their use for wall-bounded flows. Furthermore, such closures are challenging to implement in non-Fourier LES codes.

As well as the ability to improve mean output statistics, the SB modelling approach also has the secondary desirable effect of reducing the so-called 'spin-up' time; that is, the time taken for the simulation to attain a statistically steady state (Mason and Thomson, 1992, Weinbrecht

and Mason, 2008). Typically, when using a deterministic SGS model, it is necessary to add small artificial perturbations to the (initially laminar) flow-field in order to 'kick-start' turbulence. The random accelerations added by an SB model render such perturbations unnecessary. Empirical evidence further suggests that with an SB model, steady-state flow is achieved smoothly without a large transient peak in the (bulk) TKE that is often observed with the Smagorinsky model (Andren *et al.*, 1994). For example, this behaviour was observed by Weinbrecht and Mason (2008), as shown by Figure 2.5 (taken from their paper).

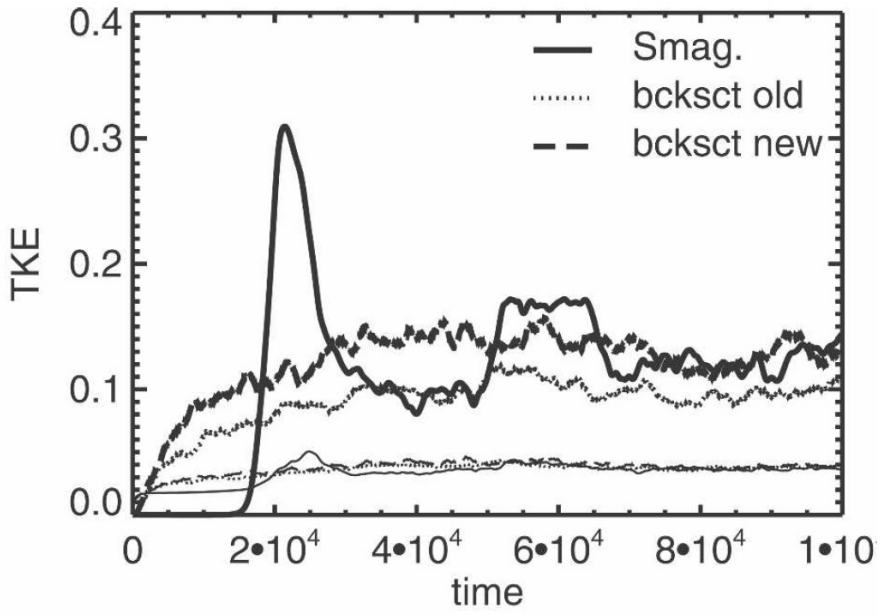

Figure 2.5 – LES spin-up time from bulk TKE
Taken from Weinbrecht and Mason (2008), Fig. 2 (right): "Time series of the TKE in $m^2 s^{-2}$ for the simulations with Smagorinsky–Lilly SGS model and stochastic backscatter. Thick lines represent the resolved TKE and the thin lines the SGS TKE."

Potential disadvantages of the SB modelling approach include the additional computational costs required to generate the stochastic fields, which will increase simulation run-time. For example, Mason and Thomson (1992) report an additional central processing unit (CPU) time increase of 15% with their SB model compared with the use of the Smagorinsky model. However, it could be argued that such costs are justified by the improvement that the SB

model gives to output statistics. Chamecki (2010) notes that while the inability of deterministic SGS models to directly account for backscatter can lead to inaccuracies, such simulations are at least stable, whereas the inclusion of stochastic backscatter carries a risk of inducing model 'blow-up' since excess backscatter can act as a spurious energy source. However, this issue is avoided as long as appropriate backscatter forcing is inserted.

Finally, it is noted that, despite the apparent success of the SB modelling approach for simulations of the ABL, it has yet to be utilised for simulating other types of atmospheric flow. Furthermore, no LES-driven dispersion modelling study has yet utilised an SB SGS model.

2.3.3 SB modelling within other communities

Parameterisations that impose stochastic fluctuations in the SGS stresses in order to model backscatter from the unresolved scales are also in use within other modelling communities due to their associated benefits. For example, modellers within the engineering community (who usually perform LES of lower-Re flows than atmospheric modellers) typically refer to the process of using an SGS model with a deterministic part for forward energy transfer and a separate stochastic part for energy backscatter as the Langevin-equation approach (e.g., Eyink (1996), Gicquel *et al.* (2002)). Similar to atmospheric LES modellers, Laval and Dubrulle (2006) showed that their Langevin-equation SB model gave a better description of the flow than with the use of a standard eddy-viscosity model.

SB models have also been used to improve simulation accuracy at other atmospheric scales. For example, in general circulation modelling, Frederiksen and Davies (1997) noticed that subgrid-scale parameterisations based on deterministic mean damping were unable to maintain consistent large-scale energy spectra and climates with changes in horizontal

resolution and dissipation strength. Realising that the resolved scales are also randomly forced by nonlinear interactions with the unresolved scales, they tested a parameterisation which included both an eddy viscosity part and a stochastic backscatter part, and found that this gave better constancy of the large-scale energy spectra in their simulations of barotropic flow (both non-rotating and differentially-rotating Rossby wave flow). Their scheme utilised EDQNM theory to obtain the eddy damping and stochastic forcing terms. Unlike the SB models described in §2.3.2, their scheme was tailored towards quasi two-dimensional turbulence on the sphere, as appropriate for global circulation patterns, rather than fully three-dimensional turbulence over level ground, as appropriate for boundary-layer flows. Zidikheri and Frederiksen (2009) later incorporated baroclinic instability processes in their stochastic subgrid model, obtaining excellent agreement with higher-resolution simulations.

Stochastic backscatter schemes have also been adapted for use in ensemble NWP models. An argument for the use of stochastic forcings at this scale is that the additional backscattered energy seeks to represent upscale error growth from partially-resolved mesoscale flow phenomena such as deep convection and gravity waves (Shutts, 2005, Berner *et al.*, 2008). Alternatively, the stochastic forcings might be considered a way of combatting excessive dissipation in areas of high numerical diffusion (Shutts, 2009). These stochastic schemes have been shown to increase ensemble member spread, giving a better match to the mean forecast error (Shutts, 2009), and remove the need for arbitrary perturbation of the initial condition. An early advocate of stochastic models in NWP was Palmer (2001) at the European Centre for Medium Range Weather Forecasts (ECMWF), who implemented a so-called cellular automaton (CA) backscatter scheme. This scheme uses a stochastic streamfunction to perturb the flow dynamics; the streamfunction forcing field is obtained from a pattern generator in which the amplitude of the forcing function is (like with the LES schemes) related to the

dissipation rate. The generated patterns are designed to resemble the organisation of convective cloud clusters (Palmer *et al.*, 2009). Berner *et al.* (2008) showed that the CA backscatter scheme, implemented into the ECMWF's coupled ocean-atmosphere model, led to reductions in large-scale systematic model error in the lower and mid-latitudes, as well as significant improvements in seasonal-forecast probabilistic skill for a number of different variables. Shutts (2005) also showed that the scheme helped to correct the form of the energy spectrum towards the expected -5/3 slope at the mesoscales. A stochastic kinetic energy backscatter (SKEB) scheme was later implemented into the Met Office's Unified Model (Bowler *et al.*, 2009, Shutts, 2009), which adds semi-random vorticity perturbations into the forecast in order to offset excessive small-scale damping.

Another related area of active research is that of coupling LES with larger (meso)-scale models so that the latter may be used to drive the simulation, rather than using periodic boundary conditions. With the periodic approach, the flow is typically either maintained via the imposition of a constant pressure gradient force (PGF) across the LES domain, or simply allowed to develop from the initial condition if the momentum loss due to turbulent drag is insignificant during the (short) simulation period. Conversely, with the coupled approach, the flow is actively maintained via the boundary condition, which comes from the mesoscale model output. However, this requires an efficient method for the generation of turbulence at the inflow boundary, which typically only contains mean-wind-field information. Xie and Castro (2008) developed a method based on the discrete filtering of a 2-dimensional slice of random data at the upwind boundary. The filter weights are calculated based on the assumption of an exponential velocity autocorrelation function. The turbulence integral length-scale can vary between prescribed 'zones' to accommodate for variations in the larger-scale flow, and the artificial turbulence fields are also shown to possess Reynolds stresses and

energy spectra that are comparable with periodic-LES turbulence fields. Their scheme also allows for the specification of an appropriate time-scale; it calculates the turbulence field at any one time-step from the field at the previous time-step and a new (independently generated) random field, with the contribution of the previous field also based on the assumption of an exponential time autocorrelation. This scheme was subsequently used in a high-resolution simulation of flow and dispersion within a real-world urban canopy layer – the DAPPLE site, which includes part of Marylebone Road and surrounding streets in central London. In both an oblique wind case (Xie and Castro, 2009) and perpendicular wind case (Xie, 2011) (with respect to Marylebone Road), the numerical results were found to be in reasonable agreement with a wind-tunnel dataset. Kim *et al.* (2013) later proposed a similar scheme that produces divergence-free fields, thereby reducing the unphysically large pressure fluctuations that are observed with the non-divergence-free scheme. Synthetic inflow turbulence schemes that generate 4D data (3D in space and time) have also been proposed, e.g. Klein *et al.* (2003).

Although much can be learned from these turbulence inflow generation schemes, their direct use in stochastic backscatter modelling is unfortunately not possible. This is because the artificial turbulence fields in SB SGS modelling are designed to add energy near the LES cut-off (grid) scale only, whereas, in the inflow turbulence case, the energy across the entire spectrum (from the integral scale to the cut-off scale) must be considered.

2.4 Research objectives

Having reviewed the relevant literature, the specific objectives of the current research project can now be outlined. It was discussed in §2.3.2 how the SB approach to SGS modelling in LES of the neutral ABL has recently been shown to significantly alleviate predictions of excessive velocity shear in the surface layer as seen with the use of the popular Smagorinsky

SGS model. However, it was also noted that the original SB model for neutral ABL flow (MT92) and a later revised version of the model (WM08) both exhibit grid-dependency issues in terms of the way in which the backscatter acceleration fields (that augment the LES momentum equation) are generated: with the MT92 model, the backscatter length-scale and anisotropy depend on the local grid spacing and aspect ratio; with the WM08 model, the backscatter is unavoidably isotropic with uniform length-scale.

This leads to a demand for a new methodology to be developed that allows the local backscatter length-scale and anisotropy to be controlled independently of the model grid. The backscatter length-scale could then be reduced appropriately towards surfaces, and, if necessary, varied to reflect any spatial variations in the LES filter width (due to local changes in grid resolution). The backscatter anisotropy could also be specified in conjunction with the physical anisotropy of the grid-scale motions. The advantages of such a model, and the corresponding limitations of the MT92 and WM08 models, are illustrated in the schematic diagram in Figure 2.6, which shows an example simulation of the neutral ABL in which the LES filter width decreases towards the bottom right corner of the domain as drawn (as a result of smooth grid refinement). It can be seen that in the flow interior, the backscatter is appropriately grid-scale and isotropic for all three models, except for the MT92 model in areas of horizontal grid refinement, where the backscatter becomes unphysically anisotropic due to the dependence of the 1:2:1 filter operation on the local grid spacing. Closer to the surface, the backscatter anisotropy with the new SB model is increased gradually in accordance with an assumed profile of the physical anisotropy of the grid-scale turbulence. With the MT92 model, however, the dependence of the anisotropy on the grid spacing results in regions of unphysically high or unphysically low anisotropy, and with the WM08 model, the backscatter remains isotropic at all distances from the surface. With the new model, the

backscatter length-scale is reduced towards the surface in accordance with the local subgrid turbulence length-scale, and further reduced in refined grid regions to reflect the reduced LES filter width, whereas the length-scale remains fixed at the local grid scale with the MT92 model, and fixed at the coarse grid scale with the WM08 model (resulting in particularly unphysically large structures in the highest refined region).

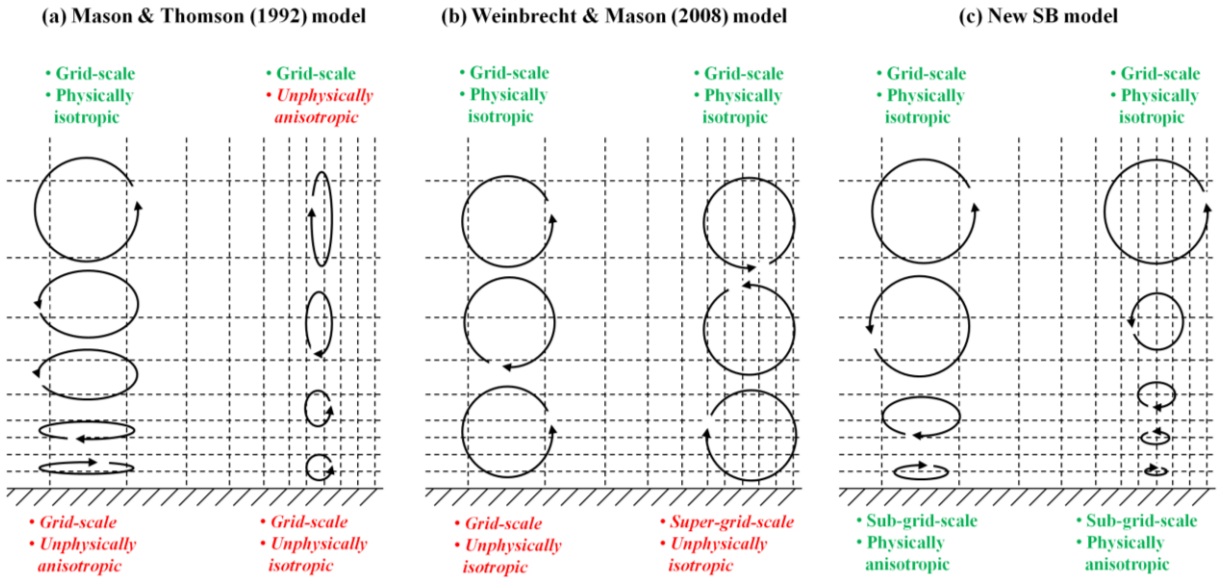

Figure 2.6 – Schematic of new SB model vs. previous models
Schematic showing the characteristic length-scale and anisotropy of backscatter acceleration fields generated using (a) the MT92 model, (b) the WM08 model, and (c) the proposed new SB model. Unphysical inconsistencies are noted in italic red font.

As well as the ability to control the backscatter length-scale and anisotropy, it would also be beneficial to control the backscatter vertical momentum flux (VMF). For a two-dimensional (2-D) mean shear flow, such as the idealised neutral ABL, velocity fluctuations in the third dimension (i.e. that which is horizontally perpendicular to the direction of mean flow) will be uncorrelated with velocity fluctuations in the other two dimensions, i.e. $\overline{u'v'}$, $\overline{v'w'} = 0$ (with the y-axis aligned with this third dimension). The $\overline{u'w'}$ component, however, will be non-zero and thus represents the total VMF. Hinze (1972) provided a full derivation of the dynamic equation for $\overline{u'w'}$ in an incompressible steady-mean shear flow. The fluctuations imparted by

the SB model in under-resolved regions will affect the grid-scale VMF, which in turn will affect the velocity (and velocity shear) profiles in that region.

Simulation of the neutral ABL provides the ideal case study with which to test any new SB model, since (i) theoretical profiles are already known (e.g. the velocity shear profile within the surface-layer as given by Eq. (12)), thus providing a means against which to validate the LES output, and (ii) the performance of the new SB model can be compared against that of the existing (i.e. MT92 and WM08) models, since the neutral ABL was also originally used to validate these models. To verify the grid-independence of the proposed new SB model, a range of grid-anisotropies should be tested. Large aspect ratios are common in LES studies of the ABL, often in order to match the physical anisotropy of surface layer turbulence with the anisotropy of the near-surface grid. Typical grid aspect ratios tested for LES studies of the neutral ABL fall within the range $\Delta_{\mathrm{AR}} = \Delta x/\Delta z = 1$ to 10 (Sullivan *et al.*, 1994, Chow *et al.*, 2005, Mirocha *et al.*, 2012). This range should therefore be covered in the SB model tests.

It was also noted in §2.3.2 that the SB modelling approach for LES of atmospheric flows has so-far been limited to simulations of the ABL. However, as argued in §2.2.4, the approach should also be tested for the simulation of street canyon flow, since under-resolution in the roof-level shear layer (where backscatter is potentially large) is again typically unavoidable in most LES set-ups. In this case, LES output may be validated against wind-tunnel data which have previously been published for various street canyon configurations. To test the effect of including backscatter in the simulation, LES output obtained with the SB model should be compared against LES output obtained without backscatter; since the SB model essentially becomes the Smagorinsky model when the backscatter accelerations that augment the LES momentum equation are set to zero, this will essentially be testing the SB model against the Smagorinsky model.

Finally, it was again noted in §2.3.2 that a research gap also exists to test the effect of an SB model on the dispersion of a passive tracer. If an SB model is shown to improve simulation accuracy in terms of the flow dynamics, it also seems logical to test whether similar improvements are observed for the predicted behaviour of a pollutant released into the flow. Any such improvements could be beneficial to dispersion modellers who use low-cost operational models with parameters derived from LES model output. One such example is street canyon box models that use an estimate for the exchange velocity to describe the mass transfer of traffic-related pollutants released within the street canyon to the external flow.

In light of the above discussion, four research objectives are defined:

Objective #1: Formulate a new methodology for generating the stochastic backscatter acceleration fields that allows for grid-independent control of the backscatter length-scale, anisotropy and momentum flux. This objective is addressed in Chapter 3.

Objective #2: Evaluate the grid-independence of the new SB model by performing LES of the neutral ABL for various grid anisotropies, comparing surface-layer velocity shear profiles against those obtained with the Smagorinsky, MT92 and WM08 SGS models. This objective is addressed in Chapter 4.

Objective #3: Assess whether the new SB model can also help improve simulation accuracy (from that obtained with the Smagorinsky model) of neutral street canyon flow, in which the roof-level shear layer is under-resolved, using a wind-tunnel dataset for validation. This objective is addressed in Chapter 5.

Objective #4: Examine the effect of the SB model on improving LES of the dispersion of a passive tracer inside the street canyon, again comparing simulation accuracy against that

obtained with the Smagorinsky model and using a wind-tunnel dataset for validation. This objective is addressed in Chapter 6.

3. THE NEW STOCHASTIC BACKSCATTER MODEL

3.1 Introduction

This chapter addresses research objective #1, as stated at the end of §2.4 and repeated below for convenience:

> **Objective #1**: Formulate a new methodology for generating the stochastic backscatter acceleration fields that allows for grid-independent control of the backscatter length-scale, anisotropy and momentum flux.

As discussed in §2.3.2, such an SB model is needed due to grid-dependency issues associated with previous SB models of this type. With the MT92 model, the filtering procedure used to generate the SB acceleration fields results in the backscatter fluctuations becoming increasingly less effective (in smoothing out excessive velocity gradients within the neutral surface layer) as vertical grid refinement is increased. With the WM08 model, although the effectiveness of the SB model remains unaffected by changes in vertical grid refinement, the backscatter is unavoidably isotropic with uniform length-scale, which is not always appropriate; its application is also limited to cases in which refined grid spacing is adopted in one dimension only. By formulating a new grid-independent filtering procedure, it should be possible to control the backscatter length-scale so that it can be reduced in appropriate regions of the flow (e.g. close to surfaces, or where the LES filter width is reduced due to local grid refinement), as well as controlling the backscatter anisotropy to be representative of the local grid-scale turbulence anisotropy as inferred, e.g., from field measurements (see Figure 2.6). The ability to control the vertical momentum flux associated with the backscatter fluctuations should also allow for control over the extent to which the SB model encourages additional grid-scale vertical mixing and thus modifies local velocity gradients.

This chapter is structured as follows. Parts of the underlying methodology of the new SB model are based on work originally proposed by Mason and Thomson (1992); these parts are collected and presented in a separate section (§3.2, 'SB model foundations') in order to clearly differentiate them from the novel parts of the new SB model's methodology, which are subsequently detailed in §3.3–3.6. Finally, the abilities and limitations of the new SB model are summarised in §3.7.

It is noted that some of the materials in this section have previously been published in the following peer-reviewed journal articles: O'Neill *et al.* (2015) and O'Neill *et al.* (2016).

3.2 SB model foundations

The new SB model is based on the concept of imposing pseudo-random acceleration fields on top of the LES acceleration fields obtained using the Smagorinsky SGS model (Mason and Thomson, 1992):

$$\frac{\partial u_i}{\partial t} + u_j \frac{\partial u_i}{\partial x_j} = -\frac{1}{\rho}\frac{\partial p}{\partial x_i} + \frac{\partial}{\partial x_j}\left\{\nu_{\text{sgs}}\left(\frac{\partial u_i}{\partial x_j} + \frac{\partial u_j}{\partial x_i}\right)\right\} + a_i, \tag{23}$$

where $a_i = \{a_1, a_2, a_3\}$ is a backscatter acceleration field, and all other symbols are as in Eq. (16) & (20).

Each backscatter acceleration field must be appropriately scaled to inject the desired amount of energy into the LES field, and should ideally be divergence-free to ensure that the adjusted LES fields continue to satisfy mass conservation. The general procedure for obtaining a backscatter acceleration field is:

(i) Generate three gridded fields of uniformly distributed random numbers with zero mean and unit variance, $\boldsymbol{r} = \{r_x, r_y, r_z\}$.

(ii) Apply a filter to each field in order to introduce an appropriate backscatter length-scale and level of anisotropy, generating a set of intermediate fields, $\widehat{\boldsymbol{\phi}} = \{\hat{\phi}_x, \hat{\phi}_y, \hat{\phi}_z\}$. A novel "grid-adaptive" filtering procedure for the new SB model is described in §3.3.

(iii) Scale each field to ensure the appropriate energy backscatter rate throughout the domain, generating another set of intermediate fields, $\boldsymbol{\phi} = \{\phi_x, \phi_y, \phi_z\}$. A novel scaling procedure for the new SB model is described in §3.4.

(iv) Take the curl of the three fields to produce the final, divergence-free (since $\nabla \cdot (\nabla \times \boldsymbol{\phi}) = 0$) acceleration field, $\boldsymbol{a} = \{a_1, a_2, a_3\}$. The vertical momentum flux associated with the final backscatter acceleration fields can be controlled by prescribing a degree of correlation between two of the three (pre-curled) fields – this novel procedure is described in §3.6.

Each backscatter acceleration field lasts for a time period T_B, before a completely new (independent) field is generated. There are no gaps in-between each field, i.e. the backscatter accelerations are added to the LES field at every time-step within each T_B time period. Mason and Brown (1994) demonstrated empirically that, despite having unrealistically high frequency, a value of T_B on the order of the model time-step, Δt, still gives significant reduction in excessive velocity shear, whilst also ensuring Galilean invariance (Pope, 2000). The ensemble-average (denoted by an overbar) change in resolved kinetic energy due to the backscatter accelerations is well approximated by $\Delta E = 1/2 \left(\overline{(u_i + a_i T_\mathrm{B})^2 - u_i^2} \right) = 1/2\ \overline{a_i^2} T_\mathrm{B}^2$ (sum over i); the expanded terms involving $\overline{u_i a_i}$ vanish since a_i has zero mean and is uncorrelated with u_i. Dividing through by T_B and noting that $\overline{a_i^2}$ is simply the variance of a_i, a modelled energy backscatter rate, $\hat{B}_\mathrm{r}$, is thus defined as

$$\hat{B}_{\mathrm{r}} = \frac{T_{\mathrm{B}}}{2}\left(\sigma_{a_1}^2 + \sigma_{a_2}^2 + \sigma_{a_3}^2\right). \tag{24}$$

The theoretical energy backscatter rate derived by Mason and Thomson (1992) for wall-bounded shear flows, as given by Eq. (10), is used. It is repeated below for convenience:

$$B_{\mathrm{r}} = C_{\mathrm{B}}\left(\frac{l}{l_0}\right)^5 \epsilon, \tag{25}$$

where, now more specifically, l is the subgrid-scale mixing length in the Smagorinsky model, with maximum value l_0 in well-resolved interior regions of the flow. Combining Eqs. (24) and (25), the aim is thus to scale each backscatter acceleration field such that

$$\sigma_{a_1}^2 + \sigma_{a_2}^2 + \sigma_{a_3}^2 = \frac{2C_{\mathrm{B}}}{T_{\mathrm{B}}}\left(\frac{l}{l_0}\right)^5 \epsilon. \tag{26}$$

l_0 is taken to be $C_{\mathrm{S}}\Delta$. For anisotropic grids, the 'equivalent grid scale' (Deardorff, 1970b) is used for Δ, namely $\Delta = \Delta_{\mathrm{eq}} = (\Delta x \Delta y \Delta z)^{1/3}$. For grids with vertical refinement only, Δ_{eq} is assumed spatially uniform, with Δz taken as a typical value in the flow interior. For l, the following equation is used to match the near-surface mixing length, which scales on $\kappa(z + z_0)$, to the mixing length in well-resolved regions (Mason and Thomson, 1992):

$$l = \left(\frac{1}{l_0^n} + \frac{1}{\left(\kappa(z + z_0)\right)^n}\right)^{-1/n}, \tag{27}$$

where the exponent n controls how sharply the near-surface mixing length is matched to the value in the well-resolved flow interior.

Mason and Thomson (1992) also outlined an analogous approach to modelling the SGS scalar fluxes, in which the magnitude of backscatter (of variance) is controlled via the scalar backscatter coefficient, $C_{\mathrm{B}\theta}$. However, in preliminary tests performed for the scalar dispersion part of this thesis (Chapter 6), it was empirically found that the inclusion of scalar backscatter

(on top of energy backscatter) gives insignificant differences in calculated mean statistics when the scalar is a dynamically passive tracer (as opposed to, e.g., temperature, which has a dynamical feedback). A value of $C_{B\theta} = 0$ is thus chosen in Chapter 6, i.e. the SGS scalar fluxes are handled entirely by the base Smagorinsky model; this further allows the effects of energy backscatter alone to be discerned.

3.3 New grid-adaptive filter

This section outlines the new filtering procedure used in the generation of the backscatter acceleration fields, which allows the local backscatter length-scale and anisotropy to be controlled independently of the model grid. The procedure utilises a discrete 3-D "grid-adaptive" filter that is applied directly on the model grid, thus removing the need for any interpolation from a secondary grid as with the WM08 model.

3.3.1 Filter kernel

It is first imposed that the 3-D filter is separable, i.e. that it can be constructed from a sequence of convolutions in the three lower dimensions (Wirjadi and Breuel, 2005):

$$h(x, y, z) = h_x(x) * h_y(y) * h_z(z), \tag{28}$$

where, e.g., $h_x(x)$ is the 1-D filter kernel in the x-dimension. The 3-D 1:2:1 filter is an example of a separable filter; the filtered field can be obtained by applying a 1-D filter with weights $A \times [1\ \ 2\ \ 1]$ in the x dimension, then the y dimension, then the z dimension (the coefficient A determines the variance of the resulting field). However, rather than fixing the filter weights (and thus the number of grid points used in the calculation of each filtered value), a physical length-scale (which may vary spatially) is instead defined for each 1-D filter. The number of grid points used in the calculation of any filtered value is then dependent on the local grid spacing in each dimension.

3.3.2 Filter shape

To decide upon the shape of each 1-D filter, one may be guided by the choice of previous models. On an isotropic grid with resolution Δ, it can be shown that the 3-point 1:2:1 filter (used in the MT92 model) and the 5-point 1:4:6:4:1 filter (used in the WM08 model) are both close approximations to the discrete Gaussian filter, with a filter width equal to 0.8Δ and Δ, respectively. These choices of filter reflect the fact that the implicit filtering imposed by the Smagorinsky model on the smallest resolved scales is Gaussian in nature (Sullivan *et al.*, 2003). A Gaussian filter shape is therefore also chosen here, which also facilitates comparison of the results obtained using the new SB model with those obtained using the MT92 and WM08 models. Defining the filter width to be the standard deviation of the Gaussian function (Geurts, 2004), the continuous 1-D filter kernel for the general dimension ζ is given by

$$h_\zeta(\xi) = A \exp\left(-\frac{\xi^2}{2\left(l_\mathrm{B}^\zeta\right)^2}\right), \tag{29}$$

where $\xi = \zeta - \zeta_\mathrm{f}$ is the distance away from the filter centre at ζ_f, l_B^ζ is the filter width for dimension ζ, and the coefficient A controls the variance of the filtered field.

3.3.3 Filter weights

For a discrete Gaussian filter, with which weights are only applied at a finite number of grid points, the weight at a grid point that is a distance of ξ away from the filter centre-point, W_ξ, may be calculated as the integral over the part of the Gaussian function for which that grid point is closest (between ξ_- and ξ_+, say), i.e.:

$$W_\xi = \int_{\xi_-}^{\xi_+} h_\zeta(\xi)\, d\xi = A l_\mathrm{B}^\zeta \sqrt{\frac{\pi}{2}} \left\{ \mathrm{erf}\left(\frac{\xi_+}{l_\mathrm{B}^\zeta \sqrt{2}}\right) - \mathrm{erf}\left(\frac{\xi_-}{l_\mathrm{B}^\zeta \sqrt{2}}\right) \right\}, \tag{30}$$

where erf is the error function, which must be approximated numerically. For a grid with variable grid spacing, $\xi_- = \xi - \Delta_-/2$ and $\xi_+ = \xi + \Delta_+/2$ are taken, where Δ_- and Δ_+ are the distances between the given grid point and the adjacent grid points in the negative and positive ζ direction, respectively. For computational efficiency, the decision is made to restrict the number of grid points at which the filter weights are calculated to those for which $|\xi| \leq 3l_{\mathrm{B}}^{\zeta}$, which ensures that at least 95% of the area under the Gaussian function is accounted for.

For most applications, the coefficient A is chosen to normalise the filter (i.e. make its full integral equal to 1), which ensures that a constant region of an unfiltered flow-field is unchanged after filtering. This is not important here, since there is no useful information contained within the initial random fields, and one may instead choose A to control the variance of the filtered fields. At this stage, the choice is made to maintain unit variance everywhere; an appropriate re-scaling of the fields will be applied at a later step (see §3.4). Given that the unfiltered fields are a random sample of values from the uniform distribution with zero mean and unit variance, then in order to maintain unit variance after filtering, it is required that

$$A = \left(\sum_{\xi} w_{\xi}^2 \right)^{-\frac{1}{2}}, \tag{31}$$

where $w_\xi = W_\xi / A$.

3.3.4 Filter width

The width of each 1-D filter will be guided by the intended local backscatter length-scale, l_{B}. As the aim of an SB model is to mimic backscatter from the unresolved to the resolved scales,

l_B should scale (in well-resolved regions) on the LES filter width, l_f. In most LES codes, the formal filtering procedure (Eq. (14)) is not explicitly carried out (since the continuous velocity field is not known). Instead, the filtering is considered to be carried out implicitly through the representation of the (continuous) dynamical fields in the discretised (in time and space) model. The length of the LES filter width is therefore not well defined, but is likely to scale with the grid resolution, i.e. $l_\mathrm{f}{\sim}\Delta_\mathrm{eq}$, where again, $\Delta_\mathrm{eq} = (\Delta x \Delta y \Delta z)^{1/3}$ is an estimate of the effective grid resolution (Deardorff, 1970b), with Δz is taken as a typical value in the flow interior for vertically stretched grids. To allow a degree of flexibility, the backscatter length-scale in well-resolved regions is defined as $l_\mathrm{B} = \lambda(\Delta x \Delta y \Delta z)^{1/3}$, where the parameter λ can be used to fine-tune l_B, but should be of order of unity. Closer to the surface, the local turbulence production scale eventually reduces below the LES filter width; in this region, it is assumed that the backscatter length-scale decreases with the ratio of the local subgrid mixing length, l, to the subgrid mixing length in well-resolved regions, l_0. Thus, the backscatter length-scale is fully defined as

$$l_\mathrm{B} = \frac{l}{l_0}\lambda(\Delta x \Delta y \Delta z)^{1/3}, \qquad \lambda = \mathcal{O}(1). \tag{32}$$

3.3.5 Level of anisotropy

It is further noted that the local level of anisotropy in the backscatter acceleration fields can be controlled through the local ratio between the three backscatter length-scale components: l_B^x, l_B^y, and l_B^z. To ensure that, locally, the overall backscatter length-scale remains at l_B, the following constraint is enforced at every point in the flow:

$$\left(l_\mathrm{B}^x\, l_\mathrm{B}^y\, l_\mathrm{B}^z\right)^{1/3} = l_\mathrm{B}. \tag{33}$$

The physical anisotropy of accelerations at the grid-scale may be estimated from coarse-grained higher-resolution LES / lower-Reynolds-number DNS. One may also attempt to infer the acceleration variances from (more readily available) velocity variance data; if $\epsilon = C_\epsilon E^{3/2}/l$ is used as an estimate for the dissipation rate in Eq. (26) (where C_ϵ is a constant), one obtains $\sigma_{a_1}^2+\sigma_{a_2}^2+\sigma_{a_3}^2 = 2C_\mathrm{B}C_\epsilon l^4 E^{3/2}/\left(T_\mathrm{B}{l_0}^5\right)$. Since $E = 1/2\,(\sigma_u^2+\sigma_v^2+\sigma_w^2)$, then in isotropic turbulence, the backscatter acceleration fluctuations and the velocity fluctuations are related by $\sigma_a^2 \propto \sigma_u^3$. The assumption is then made that in anisotropic turbulence this relationship also holds for the individual components, and thus that the acceleration variance ratios are related to the velocity variance ratios by:

$$\frac{\sigma_{a_i}^2}{\sigma_{a_j}^2} = \frac{\sigma_{u_i}^3}{\sigma_{u_j}^3}. \tag{34}$$

With the assumed local ratios of acceleration variance ($\sigma_{a_1}^2 : \sigma_{a_2}^2 : \sigma_{a_3}^2$) in place, it is possible to calculate the local values of l_B^x, l_B^y, and l_B^z for the 1-D filters. Doing this requires prior knowledge of the scaling procedure, and so the calculation is presented in §3.5, after the scaling procedure has been outlined in §3.4.

3.3.6 Examples of use

The use of the discrete grid-adaptive Gaussian filter is demonstrated by way of a couple of examples, in which $l_\mathrm{B} = 0.8\Delta x$ is used (which closely approximates the 1:2:1 filter, used in the MT92 model, when the grid spacing is Δx), and, at this stage, fully isotropic backscatter is prescribed, i.e. $\sigma_{a_1}^2 : \sigma_{a_2}^2 : \sigma_{a_3}^2 = 1:1:1$ everywhere (the generation of anisotropic backscatter fields is covered in Chapter 5, in which the new SB model is applied to the neutral ABL). Figure 3.1(a) shows the filter weights in the z-dimension when the filter is centred on a grid point at $z = z_\mathrm{f}$, on a grid with a fixed horizontal-to-vertical grid aspect ratio, for four separate

grids with $\Delta_{AR} = \Delta x/\Delta z = 1, 2, 4$ and 8 respectively. Figure 3.1(b) shows the filter weights in the z-dimension when the filter is centred on three separate grid points on a stretched vertical grid. In both cases, it can be seen that the filter width remains fixed, whilst the number and size of the filter weights adapt accordingly to ensure that the variance of the filtered fields remains unity everywhere.

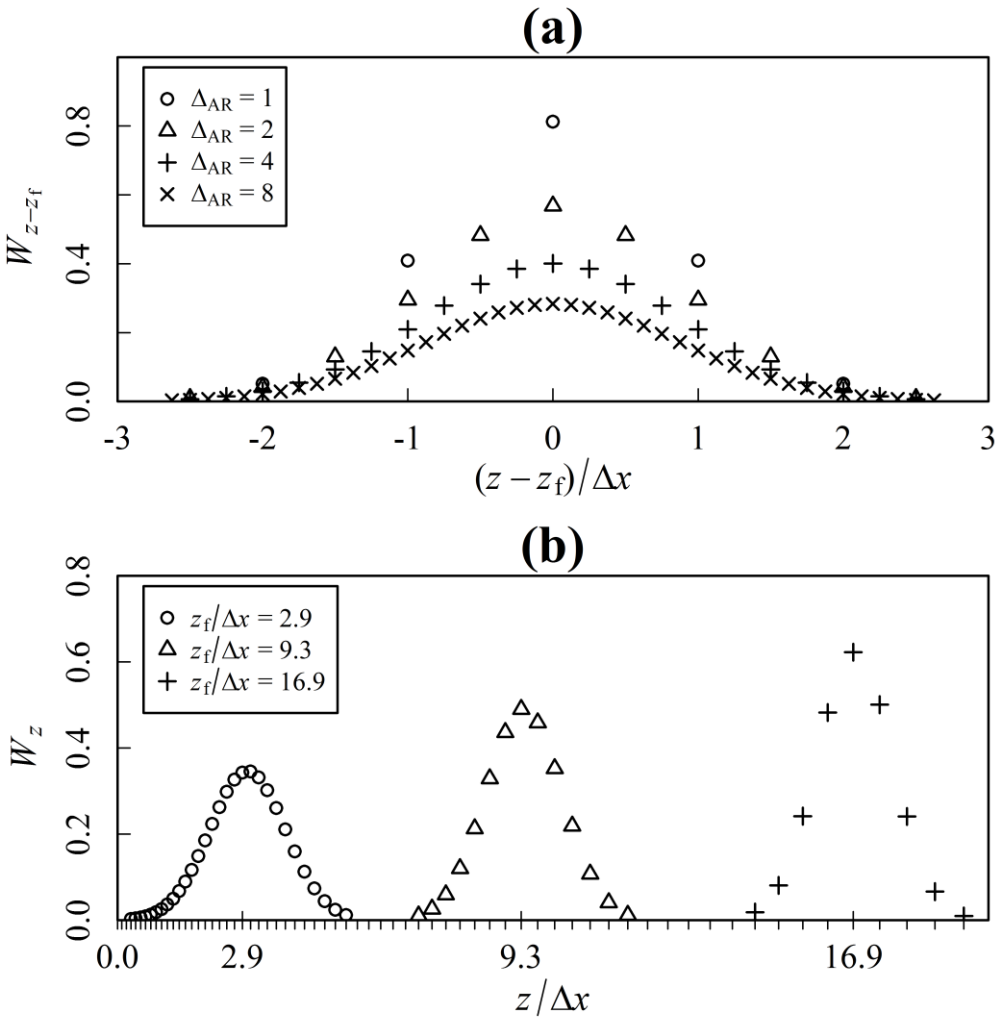

Figure 3.1 – Grid-adaptive filter weights
Weights, W, of the discrete grid-adaptive Gaussian filter in the z-dimension, for $l_B = 0.8\Delta x$ and $\sigma_{a_1}^2 : \sigma_{a_2}^2 : \sigma_{a_3}^2 = 1:1:1$, when (a) the filter is centred on a grid point at $z = z_f$, for four separate grids with $\Delta_{AR} = \Delta x/\Delta z = 1, 2, 4$ and 8, respectively; and (b) the filter is centred on 3 separate grid points (shown by inner tick marks on the lower axis) on a stretched vertical grid (shown by outer tick marks on the lower axis).

Figure 3.2(a) shows an x-z slice through a resulting filtered field, $\hat{\phi}$, for the case $\Delta_{AR} = 4$ (the filter weights in z are shown in Figure 3.1(a)). It can be seen that the characteristic length-scale of the individual structures in the filtered field scales on Δx in both the x and the z dimension (i.e. they are isotropic), despite the significantly finer grid resolution in z. This confirms (at least visually) the ability of the new grid-adaptive filter to control l_B independently of the model grid. Next to this plot (Figure 3.2(b)) is shown an equivalent x-z slice through a field that has been filtered using the 3-D 1:2:1 filter (as used in the MT92 model). Conversely, the filtered field in this case is highly anisotropic, mirroring the anisotropy of the model grid.

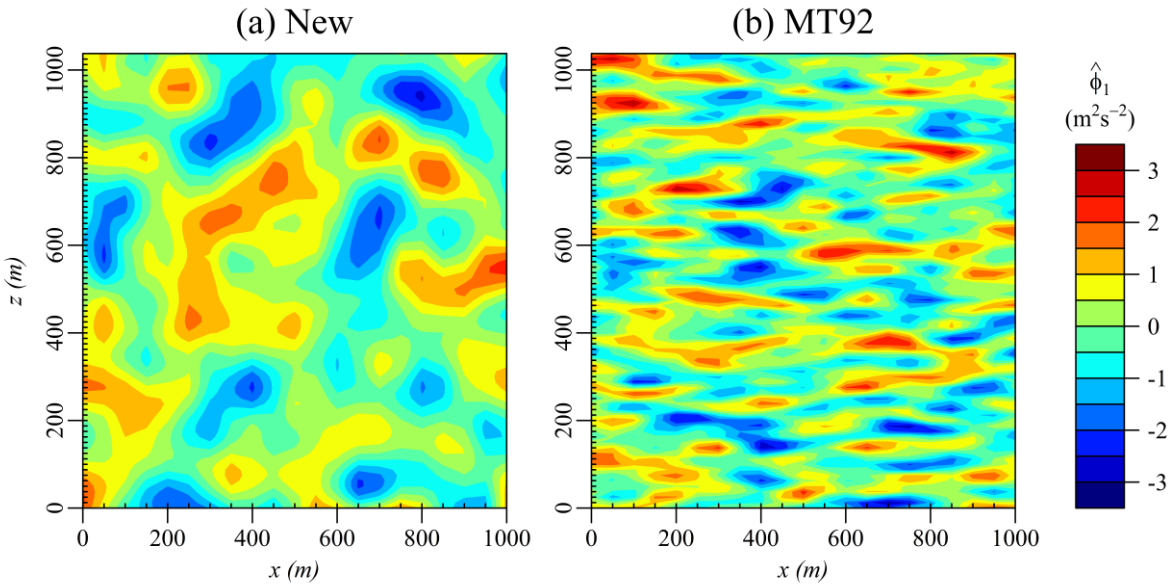

Figure 3.2 – Filtered fields on fixed-aspect-ratio grid
Contour plot of an x-z slice through a filtered field, $\hat{\phi}$, generated using (a) the new grid-adaptive filter, and (b) the MT92 model filter (3-D 1:2:1). The model grid's aspect ratio is $\Delta_{AR} = \Delta x/\Delta z = 4$ (horizontal and vertical grid spacing is shown by inner tick marks on lower and left axes, respectively).

Figure 3.3(a) shows an x-z slice through a resulting filtered field, $\hat{\phi}$, for the case of a vertically stretched grid (filter weights in z are shown in Figure 3.1(b)). Again, it can be seen that the individual structures have length-scales on the order of Δx in both x and the z

throughout the gridded domain, showing that the new grid-adaptive filter is also able to control l_B when the grid aspect ratio is spatially varying. As before, Figure 3.3(b) shows an equivalent x-z slice when the 3-D 1:2:1 filter is used; the anisotropy of the filtered field is again seen to be tied to the anisotropy of the model grid, and so varies spatially, becoming increasingly more isotropic with increasing height.

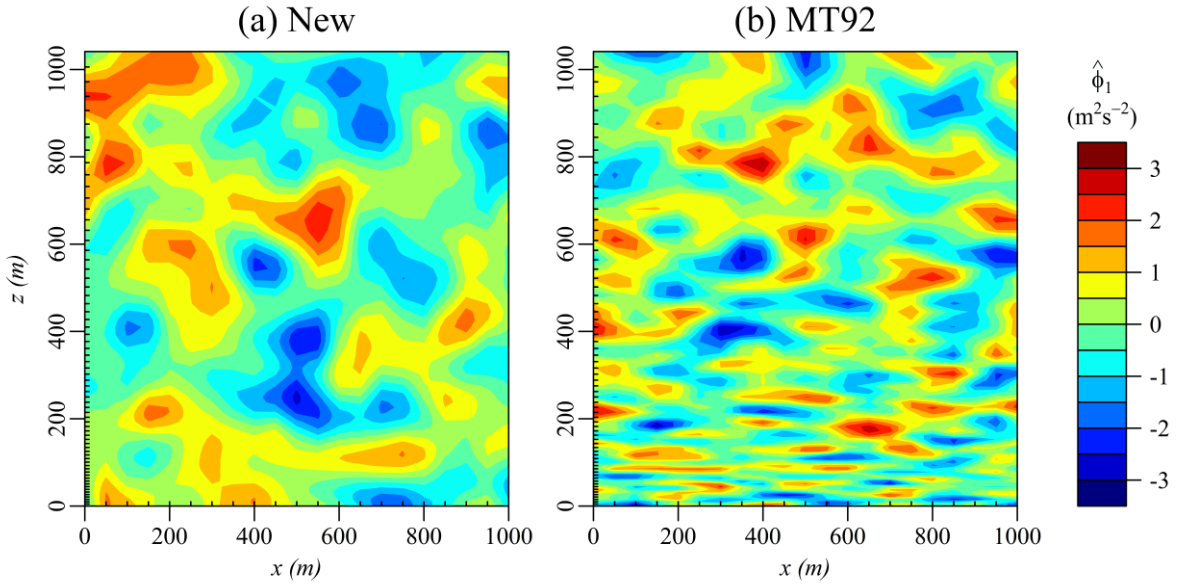

Figure 3.3 – Filtered fields on stretched vertical grid
As Figure 3.2 but for a stretched vertical grid (as shown in Figure 3.1(b)).

3.4 New scaling procedure

The adopted scaling procedure depends on whether the LES is of a horizontally homogeneous flow (e.g. the idealised 2-D ABL), for which a grid with vertical refinement only would typically be employed, or horizontally inhomogeneous flow (e.g. street canyon flow), for which a grid with horizontal and vertical grid refinement might be employed.

3.4.1 Horizontally homogeneous flow

For horizontally homogeneous flow, then, of two variables (l and ϵ) on the right hand side of Eq. (26), l varies only with height, and gradients in ϵ are much greater in the vertical than in the horizontal. Thus, when scaling the backscatter acceleration fields, it seems reasonable to

apply a scaling factor that varies only in the vertical, and ensures that the variance on any horizontal grid level, with index k, is equal to

$$\left(\sigma_{a_1}^2+\sigma_{a_2}^2+\sigma_{a_3}^2\right)_k = \frac{2C_\mathrm{B}}{T_\mathrm{B}}\left(\frac{l_k}{l_0}\right)^5 \langle\epsilon\rangle_k, \tag{35}$$

where the subscript k denotes a quantity at grid level k, and angled brackets denote a horizontal average.

Recalling that $\widehat{\boldsymbol{\phi}}$ is the (filtered) pre-scaled vector field and $\boldsymbol{\phi}$ is the post-scaled vector field, then, for a vertical scaling factor, we have that $\boldsymbol{\phi}^{\boldsymbol{i,j,k}} = g_k\widehat{\boldsymbol{\phi}}^{\boldsymbol{i,j,k}}$, where g_k is the vertical scaling factor at grid level k, and superscripts i, j and k also denote discrete grid-point indices (in the x, y and z direction, respectively). Recall also that the final acceleration vector field, $\boldsymbol{a}$, is generated by taking the curl of $\boldsymbol{\phi}$. For a continuous backscatter acceleration field, this would be expressed as:

$$\boldsymbol{a} = \nabla\times\boldsymbol{\phi} = \begin{bmatrix}\phi_{z,y}-\phi_{y,z}\\ \phi_{x,z}-\phi_{z,x}\\ \phi_{y,x}-\phi_{x,y}\end{bmatrix}\begin{Bmatrix}\boldsymbol{i}\\ \boldsymbol{j}\\ \boldsymbol{k}\end{Bmatrix}, \tag{36}$$

where, e.g., $\phi_{x,y}$ denotes the partial derivate of ϕ_x with respect to y. On the discrete model grid, a discrete curl operation must be performed. Choosing the forward-differencing discrete curl operator, the point-wise backscatter accelerations will thus be equal to

$$\boldsymbol{a}^{\boldsymbol{i,j,k}} = \nabla\times\boldsymbol{\phi}^{\boldsymbol{i,j,k}} = \begin{bmatrix} g_k\left(\hat{\phi}_z^{i,j+1,k}-\hat{\phi}_z^{i,j,k}\right)/\Delta y - \left(g_{k+1}\hat{\phi}_y^{i,j,k+1}-g_k\hat{\phi}_y^{i,j,k}\right)/\Delta z_k\\ \left(g_{k+1}\hat{\phi}_x^{i,j,k+1}-g_k\hat{\phi}_x^{i,j,k}\right)/\Delta z_k - g_k\left(\hat{\phi}_z^{i+1,j,k}-\hat{\phi}_z^{i,j,k}\right)/\Delta x\\ g_k\left(\hat{\phi}_y^{i+1,j,k}-\hat{\phi}_y^{i,j,k}\right)/\Delta x - g_k\left(\hat{\phi}_x^{i,j+1,k}-\hat{\phi}_x^{i,j,k}\right)/\Delta y\end{bmatrix}\begin{Bmatrix}\boldsymbol{i}\\ \boldsymbol{j}\\ \boldsymbol{k}\end{Bmatrix}, \tag{37}$$

where $\Delta z_k = z_{k+1}-z_k$, and, e.g., if $\hat{\phi}_x^{i,j,k} = \hat{\phi}_x(x,y,z)$ then $\hat{\phi}_x^{i+1,j,k} = \hat{\phi}_x(x+\Delta x,y,z)$. Note that the choice of the forward-differencing discrete curl operator is somewhat arbitrary and the backward-differencing operator might also have been used. The central-differencing

operator, however, would introduce another argument (namely g_{k-1}) into Eq. (37) and so is not considered for practical reasons. Since the random fields are filtered such that the variance of $\hat{\boldsymbol{\phi}}$ remains unity everywhere, then, given that the three fields $\hat{\phi}_x, \hat{\phi}_y$ and $\hat{\phi}_z$ are uncorrelated with each other, the three variance components of the acceleration field at a particular grid level k are given by

$$\left(\sigma_{a_i}^2\right)_k = \begin{cases} \frac{2g_k^2}{\Delta y^2}\left(1-\rho_k^{\Delta y}\right) + \frac{1}{\Delta z_k^2}\left(g_{k+1}^2 + g_k^2 - 2g_{k+1}g_k\rho_k^{\Delta z_k}\right), & i=1 \\ \frac{1}{\Delta z_k^2}\left(g_{k+1}^2 + g_k^2 - 2g_{k+1}g_k\rho_k^{\Delta z_k}\right) + \frac{2g_k^2}{\Delta x^2}\left(1-\rho_k^{\Delta x}\right), & i=2 \\ \frac{2g_k^2}{\Delta x^2}\left(1-\rho_k^{\Delta x}\right) + \frac{2g_k^2}{\Delta y^2}\left(1-\rho_k^{\Delta y}\right), & i=3 \end{cases} \tag{38}$$

where, e.g., $\rho_k^{\Delta x}$ denotes the autocorrelation coefficient between $\hat{\phi}(x,y,z)$ and $\hat{\phi}(x+\Delta x,y,z)$ for any of $\hat{\phi}_x, \hat{\phi}_y$ or $\hat{\phi}_z$ at grid level k. These autocorrelations will take a value between 0 and 1 depending on the chosen filtering procedure. For example, with the MT92 model, a 1:2:1 filter is applied to random numbers generated directly on the model grid, and it can be shown that $\rho^{\Delta x} = \rho^{\Delta y} = \rho^{\Delta z} = 2/3$ at every grid level. Similarly, with the WM08 model, a 1:4:6:4:1 filter (equivalent to a double application of the 1:2:1 filter) is applied to random numbers generated on an isotropic grid, and in this case $\rho^{\Delta x} = \rho^{\Delta y} = \rho^{\Delta z} = 4/5$ at every isotropic grid level (the values after interpolation onto the anisotropic model grid may also be derived, but this is not shown here for brevity). The autocorrelations expected with the new SB model are later shown to be given by Eq. (44).

Combining Eqs. (35) and (38) leads to a quadratic equation for g_k with solutions

$$g_k = \frac{-b \pm \sqrt{b^2 - 4ac}}{2a}, \quad \text{where}$$

$$a = \frac{4}{\Delta x^2}\left(1 - \rho_k^{\Delta x}\right) + \frac{4}{\Delta y^2}\left(1 - \rho_k^{\Delta y}\right) + \frac{2}{\Delta z_k^2}, \tag{39}$$

$$b = \frac{-4 g_{k+1} \rho_k^{\Delta z_k}}{\Delta z_k^2}, \qquad c = \frac{2 g_{k+1}^2}{\Delta z_k^2} - \frac{2 C_{\mathrm{B}}}{T_{\mathrm{B}}}\left(\frac{l_k}{l_0}\right)^5 \langle \epsilon \rangle_k.$$

In practice, it is necessary to first calculate the scaling factor at the top grid level, g_n say, by assuming that $g_{n+1} = g_n$, and then proceed down the grid levels using the full quadratic Eq. (39) and taking the larger root (positive sign) when real solutions exist.

It has been found that the discriminant, $b^2 - 4ac$, of this quadratic equation can become negative near the surface, where the theoretical energy backscatter rate falls sharply to zero, indicating that no real solutions exist for g_k. When this happens, the discriminant is set to zero to allow a real value of g_k to be calculated. This modifies the imposed backscatter rate away from the intended theoretical value. To correct this, another scaling factor must be applied at these grid levels after the curl operation, which is calculated empirically. This 'post-curl' scaling factor has the unwanted effect of reintroducing divergences into the backscatter acceleration field at these grid levels. Although these divergences are immediately removed by the pressure solver, this action results in a small but unwanted reduction in the backscattered energy (Weinbrecht and Mason, 2008). Fortunately, later testing shows (see §4.3.1) that this only affects a very small region close to the surface; $z/H \lesssim 0.01$, where H is the boundary layer scaling height.

3.4.2 Horizontally inhomogeneous flow

For horizontally inhomogeneous flow, where a grid with horizontal and vertical grid refinement might be employed, it is necessary to use a point-wise scaling factor, since the use of a horizontally averaged dissipation rate, $\langle\epsilon\rangle_k$, in Eq. (39) is no longer appropriate (and Δx, Δy possibly not constant). Each grid-point must therefore be scaled separately in order to satisfy

$$\left(\sigma_{a_1}^2+\sigma_{a_2}^2+\sigma_{a_3}^2\right)_{i,j,k}=\frac{2C_\mathrm{B}}{T_\mathrm{B}}\left(\frac{l_k}{l_0}\right)^5\epsilon_{i,j,k}, \tag{40}$$

If $g_{i,j,k}$ is used to denote the point-wise scaling factor at grid point i,j,k, then, for a point-wise scaling factor, we have that $\boldsymbol{\phi}^{\boldsymbol{i,j,k}}=g_{i,j,k}\widehat{\boldsymbol{\phi}}^{\boldsymbol{i,j,k}}$. In contrast to Eq. (37), for practical reasons we must assume (for now) that local gradients in the scaling factor are small, i.e. that $\Delta g_{i,j,k}\ll g_{i,j,k}$ in all 3 dimensions (where $\Delta g_{i,j,k}$ is the difference between $g_{i,j,k}$ and the scaling factor at the adjacent grid point in the positive direction of a given dimension), application of the discrete curl operator this time leads to

$$\boldsymbol{a}^{\boldsymbol{i,j,k}}=\nabla\times\boldsymbol{\phi}^{\boldsymbol{i,j,k}}=g_{i,j,k}\begin{bmatrix}\left(\hat{\phi}_z^{i,j+1,k}-\hat{\phi}_z^{i,j,k}\right)/\Delta y-\left(\hat{\phi}_y^{i,j,k+1}-\hat{\phi}_y^{i,j,k}\right)/\Delta z_k\\ \left(\hat{\phi}_x^{i,j,k+1}-\hat{\phi}_x^{i,j,k}\right)/\Delta z_k-\left(\hat{\phi}_z^{i+1,j,k}-\hat{\phi}_z^{i,j,k}\right)/\Delta x\\ \left(\hat{\phi}_y^{i+1,j,k}-\hat{\phi}_y^{i,j,k}\right)/\Delta x-\left(\hat{\phi}_x^{i,j+1,k}-\hat{\phi}_x^{i,j,k}\right)/\Delta y\end{bmatrix}\begin{Bmatrix}\boldsymbol{i}\\ \boldsymbol{j}\\ \boldsymbol{k}\end{Bmatrix}. \tag{41}$$

The three variance components of the acceleration field at a particular grid point are thus given by

$$\left(\sigma_{a_m}^2\right)_{i,j,k}=\begin{cases}\dfrac{2g_{i,j,k}^2}{\Delta y_j^2}\left(1-\rho_{i,j,k}^{\Delta y_j}\right)+\dfrac{2g_{i,j,k}^2}{\Delta z_k^2}\left(1-\rho_{i,j,k}^{\Delta z_k}\right), & m=1\\ \dfrac{2g_{i,j,k}^2}{\Delta z_k^2}\left(1-\rho_{i,j,k}^{\Delta z_k}\right)+\dfrac{2g_{i,j,k}^2}{\Delta x_i^2}\left(1-\rho_{i,j,k}^{\Delta x_i}\right), & m=2\\ \dfrac{2g_{i,j,k}^2}{\Delta x_i^2}\left(1-\rho_{i,j,k}^{\Delta x_i}\right)+\dfrac{2g_{i,j,k}^2}{\Delta y_j^2}\left(1-\rho_{i,j,k}^{\Delta y_j}\right), & m=3\end{cases} \tag{42}$$

Combining Eqs. (40) and (42) leads to:

$$g_{i,j,k} = \sqrt{\frac{\frac{2C_{\mathrm{B}}}{T_{\mathrm{B}}}\left(\frac{l_k}{l_0}\right)^5 \epsilon_{i,j,k}}{\frac{4}{\Delta x_i^2}\left(1-\rho_{i,j,k}^{\Delta x_i}\right)+\frac{4}{\Delta y_j^2}\left(1-\rho_{i,j,k}^{\Delta y_j}\right)+\frac{4}{\Delta z_k^2}\left(1-\rho_{i,j,k}^{\Delta z_k}\right)}}. \tag{43}$$

In reality, non-zero local gradients cause deviations away from the intended point-wise backscatter rates in the curled field. As with the vertical scaling factor procedure, the biggest problems occur very near the surface where the theoretical backscatter rate drops rapidly. To help correct this, an empirically calculated vertical scaling factor is again applied after the curl operation to ensure that Eq. (35) is satisfied at each grid level, i.e. that the horizontally averaged backscatter rate is at least always recovered. The resulting divergences introduced into the acceleration field are typically comparable in size to those seen with the vertical scaling factor procedure for the same case.

3.5 Backscatter length-scale components

This section details how to calculate the local values of l_{B}^x, l_{B}^y, and l_{B}^z from the assumed local ratios of acceleration variance, $\sigma_{a_1}^2 : \sigma_{a_2}^2 : \sigma_{a_3}^2$. For LES of horizontally homogeneous turbulence, in which a vertically refined grid is utilised, Eqs. (38) are used, with the assumption that $\Delta g_k \ll g_k$ (and thus that $g_{k+1} \approx g_k$), to obtain a set of three simultaneous equations (one for each of $\sigma_{a_1}^2/\sigma_{a_2}^2$, $\sigma_{a_1}^2/\sigma_{a_3}^2$ and $\sigma_{a_2}^2/\sigma_{a_3}^2$) at each grid level, k, with three unknowns; namely, $\rho_k^{\Delta x}$, $\rho_k^{\Delta y}$ and $\rho_k^{\Delta z_k}$. For horizontally inhomogeneous turbulence and/or for grids with vertical and horizontal refinement, Eqs. (42) are instead used to obtain a set of three equations at each grid point (note that as long as the turbulence field is stationary, these equations need only be solved once, at the beginning of the simulation, reducing computational cost dramatically). Now, it can be shown that the spatial autocorrelation

induced by the application of a continuous 1-D Gaussian filter (Eq. (29)) on a continuous 1-D white-noise field in the general dimension ζ is

$$\rho^{\Delta\zeta} = \exp\left\{-\left(\frac{\Delta\zeta}{2l_{\mathrm{B}}^{\zeta}}\right)^2\right\}. \tag{44}$$

This equation may thus be used, along with the constraint imposed by Eq. (33), to solve each set of simultaneous equations for l_{B}^{x}, l_{B}^{y} and l_{B}^{z}. This is achieved by using the following iterative procedure, which is found to give sufficiently accurate solutions after only one or two iterations: (i) select a sensible initial guess for l_{B}^{x}, e.g. $l_{\mathrm{B}}^{x} = l_{\mathrm{B}}$, and solve Eq. (44) for $\rho^{\Delta x}$; (ii) use this result to solve Eq. (45) (below) for $\rho^{\Delta y}$, which follows from elimination of $\rho^{\Delta z}$ from the simultaneous equation set, and subsequently obtain l_{B}^{y} using Eq. (44); (iii) use this result to solve any one of the simultaneous equation set for $\rho^{\Delta z}$, e.g., Eq. (46) (below), and subsequently obtain l_{B}^{z} using Eq. (44); (iv) multiply each of l_{B}^{x}, l_{B}^{y} and l_{B}^{z} by the factor $l_{\mathrm{B}}/\left(l_{\mathrm{B}}^{x}\, l_{\mathrm{B}}^{y}\, l_{\mathrm{B}}^{z}\right)$ to ensure that Eq. (33) is satisfied; (v) use the newly calculated value of l_{B}^{x} as the initial guess in the iteration process and repeat steps (ii) to (v) until a sufficient level of accuracy has been reached.

$$\rho^{\Delta y} = 1 - \frac{\Delta y^2(1-\rho^{\Delta x})\left\{\frac{\sigma_{a_1}^2}{\sigma_{a_3}^2}\left(1-\frac{\sigma_{a_1}^2}{\sigma_{a_2}^2}\right)-\frac{\sigma_{a_1}^2}{\sigma_{a_2}^2}\right\}}{\Delta x^2\left\{\left(1-\frac{\sigma_{a_1}^2}{\sigma_{a_3}^2}\right)\left(1-\frac{\sigma_{a_1}^2}{\sigma_{a_2}^2}\right)-1\right\}}, \tag{45}$$

$$\rho^{\Delta z_k} = 1 - \frac{\sigma_{a_1}^2}{\sigma_{a_2}^2}\frac{\Delta z_k^2(1-\rho^{\Delta x})}{\Delta x^2\left(1-\frac{\sigma_{a_1}^2}{\sigma_{a_2}^2}\right)} + \frac{\Delta z_k^2(1-\rho^{\Delta y})}{\Delta y^2\left(1-\frac{\sigma_{a_1}^2}{\sigma_{a_2}^2}\right)}. \tag{46}$$

Note that for real solutions of l_{B}^{ζ} to exist with Eq. (44), it is required that $0 < \rho^{\Delta\zeta} < 1$, which is also a requirement on account of $\rho^{\Delta\zeta}$ being a (positive) correlation coefficient. It has been

found that this requirement is met as long as the local grid aspect ratios do not differ significantly from the intended local ratios of the acceleration variance components.

3.6 Backscatter vertical momentum flux

This section outlines a further improvement to the MT92-type SB model. This improvement allows the grid-scale vertical momentum flux, which affects the local rate of mixing and thus local velocity gradients, to be adjusted towards a level that is more representative of empirical observations or theory. Importantly, this modification does not affect the ability of the model to satisfy its other constraints, and requires almost no additional computational effort. It is also stressed that this modification can be used to improve the representation of backscatter in any general two-dimensional shear flow in which two of the three momentum flux components are virtually zero.

Recall that the three component (scalar) fields of $\hat{\boldsymbol{\phi}}$ (filtered random fields with zero mean and unit variance) in the $x,\ y$ and z dimensions are denoted by $\hat{\phi}_x,\ \hat{\phi}_y$ and $\hat{\phi}_z$, respectively. In addition to this, three *independently generated* scalar fields, $\hat{\phi}_1,\ \hat{\phi}_2$ and $\hat{\phi}_3$, are defined, and the following alternative approach is considered, in which the first and third component fields can be correlated with each other:

$$\{\hat{\phi}_x, \hat{\phi}_y, \hat{\phi}_z\} = \left\{\hat{\phi}_1, \hat{\phi}_2, \alpha\hat{\phi}_1 + \sqrt{1-\alpha^2}\hat{\phi}_3\right\}, \quad \text{where} \ \ 0 \leq \alpha \leq 1. \tag{47}$$

This formulation ensures that $\hat{\phi}_z$ always has unit variance. Thus, when $\alpha = 0$, $\hat{\phi}_z$ is fully independent of $\hat{\phi}_x$ and the original approach is retrieved; when $\alpha = 1$, $\hat{\phi}_x$ and $\hat{\phi}_z$ are identical. For intermediate values of α, $\hat{\phi}_x$ and $\hat{\phi}_z$ will be correlated to some degree.

To understand why this may be useful from the point of view of controlling grid-scale vertical momentum flux, one first requires a way to link the effect of the backscatter *accelerations* on

the LES *velocity* fields. It is first recalled that the backscatter time-scale, T_{B}, is necessarily small (on the order of the model time-step, Δt) in order to ensure that all fluid elements experience the same time-scale of stress variation (Mason and Brown, 1994). One may thus linearly approximate the backscatter velocity fluctuations (which are denoted by the subscript B) from the backscatter accelerations as $u'_{i_{\mathrm{B}}} = a_i T_{\mathrm{B}}$. The six (independent) components of the resulting stress tensor relating to the backscatter velocity fluctuations, $\overline{u'_i u'_j}_{\mathrm{B}}$, are thus well approximated by:

$$\begin{bmatrix} \overline{u'^2}_{\mathrm{B}} & \overline{u'v'}_{\mathrm{B}} & \overline{u'w'}_{\mathrm{B}} \\ & \overline{v'^2}_{\mathrm{B}} & \overline{v'w'}_{\mathrm{B}} \\ & & \overline{w'^2}_{\mathrm{B}} \end{bmatrix} = T_{\mathrm{B}}^2 \begin{bmatrix} \overline{a_1^2} & \overline{a_1 a_2} & \overline{a_1 a_3} \\ & \overline{a_2^2} & \overline{a_2 a_3} \\ & & \overline{a_3^2} \end{bmatrix}. \tag{48}$$

Recalling that $\boldsymbol{a^{i,j,k}} = \nabla \times \boldsymbol{\phi^{i,j,k}} = \nabla \times g_{i,j,k} \widehat{\boldsymbol{\phi}}^{\boldsymbol{i,j,k}}$, then, using the forward-difference curl operator (as before) and assuming that local gradients in the scaling factor are small, i.e. $\Delta g_{i,j,k} \ll g_{i,j,k}$ for any Δx_i, Δy_j, Δz_k, it follows from Eqs. (36) and (47) that

$$\boldsymbol{a^{i,j,k}} \cong g_{i,j,k} \begin{bmatrix} \left(\alpha \hat{\phi}_1^{i,j+1,k} + \sqrt{1-\alpha^2}\hat{\phi}_3^{i,j+1,k} - \alpha \hat{\phi}_1^{i,j,k} - \sqrt{1-\alpha^2}\hat{\phi}_3^{i,j,k}\right)/\Delta y_j - \left(\hat{\phi}_2^{i,j,k+1} - \hat{\phi}_2^{i,j,k}\right)/\Delta z_k \\ \left(\hat{\phi}_1^{i,j,k+1} - \hat{\phi}_1^{i,j,k}\right)/\Delta z_k - \left(\alpha \hat{\phi}_1^{i+1,j,k} + \sqrt{1-\alpha^2}\hat{\phi}_3^{i+1,j,k} - \alpha \hat{\phi}_1^{i,j,k} - \sqrt{1-\alpha^2}\hat{\phi}_3^{i,j,k}\right)/\Delta x_i \\ \left(\hat{\phi}_2^{i+1,j,k} - \hat{\phi}_2^{i,j,k}\right)/\Delta x_i - \left(\hat{\phi}_1^{i,j+1,k} - \hat{\phi}_1^{i,j,k}\right)/\Delta y_j \end{bmatrix} \begin{Bmatrix} \boldsymbol{i} \\ \boldsymbol{j} \\ \boldsymbol{k} \end{Bmatrix}. \tag{49}$$

Each backscatter stress component, $\overline{u'_i u'_j}_{\mathrm{B}}$, can then be obtained from time-averaging the appropriate product of acceleration components, following Eq. (48). Since the three fields $\hat{\phi}_1$, $\hat{\phi}_2$ and $\hat{\phi}_3$ are uncorrelated with each other, the only non-zero terms after averaging will be those involving the product of a field with itself. It is further recalled that each field satisfies $\overline{\hat{\phi}^2} = 1$, i.e. there is unit variance at any given point. Thus, the local magnitude of each of these six terms is well approximated by:

$$
\begin{aligned}
\overline{u'^2}_{\mathrm{B}} &= 2T_{\mathrm{B}}^2 g_{i,j,k}^2 \left[\left(1-\rho_{i,j,k}^{\Delta y_j}\right)/\Delta y_j^2 + \left(1-\rho_{i,j,k}^{\Delta z_k}\right)/\Delta z_k^2\right] \\
\overline{v'^2}_{\mathrm{B}} &= 2T_{\mathrm{B}}^2 g_{i,j,k}^2 \left[\left(1-\rho_{i,j,k}^{\Delta z_k}\right)/\Delta z_k^2 + \left(1-\rho_{i,j,k}^{\Delta x_i}\right)/\Delta x_i^2 - \underline{\alpha\left(1-\rho_{i,j,k}^{\Delta x_i}-\rho_{i,j,k}^{\Delta z_k}+\rho_{i,j,k}^{\Delta x_i}\rho_{i,j,k}^{\Delta z_k}\right)/\Delta x_i \Delta z_k}\right] \\
\overline{w'^2}_{\mathrm{B}} &= 2T_{\mathrm{B}}^2 g_{i,j,k}^2 \left[\left(1-\rho_{i,j,k}^{\Delta x_i}\right)/\Delta x_i^2 + \left(1-\rho_{i,j,k}^{\Delta y_j}\right)/\Delta y_j^2\right] \\
\overline{u'v'}_{\mathrm{B}} &= -T_{\mathrm{B}}^2 g_{i,j,k}^2 \left[\left(1-\rho_{i,j,k}^{\Delta x_i}-\rho_{i,j,k}^{\Delta y_j}+\rho_{i,j,k}^{\Delta x_i}\rho_{i,j,k}^{\Delta y_j}\right)/\Delta x_i \Delta y_j - \underline{\alpha\left(1-\rho_{i,j,k}^{\Delta y_j}-\rho_{i,j,k}^{\Delta z_k}+\rho_{i,j,k}^{\Delta y_j}\rho_{i,j,k}^{\Delta z_k}\right)/\Delta y_j \Delta z_k}\right] \\
\overline{u'w'}_{\mathrm{B}} &= -T_{\mathrm{B}}^2 g_{i,j,k}^2 \left[\underline{2\alpha\left(1-\rho_{i,j,k}^{\Delta y_j}\right)/\Delta y_j^2} + \left(1-\rho_{i,j,k}^{\Delta x_i}-\rho_{i,j,k}^{\Delta z_k}+\rho_{i,j,k}^{\Delta x_i}\rho_{i,j,k}^{\Delta z_k}\right)/\Delta x_i \Delta z_k\right] \\
\overline{v'w'}_{\mathrm{B}} &= -T_{\mathrm{B}}^2 g_{i,j,k}^2 \left[\left(1-\rho_{i,j,k}^{\Delta y_j}-\rho_{i,j,k}^{\Delta z_k}+\rho_{i,j,k}^{\Delta y_j}\rho_{i,j,k}^{\Delta z_k}\right)/\Delta y_j \Delta z_k - \underline{\alpha\left(1-\rho_{i,j,k}^{\Delta x_i}-\rho_{i,j,k}^{\Delta y_j}+\rho_{i,j,k}^{\Delta x_i}\rho_{i,j,k}^{\Delta y_j}\right)/\Delta x_i \Delta y_j}\right]
\end{aligned}
\tag{50}
$$

The underlined terms in Eqs. (50) show the additional terms that appear as a result of using Eq. (47) over the original approach. If the choice is made to adopt the same spatial filtering procedure on the $\hat{\phi}$ fields with the old and new approaches (meaning that all $\rho^{\Delta\zeta}$ values remain unchanged from one approach to the other), it is seen that, with the new approach, the magnitude of the backscatter covariance component $\overline{u'w'}_{\mathrm{B}}$ is increased (by an amount which depends on the value of α), and the magnitude of the $\overline{u'v'}_{\mathrm{B}}$ and $\overline{v'w'}_{\mathrm{B}}$ components are reduced (by a smaller amount). Furthermore, the auto-variance component $\overline{v'^2}_{\mathrm{B}}$ is also slightly reduced, and, since the sum of the three auto-variance components is fixed by the locally expected energy backscatter rate, components $\overline{u'^2}_{\mathrm{B}}$ and $\overline{w'^2}_{\mathrm{B}}$ must also increase slightly. Thus, while the magnitudes of the covariance terms are constrained to some degree by the scaling factor $g_{i,j,k}$ and the filter correlation $\rho_{i,j,k}^{\Delta\zeta}$, which must be chosen based on the desired local energy backscatter rate and backscatter anisotropy, some degree of control is recovered with the new approach through the choice of the parameter α. To aid this choice, the expected magnitudes of the covariance terms are discussed next.

It is recalled that for a two-dimensional (2-D) mean shear flow, velocity fluctuations in the third dimension (i.e. that which is horizontally perpendicular to the direction of mean flow) will be uncorrelated with velocity fluctuations in the other two dimensions, i.e. $\overline{u'v'}$, $\overline{v'w'} = 0$ (with the y-axis aligned with this third dimension). The $\overline{u'w'}$ component, however, will be non-zero and thus represents the total vertical momentum flux. In light of this, the backscatter stress term $\overline{u'w'}_{\mathrm{B}}$ shall also be allowed to be non-negligible within the roof-level shear-layer region. A new parameter is defined called the 'backscatter vertical momentum flux factor', $\mathrm{VMF}_{\mathrm{B}}$, which describes the ratio of the magnitude of $\overline{u'w'}_{\mathrm{B}}$ to $\sigma_{u\mathrm{B}}\sigma_{w\mathrm{B}}$, where, e.g., $\sigma_{u\mathrm{B}} \equiv \sqrt{\overline{u'^2}_{\mathrm{B}}}$:

$$\mathrm{VMF}_{\mathrm{B}} = \frac{\left|\overline{u'w'}_{\mathrm{B}}\right|}{\sigma_{u\mathrm{B}}\sigma_{w\mathrm{B}}}. \tag{51}$$

Substituting in the corresponding terms from Eqs. (50) and rearranging for α, one obtains:

$$\alpha_{i,j,k} = \frac{2\,\mathrm{VMF}_{\mathrm{B}}\sqrt{\left[\frac{\left(1-\rho_{i,j,k}^{\Delta y_j}\right)}{\Delta y_j^2}+\frac{\left(1-\rho_{i,j,k}^{\Delta z_k}\right)}{\Delta z_k^2}\right]\left[\frac{\left(1-\rho_{i,j,k}^{\Delta x_i}\right)}{\Delta x_i^2}+\frac{\left(1-\rho_{i,j,k}^{\Delta y_j}\right)}{\Delta y_j^2}\right]}-\frac{1-\rho_{i,j,k}^{\Delta x_i}-\rho_{i,j,k}^{\Delta z_k}+\rho_{i,j,k}^{\Delta x_i}\rho_{i,j,k}^{\Delta z_k}}{\Delta x_i \Delta z_k}}{\frac{2\left(1-\rho_{i,j,k}^{\Delta y_j}\right)}{\Delta y_j^2}} \tag{52}$$

It is noted that the permissible range of $\mathrm{VMF}_{\mathrm{B}}$ is limited by α; the minimum value corresponds to when $\alpha = 0$ and the maximum value to when $\alpha = 1$.

This new approach is demonstrated more formally with an example of its application. For simplicity, an isotropic model grid (with resolution Δ) is considered, and a discrete Gaussian filter is used with a width (i.e. backscatter length-scale) of $l_{\mathrm{B}} = \Delta$ when filtering each $\hat{\phi}$ field, which results in an auto-correlation coefficient of $\rho^{\Delta} = 0.8$ everywhere, and (with the old approach) fully isotropic backscatter. The resulting backscatter stresses are normalised by the

sum of the three auto-variance components, which is fixed for a given dissipation field. The resulting (relative) magnitudes are shown in Figure 3.4 for the cases: (a) $\alpha = 0$ (equivalent to the old approach in which $\hat{\phi}_x$ and $\hat{\phi}_z$ are fully independent), which corresponds to a value of $\mathrm{VMF_B} = 0.05$; and (b) $\mathrm{VMF_B} = 0.5$ (i.e. $\hat{\phi}_z$ and $\hat{\phi}_x$ are correlated to such a degree that the magnitude of $\overline{u'w'}_\mathrm{B}$ is half that of $\sigma_{u\mathrm{B}}\sigma_{w\mathrm{B}}$), which corresponds to a value of $\alpha = 0.89$. It is seen that with the old approach, all three covariance components are very small compared with the auto-variance components (around 5% the size). No consideration was previously given to the magnitude of the covariance components; they were simply a by-product of the overall backscatter generation procedure. With the new approach, it is seen that by increasing $\mathrm{VMF_B}$ (i.e. making $\hat{\phi}_x$ and $\hat{\phi}_z$ more correlated), the magnitude of the $\overline{u'w'}_\mathrm{B}$ component relative to the three auto-variance components can be increased significantly. The maximum achievable value of $\mathrm{VMF_B}$ (corresponding to $\alpha = 1$) is approximately 0.6 in this case. The other two covariance components, $\overline{u'v'}_\mathrm{B}$ and $\overline{v'w'}_\mathrm{B}$, tend to zero as α tends to 1. It is noted that because the auto-variance component $\overline{v'^2}_\mathrm{B}$ is slightly reduced (and consequently $\overline{u'^2}_\mathrm{B}$ and $\overline{w'^2}_\mathrm{B}$ slightly increased) with the new approach, a small amount of accuracy has been sacrificed in the intention to generate fully isotropic backscatter acceleration fields. However, even with the maximum value of $\mathrm{VMF_B}$ (when $\alpha = 1$), this reduction is not large ($\overline{v'^2}_\mathrm{B}$ is only around 10% smaller than the other two auto-variance components). Note also that the backscatter acceleration fields can still be scaled such that the sum of the three auto-variance components remains at the intended value, and so the intended local energy backscatter rate is not violated.

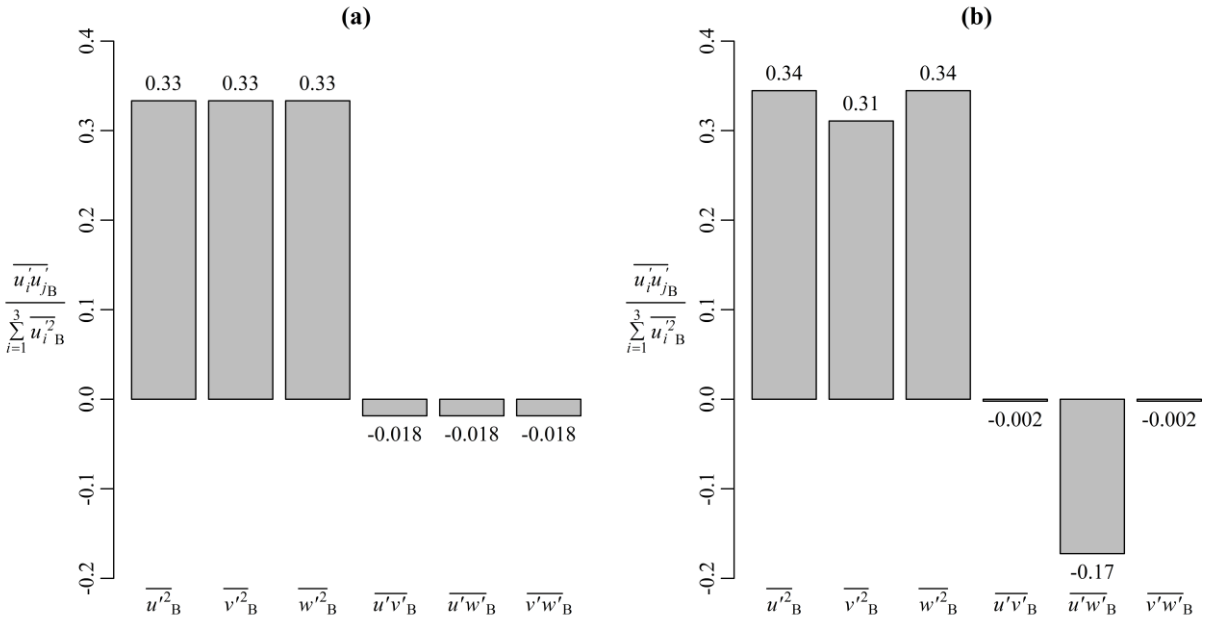

Figure 3.4 – Backscatter stresses
Normalised backscatter stresses on an isotropic model grid with resolution $\boldsymbol{\Delta}$ and a backscatter length-scale of $\boldsymbol{l_B = \Delta}$, with a backscatter VMF factor of (a) $\boldsymbol{\mathrm{VMF_B} = 0.05}$ (corresponds to $\boldsymbol{\alpha = 0}$), and (b) $\boldsymbol{\mathrm{VMF_B} = 0.5}$ (corresponds to $\boldsymbol{\alpha = 0.89}$).

3.7 Summary and conclusions

In this chapter, a new methodology has been proposed for the generation of stochastic backscatter acceleration fields designed to impose fluctuations in the Smagorinsky subgrid stresses in order to mimic backscattered energy from the subgrid scales. The methodology employs a discrete "grid-adaptive" filter that allows control of spatial variations in the backscatter length-scale and anisotropy (§3.3). Thus, unlike the previous models of Mason and Thomson (1992) and Weinbrecht and Mason (2008), with which these properties are either tied to the model grid or spatially uniform, the backscatter length-scale can be appropriately reduced towards surfaces, and the backscatter anisotropy can be chosen to be consistent with the physical anisotropy of the subgrid scales. The backscatter length-scale may also be varied in accordance with any spatial variations in the LES filter width, thus widening the applicability of the new model to studies of more complex flow geometries that

utilise local 3-D grid refinement. The efficacy of the new filtering procedure was confirmed via demonstrations of its use; example filtered fields were generated on a number of different grids with varying grid spacings, whilst the backscatter length-scale and anisotropy were successfully held fixed (Figures 3.2 and 3.3). Details of a new scaling procedure, which ensures a theoretically appropriate energy backscatter rate at each level (for horizontally homogeneous flow) or each point (for horizontally inhomogeneous flow) in the modelled flow-field, were also given (§3.4).

In addition, an improvement to the SB model was also outlined that facilitates a better representation of grid-scale vertical momentum flux (§3.6). This is done by imposing a constraint on the magnitude of the main *covariance* term of the three backscatter acceleration components, which is satisfied by prescribing an appropriate degree of correlation between the first and third filtered component fields (this is in addition to the constraint on the magnitude of their *variances*, which ensures a theoretically appropriate energy backscatter rate, and remains satisfied). The ability to control the backscatter vertical momentum flux is a desirable feature because it directly affects the amount of additional vertical mixing caused by the backscatter fluctuations, and thus the extent to which local velocity gradients are modified. Again, the efficacy of this new feature was confirmed via an example of its use; the calculated magnitude of the dominating backscatter VMF component, $\overline{u'w'}_{\mathrm{B}}$, was successfully increased in an example backscatter acceleration field when the correlation between the first and third filtered fields was increased.

Limitations of the new SB model include the fact that the backscatter time-scale is (like with the MT92 and WM08 models) still physically unrealistic, being based on the numerical model time-step rather than a more appropriate time-scale over which grid-scale fluctuations are

expected to vary. The problem with simply increasing the backscatter timescale to give a better match in this regard, is that the assumption of linear backscatter perturbations (i.e. $u'_{i_{\mathrm{B}}} = a_i T_{\mathrm{B}}$) starts to break down, and a Lagrangian approach to 'follow' perturbed fluid elements would be required in order to ensure Galilean invariance. Again, however, it is recalled that empirical evidence from previous studies (Mason and Brown, 1994, Grooms *et al.*, 2015) suggests that employing an unrealistically short time-scale is not detrimental to model performance, and ensures that all fluid elements experience the same time-scale of stress variation (Mason and Brown, 1994). Another limitation of the new SB model in its current state is that it is specifically set up for simulations of neutral atmospheric flows only. However, with appropriate modification, e.g. to the theoretical energy backscatter rate, the model might also be applied in non-neutral stability regimes. Direction can be taken from Brown *et al.* (1994) in this regard, who have already modified the MT92 model for application to the stably stratified ABL.

In conclusion, the new SB model is able to generate stochastic backscatter acceleration fields in a way that allows for grid-independent control of the backscatter length-scale, anisotropy and momentum flux; the first research objective (§2.4) has therefore been satisfied. The next step is to implement the new SB model into a working LES code and test whether it can overcome the grid-dependency issues associated with previous SB models in simulations of the neutral ABL.

4. THE NEUTRAL ATMOSPHERIC BOUNDARY LAYER

4.1 Introduction

This chapter addresses research objective #2, as stated at the end of §2.4 and repeated below for convenience:

> **Objective #2**: Evaluate the grid-independence of the new SB model by performing LES of the neutral ABL for various grid anisotropies, comparing surface-layer velocity shear profiles against those obtained with the Smagorinsky, MT92 and WM08 SGS models.

As discussed in §2.3.2, previous studies utilising the SB modelling approach for LES of the neutral ABL have been shown to be remarkably successful in reducing excessive velocity shear, as predicted with the widely-used Smagorinsky model, within the under-resolved surface layer (Mason and Thomson, 1992, Brown *et al.*, 1994, Mason and Brown, 1994, Weinbrecht and Mason, 2008). Simulation of the neutral ABL therefore provides the ideal case for testing the new SB model, since (i) the theoretical profiles against which the LES output is validated are well established, and (ii) the performance of the new SB model may be compared against the previous models.

This chapter is structured as follows. A methodology section (§4.2) first includes a technical description of the LES model used in this thesis (§4.2.1), followed by details of the LES model's configuration (including the different model grids tested) for the neutral ABL case (§4.2.2). The configuration of the new SB model (as well as the other SGS models tested in this chapter) is also given separately (§4.2.3). Results are then presented and discussed (§4.3); the characteristics of the backscatter acceleration fields generated by each tested SB model are first examined in isolation (§4.3.1), followed by an analysis of their effects on the LES fields

(§4.3.2). The additional CPU time required by the new SB model is also assessed and compared against the additional CPU time required by simply increasing the grid resolution with the Smagorinsky model (§4.3.3). Finally, the results are summarised and conclusions drawn (§4.4).

It is noted that some of the materials in this section have previously been published in the following peer-reviewed journal article: O'Neill *et al.* (2015).

4.2 Methodology

4.2.1 The RAMS LES model

Colorado State University's Regional Atmospheric Modelling System (RAMS) is used throughout this thesis. RAMS was originally developed by Pielke *et al.* (1992) for simulating and forecasting meteorological phenomena. Cai (1999) later adapted RAMS version 2a, at the University of Birmingham, for simulating the boundary layer over an idealised urban surface. This is the version of RAMS that forms the basis for the neutral ABL simulations undertaken in this chapter, with additional coding performed in order to implement the new SB model (Chapter 3), as well as the MT92 and WM08 models. The code is written in the FORTRAN 77 programming language.

The dynamic core of RAMS is scale independent; it adopts the finite volume method to solve the primitive equations on a staggered Arakawa-C grid, using a flux conservative leapfrog time differencing method, and has 2nd order spatial accuracy. The option to solve the non-hydrostatic compressible equations is selected. As only dry neutral atmospheric flows are considered in this study, no convective, cloud microphysics, moisture or radiation parameterisation is selected.

4.2.2 LES model configuration

For the neutral ABL simulations described in this chapter, the specified initial profiles are for a fully neutral boundary layer, with a constant potential temperature of 300 K throughout the entire depth of the domain, and a wind profile based on the Ekman spiral at latitude 45° with a geostrophic wind speed of $U_g = 5$ m s^{-1}. Other selected parameters include a von-Kármán constant of $\kappa = 0.35$, following the analysis by Businger *et al.* (1971) of the ABL observations carried out in Kansas in 1968, a surface roughness of $z_0 = 0.1$ m and a model time-step of $\Delta t = 0.3$ s. A Monin-Obukhov boundary condition is applied at the first grid level above the surface (at $z = z_1$) which, for the neutral case, enforces a horizontal wind speed of $U(z_1)/u_* = (1/\kappa)\ln(z_1/z_0)$. This is common practice in rough-wall geophysical flows, including in studies that (like the current one) also test the ability of LES to reproduce Monin-Obukhov similarity theory above the first grid level (e.g., Sullivan *et al.* (1994), Kirkil *et al.* (2012), Lu and Porté-Agel (2014)). However, as Sullivan *et al.* (1994) points out, this approach is only justified if the grid mesh is refined enough that at least part of the surface layer is explicitly resolved by the LES model. The depth of the neutral boundary layer scales with $u_*/|f|$, where f is the Coriolis parameter (Garratt, 1994). In the simulations performed here, $u_* = 0.2$ is a typical value for u_* and $f = 1.0 \times 10^{-4}$; a scaling height of $H = 2000$ m is thus defined, which is used to scale z in plots. For the Smagorinsky model runs, the so-called Smagorinsky coefficient is set to $C_S = 0.15$ (this is also the value used for the dissipative part of the SB model, which uses the Smagorinsky model).

To test the grid-independence of the new SB model (and confirm the grid-dependence of the previous models), a number of different grid aspect ratios are employed. Typical grid aspect ratios tested for LES studies of the neutral ABL fall within the range $\Delta_{AR} = \Delta x/\Delta z$ =1 to 10 (Sullivan *et al.*, 1994, Chow *et al.*, 2005, Mirocha *et al.*, 2012). Thus here the SB models are

tested on four different model grids that cover this range. 64×64 grid points are used in the x- and y- directions with $\Delta x = \Delta y$ = 50 m. For the vertical grid, Δz_1 is defined as the height of the lowest grid point above the surface, and a constant vertical grid stretch factor, $S_{\Delta z}$ = 1.03, is applied such that $\Delta z_{k+1} = S_{\Delta z} \times \Delta z_k$, until $\Delta z = \Delta z_{\max} = 50$ m, after which Δz remains fixed at $\Delta z_{\max}$ up to the top of the domain, at around 2500 m in all cases. This is summarised in Table 4.1.

Table 4.1 – LES grids
The LES model grids used for the neutral ABL simulations.

Grid	Δx (m)	Δy (m)	Nx	Ny	Δz_1 (m)	$\Delta x/\Delta z_1$	$S_{\Delta z}$	$\Delta z_{\max}$ (m)	Nz
G1	50	50	64	64	50	1	1.03	50	58
G2	50	50	64	64	25	2	1.03	50	79
G3	50	50	64	64	10	5	1.03	50	99
G4	50	50	64	64	5	10	1.03	50	128

Mean vertical profiles calculated from the LES output data (presented in §4.3.2) are the result of horizontal averages over all grid points on a given grid level and over 3 hours of simulation time, after a quasi-steady state is adjudged to have been reached. Note that there is no pressure gradient force applied across the domain, and so the total momentum in the system (which comes entirely from the initial condition) will reduce as the simulation progresses due to turbulent drag. However, this momentum loss occurs on a time-scale that is much longer than the averaging period used to obtain the flow statistics, and so the flow can be considered quasi-steady within this period.

4.2.3 SB model configuration

For the neutral ABL simulations described in this chapter, LES output obtained with the new SB model is compared against output obtained using the Smagorinsky model alone, as well as the MT92 and WM08 models, which have also been implemented into the RAMS LES code. To allow a direct comparison of the results obtained with each SB model, the following

parameters are set constant over each model, and are potentially different from those used in the original papers for the MT92 and WM08 models: For the new model, $\lambda = 1$ is used in Eq. (32), which defines a discrete Gaussian filter that is well approximated by the 1:4:6:4:1 filter on an isotropic grid; the 3-D 1:4:6:4:1 filter is thus used for both the MT92 and WM08 models. $n = 4$ is taken for the mixing length exponent in Eq. (27). The backscatter coefficient is set to $C_{\mathrm{B}} = 0.6$. A new backscatter acceleration field is generated every other model time-step, thus the time-scale of the backscatter acceleration fields is taken as $T_{\mathrm{B}} = 2\Delta t$. As discussed by Mason and Brown (1994), although a more realistic treatment of this time-scale is possible, a value of T_{B} on the order of the model time-step removes the need for Lagrangian-type following of fluid elements. Finally, as the influence of backscatter is minimal far enough above the near-surface region, computational expense can be spared by defining a maximum height, $z_{\mathrm{B_{max}}}$, below which the backscatter accelerations are added to the LES field. Here, $z_{\mathrm{B_{max}}} = 500$ m is used, which corresponds to a height of around $0.2H$. This is summarised in Table 4.2.

Table 4.2 – SGS models
The SGS models for the neutral ABL simulations.

Model	Reference	Filter	n	C_{B}	T_{B}	$z_{\mathrm{B_{max}}}$
SMAG	Smagorinsky (1963)	-	-	-	-	-
New	N/A	Eq. (32) with $\lambda = 1$	4	0.6	$2\Delta t$	500 m
MT92	Mason and Thomson (1992)	3-D 1: 4: 6: 4: 1	4	0.6	$2\Delta t$	500 m
WM08	Weinbrecht and Mason (2008)	3-D 1: 4: 6: 4: 1	4	0.6	$2\Delta t$	500 m

With the new SB model, an attempt is made to relate the backscatter anisotropy to the physical anisotropy of the subgrid scales by using measured velocity variance data. The velocity variance profiles reported by Grant (1986) (his Figure 5) in near-neutral conditions is used. It is noted that the reported variances encompass a wide range of turbulence length-scales, and it must be assumed that the variance ratios are characteristic of the variance ratios

at the subgrid scales. The data are somewhat simplified by taking the two horizontal variance components to be equal (to be consistent with the MT92 and WM08 models for the sake of later comparison) and a smooth exponential curve is fitted roughly through the data points, such that the velocity variance ratios at the surface are taken as $\sigma_u^2 : \sigma_v^2 : \sigma_w^2 = 4 : 4 : 1$, and are essentially isotropic above $0.2H$. Using Eq. (34), the imposed backscatter acceleration variance ratios are thus taken as $\sigma_{a_1}^2 : \sigma_{a_2}^2 : \sigma_{a_3}^2 = 8 : 8 : 1$ at the surface – the full variance ratio profiles are plotted in Figure 4.1(a). It is emphasised that these ratios might be considered as an example, used to demonstrate the new SB model, and that any other ratios that allow for realizable solutions of l_{B}^{ζ} could be applied. Figure 4.1(b) shows the resulting profiles (on grid G4 – see Table 4.1) of the normalised backscatter length-scale components, $l_{\mathrm{B}}^{\zeta}/\hat{l}_{\mathrm{B}}$, where $\hat{l}_{\mathrm{B}}$ is the backscatter length-scale in the isotropic flow interior. This plot also shows how the backscatter length-scale decreases close to the surface with the new SB model, in line with the subgrid mixing length-scale.

Finally, it is noted that the ability to control the backscatter VMF with the new SB model is not tested in this chapter (i.e. $\alpha = 0$ is used in Eq. (47)). Since this feature was not present in the MT92 or WM08 models, this allows the effect of the new grid-adaptive filter to be tested in isolation. The effect of varying the backscatter VMF is then analysed in the next chapter.

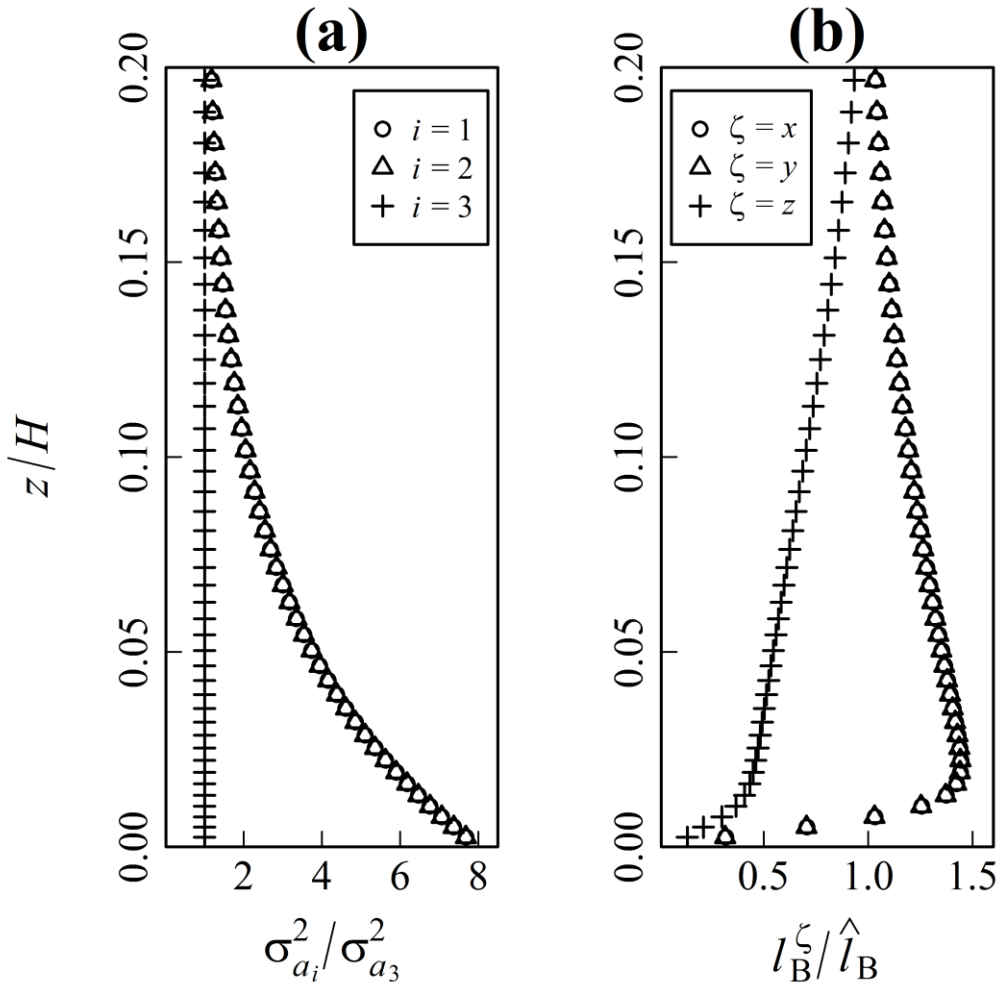

Figure 4.1 – Backscatter anisotropy and length-scale profiles
For the new SB model, (a) the imposed anisotropy in the backscatter acceleration fields, as shown by the acceleration variance ratio profiles; (b) the resulting profiles, on grid G4, of the backscatter length-scale components, l^{ζ}_{B}, normalised by the backscatter length-scale in the flow interior, $\hat{l}_{\mathrm{B}}$.

4.3 Results and discussion

4.3.1 Backscatter acceleration fields

Figure 4.2 shows surface layer contour plots through three example backscatter acceleration fields, generated using (a) the MT92 model, (b) the WM08 model, and (c) the new SB model, respectively, on grid G4 (which has a near-surface grid aspect ratio of $\Delta x/\Delta z \approx 10$). Each

plot shows point-wise acceleration magnitudes, i.e. $a = \sqrt{a_1^2 + a_2^2 + a_3^2}$, normalised by the maximum value within that field. The dissipation field used to calculate the local backscatter rate was taken from a quasi-steady LES, without backscatter, on the same grid. It can be seen that the backscatter is most significant within the lower part of the surface layer. With all three models, the characteristic length-scale of individual backscatter structures away from the surface scales reasonably with the horizontal grid spacing, and thus with the scale of the LES filter width. Nearer the surface, the backscatter length-scale can just be seen to begin to decrease with the new SB model, in line with the subgrid mixing length-scale, though this is hidden very close to the surface by the small acceleration magnitudes there. With the MT92 model, the backscatter anisotropy can be seen to depend on the local vertical grid spacing. Consequently, the field is excessively anisotropic on the highly refined near-surface grid. With the WM08 model, the backscatter seems to remain locally isotropic (with individual structures as tall as they are wide) at all grid levels, as expected from the interpolation method used to generate the acceleration fields. There are apparent discontinuities in the field at some grid levels, where individual backscatter structures seem to be slightly misaligned. However, this doesn't appear to affect the time-averaged LES statistics at these levels (shown later). The anisotropy within the backscatter acceleration field generated using the new SB model falls somewhere in-between the MT92 and WM08 models; it is neither fixed to the vertical grid spacing, nor spatially uniform, but looks to follow the imposed profile shown in Figure 4.1(a), with modest anisotropy close to the surface, becoming gradually more isotropic with distance from the surface. This is more formally verified next.

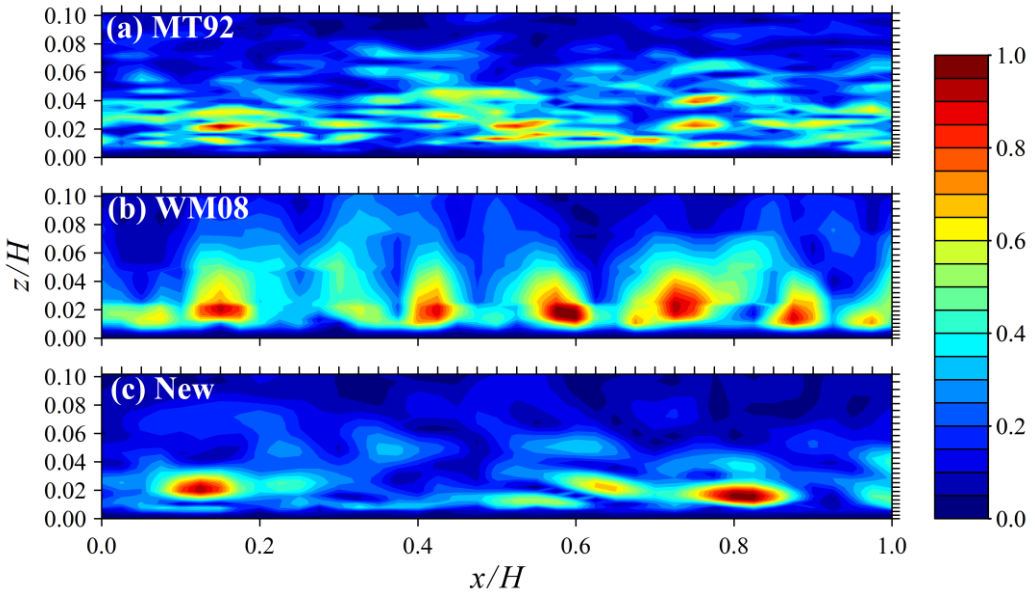

Figure 4.2 – Backscatter acceleration fields
Surface-layer contour plots through backscatter acceleration fields generated using each SB model: (a) MT92, (b) WM08, (c) new, on grid G4 (horizontal and vertical grid spacing is shown by outer tick marks on upper and right axes, respectively). Each field shows acceleration magnitudes and is normalised by its maximum value.

The spatial anisotropy within the backscatter acceleration fields described above is quantified in Figure 4.3, which shows, for each model, normalised surface-layer profiles of the three variance components, $\sigma^2_{a_1}$, $\sigma^2_{a_2}$ and $\sigma^2_{a_3}$, and their sum, which should equate to the target backscatter variance profile as given by the right hand side of Eq. (35) (also plotted for comparison). The data are normalised by the maximum of the target profile. The plots show that the target profile of summed variance components is well met by all three backscatter models. With the MT92 model, however, the vertical variances are considerably smaller than the horizontal variances at all grid levels, as a result of the application of the 3-D 1:4:6:4:1 filter on the vertically refined grid. Taking $\Delta x = \Delta y$ in Eq. (38), and assuming that $\Delta g_k \ll g_k$ (and thus that $g_{k+1} \approx g_k$), it follows that the ratio of the vertical variance to either of the horizontal variance components in the MT92 backscatter acceleration fields is

$$\frac{\sigma_{a_3}^2}{\sigma_{a_1}^2} = \frac{\sigma_{a_3}^2}{\sigma_{a_2}^2} = \frac{2}{1 + \Delta_{\mathrm{AR}}{}^2}, \tag{53}$$

where $\Delta_{\mathrm{AR}} = \Delta x / \Delta z_k$ is the local horizontal-to-vertical grid aspect ratio. Setting $\Delta_{\mathrm{AR}} = 10$ in Eq. (53), one can approximate the vertical variance component to be around 2% of the horizontal variance components near the surface (for grid G4). Such large anisotropy in the acceleration fields is detrimental to the performance of the backscatter model (as shown in later results) since, from a pragmatic point of view at least, the inclusion of backscatter is intended to reduce the excessive velocity shear in the surface layer, which can only be achieved through an increased vertical mixing of momentum. When horizontal variances dominate, the mixing of momentum is largely increased only within horizontal planes, and thus the effectiveness of backscatter acceleration fields in smoothing out the velocity shear profile is reduced. With the WM08 model, the backscatter is largely isotropic at all grid levels as a result of linearly interpolating the accelerations from an isotropic grid, as can be understood by setting $\Delta_{\mathrm{AR}} = 1$ in Eq. (53). With the new SB model, the observed backscatter anisotropy matches well with the imposed (target) anisotropy profile (shown by the dashed lines) at all grid levels. This confirms that the new grid-adaptive filtering procedure is able to control spatial variations in the backscatter anisotropy, allowing for physical consistency with the anisotropy of the subgrid scales.

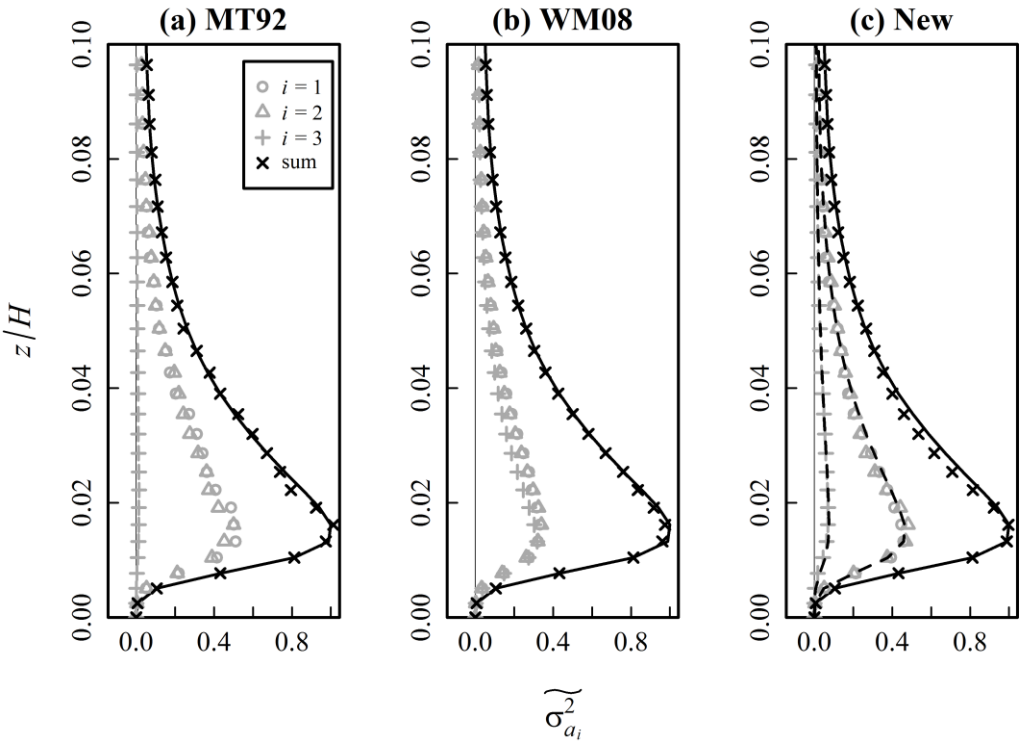

Figure 4.3 – Backscatter acceleration variance profiles
Surface-layer profiles of the three variance components, and their sum, for the three backscatter acceleration fields shown in Figure 4.2 for the (a) MT92, (b) WM08, and (c) new SB model. Solid line shows the target backscatter variance profile as given by the right hand side of Eq. (35). All values are normalised by the maximum of the target profile. For the new SB model, dashed lines show the expected variance profiles resulting from the imposed backscatter anisotropy (see Figure 4.1(a)).

The SB model should also aim to generate acceleration fields that contain minimal divergences. A divergence-free backscatter acceleration field ensures that the modified LES fields continue to satisfy conservation of mass. Conversely, any divergences in the backscatter acceleration fields may leave simulations prone to unphysical small-scale behaviour, and also lead to an unwanted reduction in the backscattered energy as a consequence of the pressure solver removing the resulting divergences from the velocity field (Weinbrecht and Mason, 2008). The curl operation that is performed during the generation of the backscatter acceleration fields removes all divergence from the fields. However, the application of the 'post-curl' vertical scaling factor, required at grid levels where real solutions to the 'pre-curl'

scaling factor g_k (Eq. (39)) do not exist, reintroduces divergences at those grid levels. Figure 4.4 summarises, for each SB model, the magnitude of the grid-cell divergences, i.e. $\left(a_1^{i+1,j,k} - a_1^{i,j,k}\right)/\Delta x + \left(a_2^{i,j+1,k} - a_2^{i,j,k}\right)/\Delta y + \left(a_3^{i,j,k+1} - a_3^{i,j,k}\right)/\Delta z_k)$, within the surface layer, for the same three example backscatter acceleration fields described above (generated on grid G4). The plots show normalised root-mean-square (RMS) values at each grid level (equivalent to the standard deviations, since their mean is zero). The accelerations have been normalised by $\sigma_a/\Delta_{\mathrm{eq}}$, where σ_a is the square root of the maximum of the target backscatter variance profile (given by the right hand side of Eq. (35)) and Δ_{eq} is 50 m in this case – this normalising factor scales with the magnitude of spatial variations of the largest backscatter accelerations. The plots show that real solutions of g_k exist throughout most of the surface layer, but the post-curl scaling factor is required at the lowest 4 or 5 grid levels (within the region $z/H \lesssim 0.01$) in each case, introducing divergences there as a consequence. The largest divergences exist within the backscatter acceleration fields generated with the WM08 model. The divergences are around half the size with the new SB model, and considerably smaller with the MT92 model. The magnitude of the divergences corresponds to the level of anisotropy within the backscatter acceleration fields, and is related to the use of the curl operator in the region where the backscatter rate profile falls sharply to zero at the surface from its maximum at around $0.02H$; as the operator involves differences between adjacent grid levels, it is easier to accommodate such a sharp vertical gradient as the autocorrelation between the two adjacent grid levels is reduced. With the new SB model, the magnitude of divergences within backscatter acceleration fields thus depends on the imposed level of anisotropy. As would be expected, the new SB model divergence profiles are almost identical to the MT92 and WM08 model profiles when the anisotropy level is set to match that of the respective model (not shown).

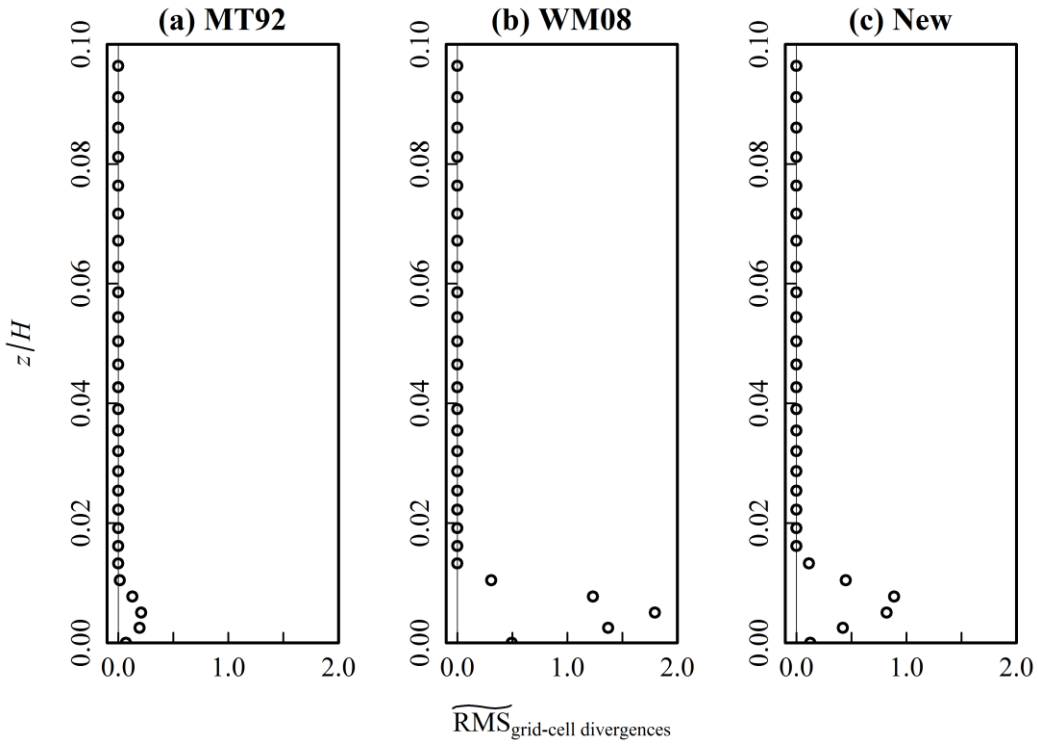

Figure 4.4 – Backscatter acceleration divergence profiles
Surface-layer profiles of the normalised RMS grid-cell divergences for the three backscatter acceleration fields shown in Figure 4.2 for the (a) MT92, (b) WM08, and (c) new SB model. See text for more details.

4.3.2 LES fields

The performance of the new SB model against the other tested SGS models (see Table 4.2) is assessed from the surface-layer profiles of mean nondimensional velocity shear, Φ_{M}. One set of profiles is plotted for each model grid tested (see Table 4.1). The profiles are normalised such that the expected value is equal to 1 within the neutral surface layer, which follows from differentiation of the neutral logarithmic wind profile (see Eq. (13) and note that $dU/dz = \sqrt{(\partial u/\partial z)^2 + (\partial v/\partial z)^2}$ is taken). The resulting profiles are shown in Figure 4.5.

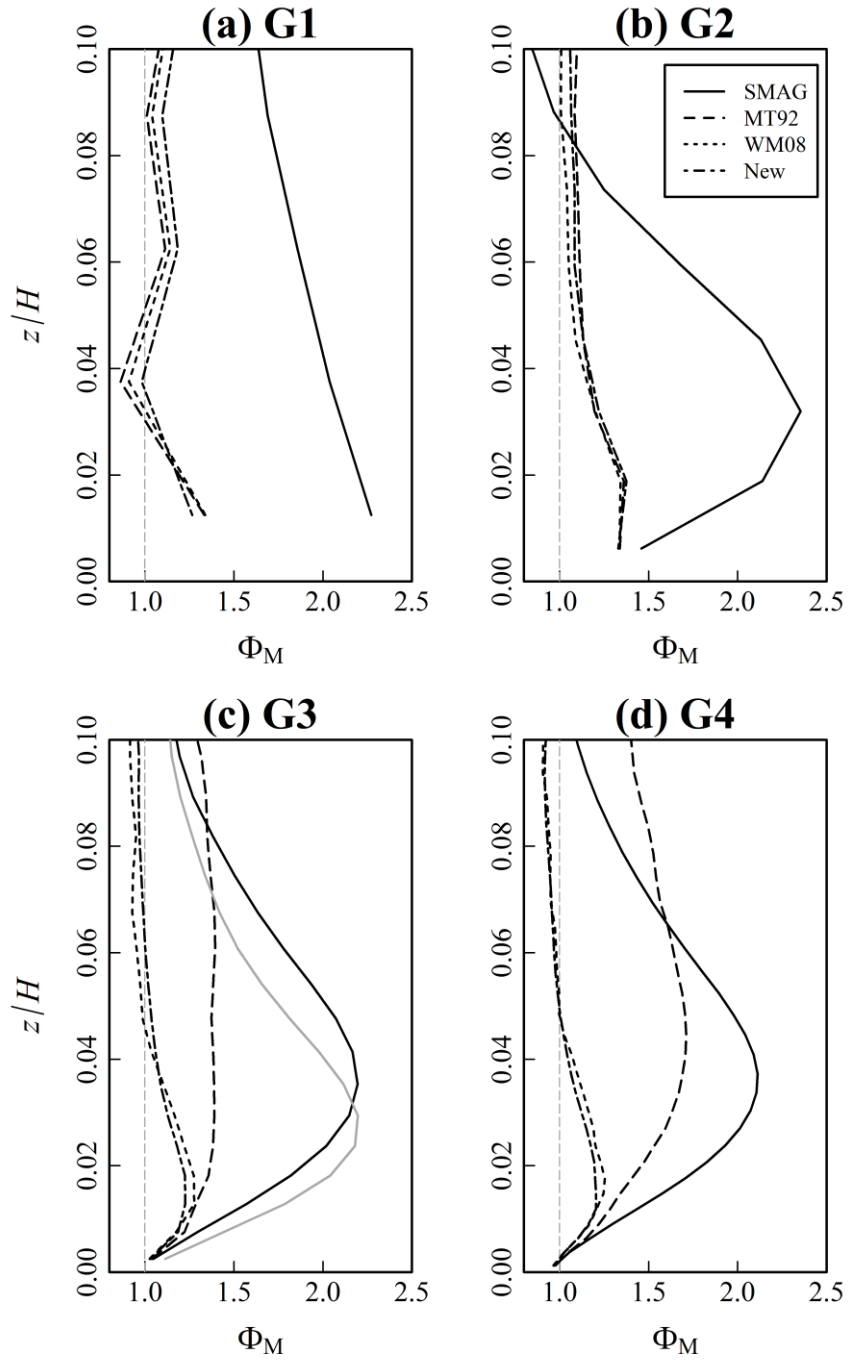

Figure 4.5 – Velocity shear profiles

Surface-layer profiles of mean nondimensional velocity shear, Φ_M, obtained with each SGS model, for each model grid: (a) G1, (b) G2, (c) G3, and (d) G4. The grey dashed lines through $\Phi_M = 1$ corresponds to the theoretical profile for a neutral surface layer. The lowest grid point is set by the surface boundary condition and so is not plotted. The solid grey line in panel (c) shows the profile obtained with the SMAG model when the grid resolution is increased such that the additional required CPU time is similar to that required for the backscatter models (discussed in §4.3.3).

The profiles show that the new SB model is able to significantly reduce the maximum of the 'overshoot' in Φ_M (from that obtained without backscatter, i.e. with the Smagorinsky model alone) towards the expected value of 1. Importantly, this reduction appears to be largely independent of the level of vertical grid refinement, at least for the cases tested here, which span a grid aspect ratio range of $\Delta_{AR} = \Delta x/\Delta z = 1$ to 10. The Φ_M maximum is reduced from 2.27 to 1.27 on grid G1, from 2.35 to 1.38 on grid G2, from 2.19 to 1.23 on grid G3, and from 2.11 to 1.21 on grid G4, thus giving a typical reduction of around 80%. The height of the Φ_M maximum is also brought closer to the ground with the backscatter model, occurring at around 1/3 of the surface-layer depth without backscatter and around 1/6 of the surface-layer depth with backscatter (though the vertical resolution is too coarse to confirm this for grid G1). The performance of the new SB model is fairly similar to that of the WM08 model; however, there is a further improvement of around 5% with the new SB model in reducing maximum excessive Φ_M on three of the four grids tested (G1, G3 and G4). Conversely, the reduction in the Φ_M overshoot with the MT92 model is shown to depend heavily on the grid aspect ratio. On an isotropic grid (G1), the model is essentially as effective as the other two backscatter models; this is not surprising, since the MT92 backscatter acceleration fields are fully isotropic in this case. The model appears to remain effective for grids with modest anisotropy, i.e. on grid G2 with $\Delta_{AR} = 2$. However, for larger aspect ratios (grids G3 and G4), the reduction in Φ_M becomes less pronounced as the vertical grid refinement within the surface layer increases. This illustrates how an overly-large level of anisotropy within the backscatter acceleration fields can act to reduce the effectiveness of the backscatter model due to a reduction in the downward mixing of momentum from the upper part of the surface layer. Mirocha *et al.* (2010) found that the expected similarity solution for wind speed within the surface layer is best reproduced by the Smagorinsky model for grid aspect ratios of around

$\Delta_{AR} = 4$; it is thus reasoned that the range of grid anisotropies over which the MT92 model remains effective is too small.

There are two key reasons for the justification of the new SB model, despite the relatively small difference in performance from the WM08 model for the simulations performed here:

i. ***Improved physics*** – The new SB model is able to control the backscatter length-scale (eddy-size) and anisotropy (eddy-shape). This means that the inclusion of backscatter can be implemented in a manner that is more physically consistent with reality. One of the principles of backscatter theory dictates that the dominant backscatter length-scale from the unresolved (SGS) to the resolved scales should match the local grid-scale (Mason and Thomson, 1992). The new SB model follows this principle closely from the middle of the boundary layer down through the surface layer. The WM08 model, however, violates the principle in the surface layer, since the backscatter length-scale is fixed everywhere at the grid-scale of the flow interior. Thus, within the surface layer, where eddy sizes are smaller and turbulence structure is known to be anisotropic with smaller vertical than horizontal extent (Kaimal *et al.*, 1972), the vertical length-scale is unphysically large. From a spectral point of view, this corresponds to energy being added at inappropriately large wavelengths (or small wave-numbers). The WM08 model thus induces an unfairly high degree of vertical mixing, bringing higher momentum flow down towards the region of excessive velocity shear and smoothing out the overshoot there. It is therefore to the new SB model's credit that it performs at least as well as the WM08 model despite this – reasons for why this might be the case are given after (ii).

ii. ***Wider applicability*** – The simulations performed in this chapter (of a fully neutral ABL over homogeneous, flat terrain) require LES grids with vertical stretching only, thus making it possible to test and compare both models (new and WM08), which are both applicable on such grids. However, the WM08 model is not applicable in more complex modelling cases in which local 3-D grid refinement is utilised, since the backscatter length-scale is fixed and so cannot be varied spatially to account for local changes in the LES filter width, whereas the new SB model is capable of doing this.

One might have expected a monotonic relationship between the reduction in maximum excessive Φ_M and the level of anisotropy within the backscatter acceleration fields, on the presumption that larger anisotropy (with smaller vertical variances than horizontal) results in less vertical mixing of momentum and thus a larger maintained velocity gradient within the surface layer. However, the results obtained e.g. on grids G3 and G4 comparing the new SB model (anisotropic) with the WM08 model (isotropic) show that this is not always the case. Two possible reasons are proposed for this. Firstly, it is noted that with increasing anisotropy in the backscatter acceleration fields, there are smaller near-surface divergences which will thus result in smaller associated losses of the backscattered energy. It is possible that the reduction in vertical mixing due to the larger anisotropy (where fluid parcels are 'pushed' more towards horizontal directions than up or down) is not as great as the reduction in vertical mixing due to the backscatter energy loss (where fluid parcels are not pushed up or down with the maximum desired force), resulting in a more pronounced reduction in the mean velocity shear profile with the new model than with the WM08 model. Secondly, it is hoped that when the backscatter length-scale and anisotropy are more closely matched to the grid-scale turbulence length-scale and anisotropy within the LES flow-field, the backscatter accelerations will be more readily 'taken up' by the grid-scale flow structures, and

consequently more effective in reducing the Φ_M overshoot. Either way, the results demonstrate that by controlling the spatial structure of the backscatter acceleration fields, the new SB model is, in some cases, able to further reduce excessive Φ_M over that which is possible with fully isotropic backscatter.

It is encouraging to note the similarity between the WM08 and MT92 profiles in Figure 4.5(c) and the equivalent profiles in the Weinbrecht and Mason (2008) paper (their Figure 1, left – reproduced in Figure 4.6 below), which were plotted from runs on a similar model grid and in neutral conditions. Although the maximum absolute value of Φ_M within the surface layer is slightly larger in the simulations performed here than in theirs, this is also true for the profiles without backscatter (i.e. with the Smagorinsky model alone), and the percentage reduction in excessive Φ_M remains similar. It is therefore reasoned that the absolute differences are simply a result of the different LES codes used in each study. It is also noted that it is possible to reduce the excessive velocity shear within the lower part of the surface layer further towards 1 by increasing either the backscatter coefficient, C_B, or the filter width (i.e. increasing λ in the new SB model). However, it was found that this can often lead to an over-reduction in Φ_M (i.e. values below 1) in the upper part of the surface layer (not shown for brevity). An attempt has not been made here to find the optimal 'tuning' of the SB model parameters, since the main focus of interest is in comparing the relative performance of the new SB model against the previous models for any given set of reasonable parameters.

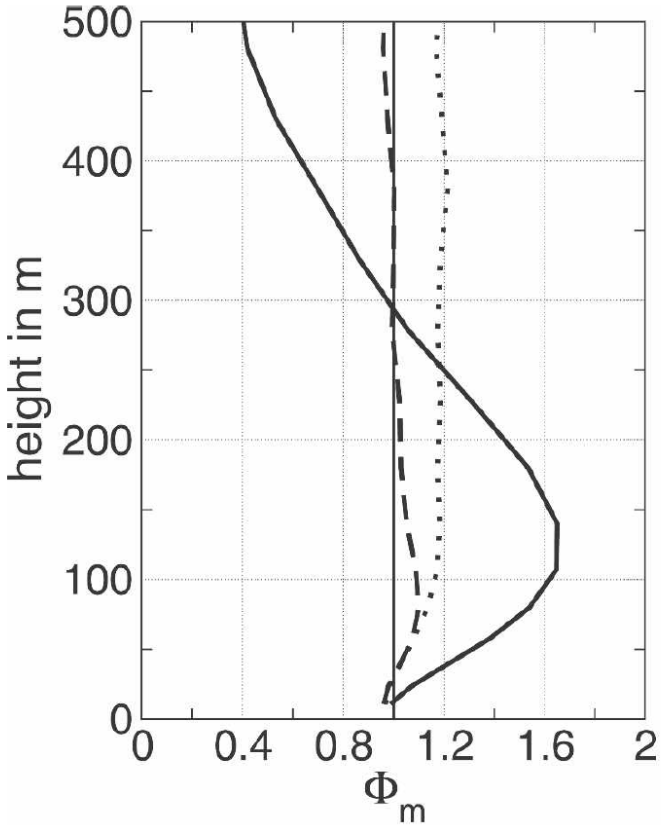

Figure 4.6 – Profiles from WM08 paper
Taken from Weinbrecht and Mason (2008), Fig. 1 (left): "Profiles of the nondimensional velocity gradient, Φ_M". Solid line–SMAG; Dotted line–MT92; Dashed line–WM08.

The backscatter acceleration fields constitute a continuous modification to the LES fields which, it is argued, bring the model closer towards reality. Similarly, should the backscatter acceleration fields be abruptly removed, one would expect the model to tend back towards its original state, further from reality. There should therefore exist a time-scale over which this change occurs, which might be interpreted as a physical time-scale associated with the effects of backscatter at the grid-scale. An attempt to objectify this time-scale is made in the following way. A quasi-steady simulation without backscatter is taken as a starting point; here, the SMAG run performed on grid G3 is used for this. Each backscatter model is then turned on and the subsequent changes to the LES fields are observed. Specifically, the value of the maximum nondimensional velocity shear within the surface layer, $(\Phi_M)_{max}(t)$, or $S(t)$ for short, is tracked, and the resulting time-series plotted. This is shown in Figure 4.7, along

with a fitted exponential trend-line for each model (as described below). The raw time series have been smoothed with a 5-minute moving average filter to remove small (high frequency) fluctuations for the benefit of plotting. The relative success of a particular backscatter model can again be assessed by examining its ability to bring the maximum nondimensional velocity shear towards the expected value of 1.

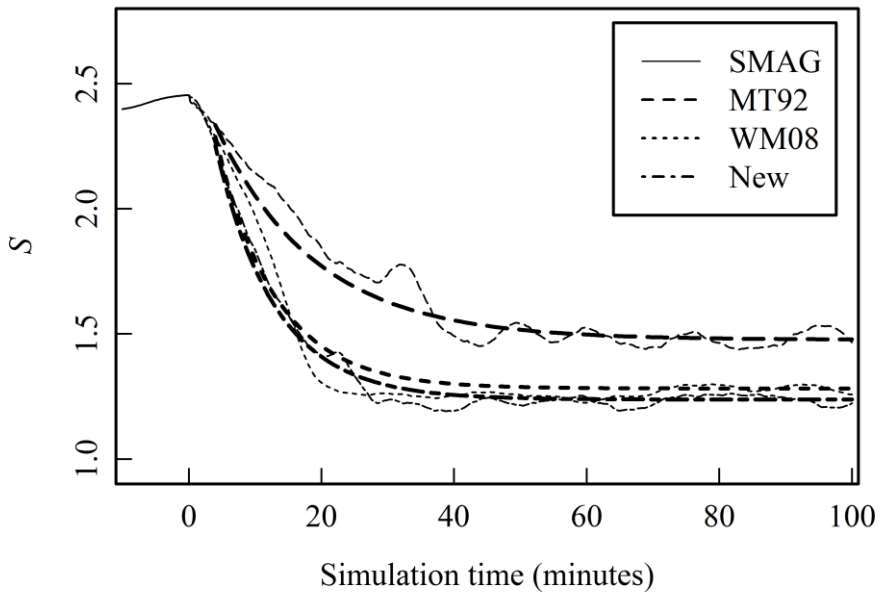

Figure 4.7 – Velocity shear time-series
LES time-series (thin lines) and fitted exponential trend-lines (thick lines) of maximum nondimensional velocity shear, S, within the surface layer, after each SB model (MT92, WM08, new) is activated from an initially quasi-steady state without backscatter (SMAG), on grid G3.

The time-series suggest the existence of a 'backscatter adjustment time-scale' that is largely independent of the chosen backscatter model. An exponential trend-line is fitted to each of the time-series, of the general form:

$$S(t) = (S_0 - S_\infty)e^{-t/\tau} + S_\infty, \tag{54}$$

where S_0 is the initial value of S, and S_∞ is the final quasi-steady value of S, which is taken to be the mean value of S over the last third of the simulation period. It is found that a good fit

can be obtained for all models with an e-folding time of $\tau \approx$ 10-15 minutes. This backscatter adjustment time-scale is comparable with the turnover time-scale of surface-layer eddies, which is of order $\Delta_{\mathrm{SL}} / \sigma_{U,\mathrm{SL}} \approx 200/0.3 \approx 11$ minutes, where Δ_{SL} is the depth of the surface layer and $\sigma_{U,\mathrm{SL}}$ is a typical value for the square root of velocity variance within the surface layer (which has been approximated from Figure 4.8, shown later). This suggests that the largest surface-layer eddies constitute the most important mechanism through which the imposed backscatter accelerations eventually redistribute momentum, and thus reduce velocity shear, within the surface layer.

Figure 4.8 shows near-surface profiles of resolved velocity variance for the LES runs on model grid G4, obtained with the Smagorinsky model and each of the SB models. In the figure, the curves for $i = 1,2,3$ correspond to the curves for σ_u^2, σ_v^2 and σ_w^2, respectively. On their own, the backscatter acceleration fields provide a direct (positive) source of velocity variance to all three components. However, in all cases, it is observed that the overall effect of backscatter is to redistribute the velocity variance among the three components so as to increase near-surface isotropy of the flow-field. This is seen as a reduction of the streamwise component and an increase in the crosswind and vertical components. The backscatter acceleration fields provide the means by which momentum from the upper part of the surface layer is mixed down towards the lower part, thereby reducing the excessive velocity shear observed when backscatter is not modelled. These results agree closely with Mason and Thomson (1992) who observed a similar redistribution among the three components of velocity variance, bringing them closer to the ratios observed in the upper surface layer by Grant (1986) in near-neutral conditions.

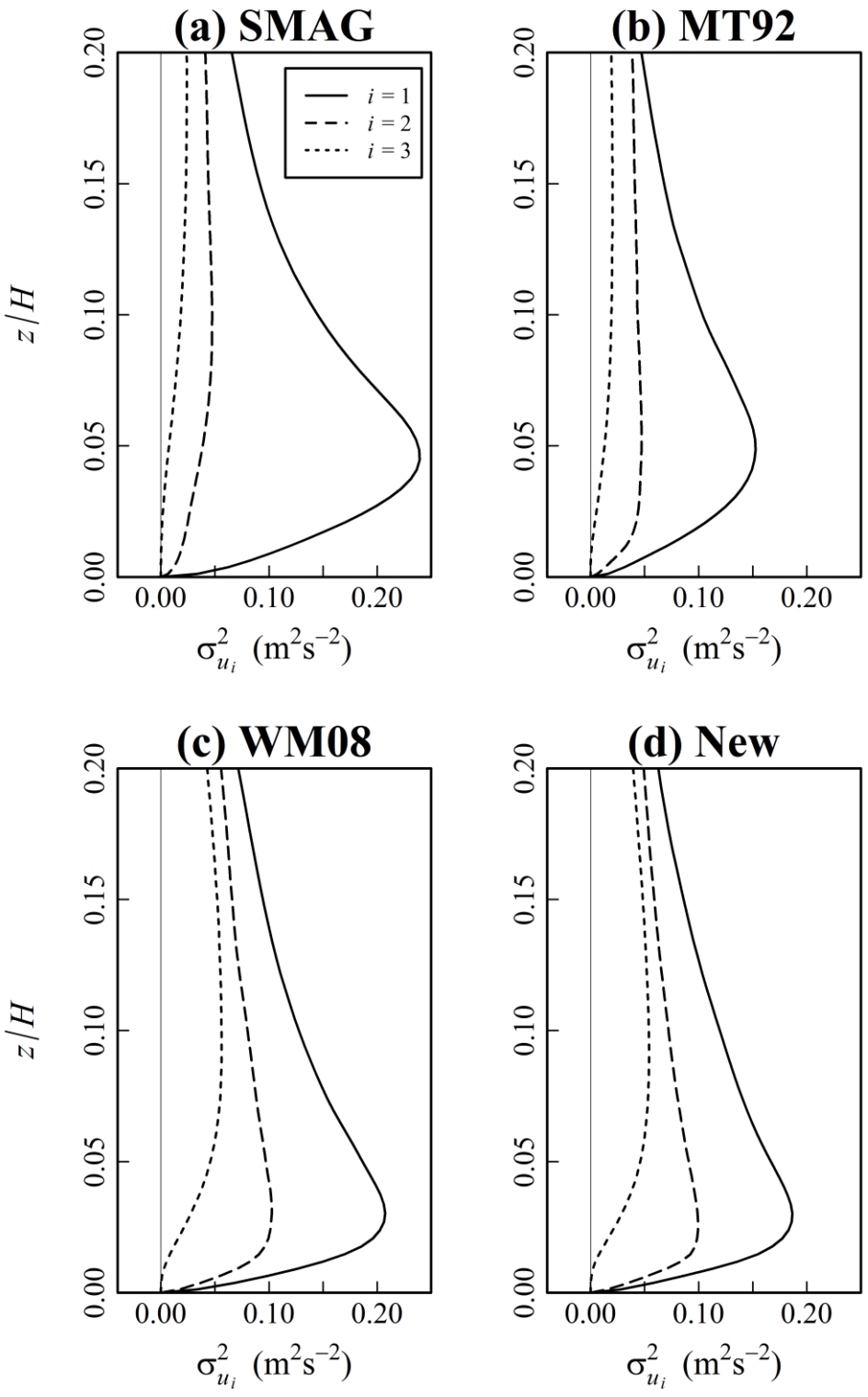

Figure 4.8 – Velocity variance profiles

Near-surface profiles of resolved velocity variances, σ_u^2, σ_v^2 and σ_w^2, (on grid G4) obtained with each SGS model: (a) SMAG, (b) MT92, (c) WM08, (d) new.

4.3.3 Additional CPU time

Finally, the additional CPU time required by the new SB model, over equivalent simulations without backscatter (i.e. with the Smagorinsky model alone) is reported. For a given simulation, this will vary with the SB model parameters selected, in particular the height below which the backscatter accelerations are added to the LES fields, $z_{\mathrm{B}_{\max}}$, the filter width parameter λ (and the number of standard deviations away from the filter centre point used for the discrete Gaussian filter kernel), and the time between each newly generated backscatter acceleration field, T_{B}. However, as an example, assessing the LES runs performed here on grid G3, the simulation with the new SB model required approximately 50% additional CPU time than the simulation with the Smagorinsky model alone. Although this could be considered a fairly large computational cost, it is possible to get a better indication of the relative benefit of the backscatter model by comparing the surface-layer profile of mean nondimensional velocity shear Φ_{M} obtained with the SB model on grid G3 against the profile obtained with the Smagorinsky model when the grid resolution is increased such that an additional 50% CPU time is required (for the same simulation time period). To this end, a simulation was run in which the horizontal grid resolution was increased from $\Delta x = \Delta y = 50$ m to around 40 m and $\Delta z_{\max}$ was reduced to 40 m (whilst the domain extent was kept roughly the same in each dimension), and the model time-step was reduced accordingly from $\Delta t = 0.3$ s to $\Delta t = 0.25$ s. In fact, this simulation required almost twice as long (94% extra CPU time) to complete than with the original grid. Despite this, the results are still clear – increasing the grid resolution with the Smagorinsky model *does not* remedy the problem of erroneous velocity shear within the surface layer; it simply acts to shift the velocity shear profile maximum towards the surface (compare the solid grey and black lines in Figure 4.5(c)). This result has also been observed in previous studies (Mason and Thomson, 1992,

Chow *et al.*, 2005). It may thus be concluded that the SB model adds significant worth to the simulation for its computational cost that cannot be achieved by an increase in grid resolution with the Smagorinsky model alone. An additional advantage is that the imposed backscatter accelerations act to induce fully developed turbulence much faster than with the Smagorinsky model alone; thus a statistically steady state was achieved significantly more quickly with the backscatter model (typically around 5 hours) than with the Smagorinsky model alone (typically around 10 hours) in the simulations performed here. Figure 4.9 shows time-series of bulk (i.e. domain-averaged) RS-TKE for each SGS model on grid G4, which can be used to indicate how quickly each simulation attains a quasi-steady state (by judging when each time-series starts to 'level off'. Note that the slightly downward linear trend later in each simulation period is due to the fact that the total momentum in the system is gradually being lost to surface friction). These findings are again corroborated by previous work (Weinbrecht and Mason, 2008) – refer to Figure 2.5.

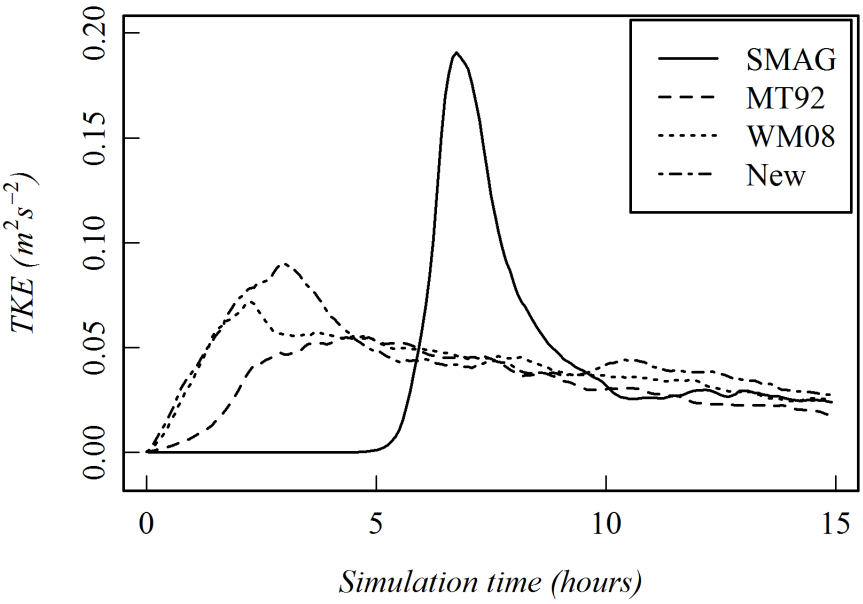

Figure 4.9 – Bulk TKE time-series
LES time-series of bulk RS-TKE, for each SGS model, on grid G4; used to indicate how quickly each simulation attains a quasi-steady state.

4.4 Summary and conclusions

In this chapter, the new SB model presented in Chapter 3 was tested for the case of LES of the neutral ABL over flat, homogeneous terrain, on a number of model grids, each with a different level vertical grid refinement. Its performance was compared against that of the MT92 and WM08 models, in terms of its ability to reduce excessive nondimensional velocity shear within the surface layer, as seen with the Smagorinsky model alone, towards the expected value of 1. The new SB model was shown to significantly reduce the velocity shear 'overshoot' maximum by an amount that is largely independent of the near-surface grid aspect ratio, and typically around 80%. Conversely, the effectiveness of the MT92 model was shown to depend heavily on the level of grid refinement, with significant reduction in model performance as the vertical resolution is increased, due to an associated reduction in the vertical mixing of momentum within the surface layer. The effectiveness of the WM08 model was similar to that of the new SB model; however, the value of the new model lies in its wider applicability in cases where 3-D grid refinement is used (rather than just vertical grid refinement), which can be exploited in further work. It was also shown that although the additional CPU time required by the SB model over the Smagorinsky model is not insignificant, the improvement in simulation accuracy that it offers cannot be achieved by simply increasing the grid resolution with the Smagorinsky model.

The level of divergences within the backscatter acceleration fields generated by the new and existing SB models was also analysed. Divergences leave simulations prone to unphysical small-scale behaviour and lead to an unwanted reduction in the backscattered energy, and should therefore be minimised. Divergences are reintroduced into the initially divergence-free acceleration fields at grid levels very close to the surface ($z/H \lesssim 0.01$) where the application of a 'post-curl' scaling is required in order to ensure the correct horizontally-averaged energy

input. The magnitude of these divergences was shown to correspond to the level of anisotropy within the backscatter acceleration fields; thus the smallest divergences were seen with the MT92 model (most anisotropic) and the largest ones with the WM08 model (fully isotropic), with the new SB model divergences falling somewhere in-between depending on the imposed level of backscatter anisotropy.

A backscatter adjustment time-scale, corresponding to the e-folding time for the rate of reduction in excessive velocity shear within the surface layer, was also identified and found to be of the order of 10-15 minutes for all the SB models tested. This is also the time-scale associated with the turnover time of the largest surface-layer eddies, indicating their importance as a mechanism through which the imposed backscatter accelerations can redistribute momentum, and thus reduce velocity shear, within the surface layer.

In conclusion, the grid-independence of the new SB model was confirmed via LES of the neutral ABL, and shown to be at least as effective as existing SB models in reducing the excessive velocity shear, as predicted by the Smagorinsky model, within the surface layer. The second research objective (§2.4) has therefore been satisfied. The next step is to exploit the capabilities of the new SB model to test whether simulation accuracy can also be improved in LES of other neutral atmospheric flows, in particular those in which grid-scale backscatter is again an important physical process that should be explicitly handled by the SGS model. One such example is LES of street canyon flow, which is the focus of the next chapter.

5. STREET CANYON FLOW

5.1 Introduction

This chapter addresses research objective #3, as stated at the end of §2.4 and repeated below for convenience:

> **Objective #3**: Assess whether the new SB model can also help improve simulation accuracy (from that obtained with the Smagorinsky model) of neutral street canyon flow, in which the roof-level shear layer is under-resolved, using a wind-tunnel dataset for validation.

As discussed in §2.2.4, previous LESs of street canyon flow have shown an under-prediction in the intensity of the primary eddy that forms within the street canyon (Liu and Barth, 2002, Cui *et al.*, 2004, Cheng and Liu, 2011a, Liu and Wong, 2014), indicating a lack of momentum transfer across the roof-level shear layer. It was hypothesised in §2.4 that this discrepancy is due to the inability of the SGS model (in these cases) to account for important grid-scale backscatter that occurs in the highly energetic, but typically under-resolved, roof-level shear layer. Since the application of an SB model to simulation of street canyon flow has, to the author's knowledge, not been performed to date, this hypothesis remains untested; the work in this chapter is intended to fill this knowledge gap.

This chapter is structured as follows. In the methodology section (§5.2), the configuration of the LES model (§5.2.1) and the new SB model (§5.2.2) for the street canyon flow case are each given separately. Details of the wind-tunnel (WT) experiment used to validate the LES output are also given (§5.2.3). Results are then presented and discussed (§5.3); simulation accuracy for each LES run is analysed by comparing mean velocity profiles (from which the primary eddy intensity can be inferred) (§5.3.1) and mean TKE profiles (§5.3.2) inside the

street canyon with the WT data, and the roof-level air exchange rate is also calculated for each LES run to assess the change in entrainment rate with the inclusion of backscatter (§5.3.3). Finally, a summary of the results and the main conclusions are presented in §5.4.

It is noted that some of the materials in this section have previously been published in the following peer-reviewed journal article: O'Neill *et al.* (2016).

5.2 Methodology

5.2.1 LES model configuration

The RAMS model, described in §4.2.1, is again used for the street canyon (flow and dispersion) simulations. After the developments of Cai (1999) for simulating the boundary layer over an idealised urban surface, the model was further developed by Cui *et al.* (2004), again at the University of Birmingham, for simulating the flow-field within an idealised urban street canyon. This version forms the basis for the street canyon simulations performed in this (and the next) chapter, with additional coding performed in order to implement the new SB model. Information about the coding structure of the new SB model is given in an appendix at the end of this thesis (APPENDIX: FORTRAN CODE EXTRACTS).

The LES modelling domain for the street canyon flow simulations is schematised in Figure 5.1. The street canyon has dimensions $H = W = 18$ m, making it 120 times larger than the WT street canyon. Given that the kinematic viscosity of the modelled flow is assumed to be that of air in standard conditions (i.e. $\nu \approx 1.6 \times 10^5$ m^2 s^{-1}), the effective Reynolds number based on H and the maximum free-stream velocity is approximately $Re \approx 3 \times 10^6$. For such a high-*Re* flow, molecular viscosity can be assumed negligible compared with the SGS stresses, and is therefore not included in the numerical simulations. Full-scale experimental datasets of high enough quality to validate LES model output are lacking due to the

difficulties associated with controlling the external conditions in such experiments. Consequently, many WT experiments have been conducted using similar block sizes to Brown *et al.* (2000) for the purpose of assessing the mixing of momentum and scalars in street canyon flow, e.g. Kastner-Klein and Plate (1999), Pavageau and Schatzmann (1999), Salizzoni *et al.* (2009), and subsequently used for validation purposes in full-scale numerical studies, e.g. Walton and Cheng (2002), Cui *et al.* (2004), Cai *et al.* (2008), Letzel *et al.* (2008). The x (across-canyon), y (along-canyon) and z (vertical) extent of the domain are $L_x, L_y, L_z = 24\ \text{m}, 40\ \text{m}, 94\ \text{m}$, respectively. The open boundaries in x and y are treated as periodic, implying an infinitely long (repeating) canyon in y and an infinite number of repeated street canyons in the streamwise direction. Constant grid spacings of $\Delta x = 0.3\ \text{m}$ and $\Delta y = 1\ \text{m}$ are used in the streamwise and spanwise directions, respectively. The number of grid points in each of these directions is thus $N_x = 81$ and $N_y = 40$. In the vertical direction, there are $N_z = 91$ grid levels; a constant grid spacing of $\Delta z = 0.3\ \text{m}$ is used between the ground and $z/H = 1$, and Δz is then gradually stretched such that $\Delta z = 5\ \text{m}$ by the top of the domain.

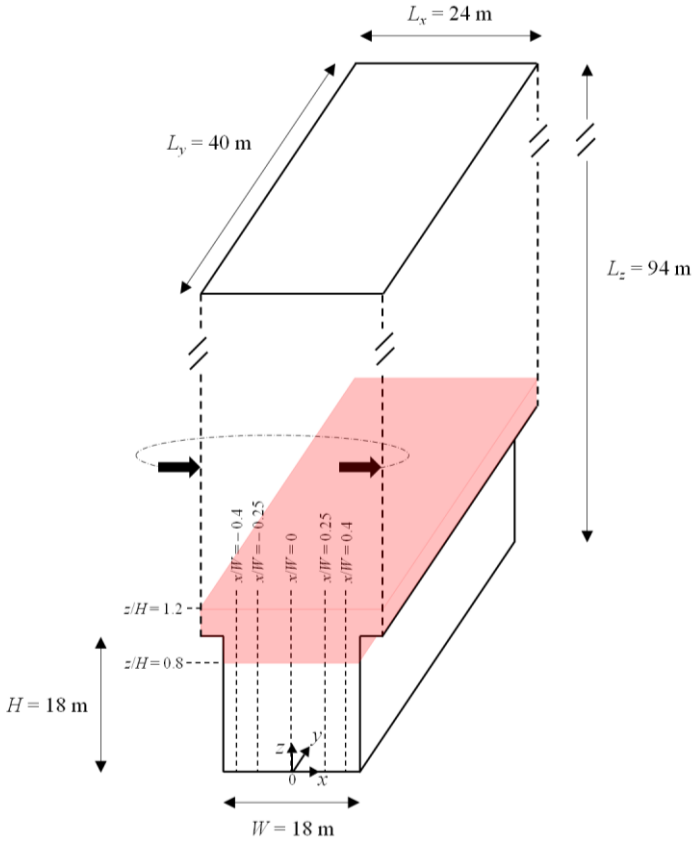

Figure 5.1 – Schematic of LES domain
Dimensions of the LES computational domain for street canyon simulations. Vertical dashed lines within the street canyon show the five transects along which time-averaged statistics are computed for comparison with the wind-tunnel data. Periodic boundary conditions are used in x (above roof-level) and y. The red shaded region shows where the backscatter accelerations are added to the LES field (discussed in §5.2.2 next).

The initial wind profile is logarithmic, starting from zero at the street canyon roof level (velocities are zero within the canyon) and reaching a maximum of 2.6 m s^{-1} at the domain lid. A rough-wall boundary condition is used at solid surfaces, with normal velocities set to zero and tangential velocities based on a logarithmic profile. The use of a smooth-wall boundary condition, which would require a grid resolution fine enough to resolve up to the viscous sublayer, is unfeasible for atmospheric (high Re) flows. Although the need for better rough-wall models in simulations of complex flows such as the one presently considered is recognised within the LES community (Piomelli and Balaras, 2002), the logarithmic wall

function is still, to the author's knowledge, the best and simplest choice available for rough walls, and widely adopted by numerous LES studies of flows over building-like obstacles in the past, e.g. Santiago *et al.* (2010), Park and Baik (2013), Cheng and Porte-Agel (2015). A zero-gradient boundary condition is used for velocity at the top of the domain.

The baseline Smagorinsky SGS model uses a fixed coefficient of $C_S = 0.1$. Mason and Callen (1986) reported that this value gives optimum behaviour in practical simulations of neutral flow, and that values as large as the theoretical one for homogeneous isotropic turbulence (Lilly, 1967) give excessive damping of the resolved scale motions. A number of LES studies of neutrally stratified flows have adopted similar values for the Smagorinsky constant, e.g. Xie *et al.* (2004), Boppana *et al.* (2010), Santiago *et al.* (2010). A model time-step of $\Delta t = 0.04$ s is used. Based on the maximum free-stream velocity, this gives a Courant–Friedrichs–Lewy (CFL) number (which must be below one for convergence of the finite-difference approximation) of 0.797.

All simulations are run for 75 minutes, which corresponds to around 25 turnover times of the primary eddy within the street canyon, with data from the last 15 minutes of each simulation used to calculate average flow statistics. As the mean flow-field is 2-D, data are also averaged in the homogeneous spanwise (y) direction. As in the previous chapter, there is no pressure gradient force applied across the domain, and so the total momentum in the system will reduce over time. Again, however, this occurs on a time-scale that is much longer than the averaging period used to obtain the flow statistics, and so the flow can be considered quasi-steady within this period.

5.2.2 SB model configuration

For the street canyon flow simulations, the new SB model is compared against the Smagorinsky SGS model only, using WT data for validation. The SB model is used to account for important grid-scale backscatter within the under-resolved roof-level shear layer, rather than within a near-surface shear layer as in the case of the neutral ABL (Chapter 4). Away from surfaces, it is assumed that $l = l_0$ in Eq. (26); the backscatter acceleration fields should therefore be scaled such that

$$\overline{a_1^2} + \overline{a_2^2} + \overline{a_3^2} = \frac{2C_\mathrm{B}}{T_\mathrm{B}}\epsilon. \tag{55}$$

For the neutral ABL case (Chapter 4), a number of different model grids are tested using a fixed set of SB model parameters. Conversely, here, the model grid is fixed and the effect of changing some of the SB model parameters is tested, with the WT data used to infer the most appropriate values. Namely, the SB model parameters that are varied are: the backscatter coefficient, C_B; the backscatter length-scale, l_B; and the backscatter VMF factor, $\mathrm{VMF_B}$. The different values tested for each of these parameters are discussed in turn below.

Since C_B typically takes a value within the range 0.6 – 1.4 (Chasnov, 1991, Mason and Thomson, 1992, Weinbrecht and Mason, 2008), here, three different values for the backscatter coefficient that cover this range are tested; namely $C_\mathrm{B} = 0.6, 1.0$ and 1.4.

For l_B, it is recalled that the aim of the SB model is to model backscatter from the unresolved to the smallest resolved scales, and so l_B should be on the order of the local LES filter width, which is typically assumed to be on the order of the local grid-scale. However, in finite-difference LES codes that use anisotropic and/or variable grid spacing, ambiguity exists over the effective local grid resolution. The geometric mean of the three local grid spacings in each

dimension is one often-used measure (Deardorff, 1970b); the local backscatter length-scale might thus be defined as

$$l_{\mathrm{B}} = \left(\Delta x_i \Delta y_j \Delta z_k\right)^{1/3}. \tag{56}$$

Alternatively, Mason and Brown (1999) suggest that the effective grid resolution is governed by the coarsest of the three local grid spacings; thus, the local backscatter length-scale might instead be defined as

$$l_{\mathrm{B}} = \max\{\Delta x_i, \Delta y_j, \Delta z_k\}. \tag{57}$$

Here, both these definitions for l_{B} shall be tested. On the employed LES model grid, Eq. (56) gives $l_{\mathrm{B}} = 0.45$ m below roof-level (where $\Delta z = 0.3$ m) and Eq. (57) gives $l_{\mathrm{B}} = 1$ m everywhere. It is worth noting that neither of these backscatter length-scales could have been employed with the WM08 model; Eq. (56) because l_{B} varies spatially depending on the local grid spacing but must remain fixed with the WM08 model, and Eq. (57) because l_{B} with the WM08 would be fixed at the value of $\left(\Delta x_i \Delta y_j \Delta z_k\right)^{1/3}$ in the flow interior rather than the value of $\max\{\Delta x_i, \Delta y_j, \Delta z_k\}$.

For $\mathrm{VMF_B}$, two values are tested; namely $\mathrm{VMF_B} = 0.05$ and $\mathrm{VMF_B} = 0.5$. $\mathrm{VMF_B} = 0.05$ is close to the minimum permissible value, which corresponds to $\alpha = 0$ in Eq. (47) and implies that $\hat{\phi}_x$ and $\hat{\phi}_z$ are fully independent; this essentially retrieves the older version of the SB model used for the neutral ABL case (Chapter 4). $\mathrm{VMF_B} = 0.5$ has been chosen partly on empirical grounds; a recent field measurement study of flow within a full-scale isolated street canyon (Blackman *et al.*, 2015) reports a magnitude of $\overline{u'w'}$ of around 1/2 the magnitude of $\sigma_u \sigma_w$ within the roof-level shear layer. By adopting this value, it is thus assumed that the measured ratio is representative of the ratio associated with backscatter in the shear layer, which is not confirmed. However, it is also noted that $\mathrm{VMF_B} = 0.5$ is close to the maximum

permissible value (when $\alpha = 1$) of $\mathrm{VMF_B} \approx 0.6$; the two tested values for $\mathrm{VMF_B}$ should therefore also allow an assessment of the full extent to which the modification to control grid-scale VMF can affect results.

In summary, 12 different configurations of the new SB model are tested, corresponding to the 12 possible combinations of: three tested values of $\mathrm{C_B}$; two tested definitions of l_B; and two tested values of $\mathrm{VMF_B}$. This is summarised in Table 5.1.

Table 5.1 – SB model configurations
Configurations of new SB model for the street canyon flow simulations. C_B is the backscatter coefficient, l_B the backscatter length-scale, and $\mathrm{VMF_B}$ the backscatter VMF factor. SMAG refers to a run that uses the Smagorinsky SGS model alone (i.e. no backscatter).

Run Name	C_B	l_B	$\mathrm{VMF_B}$
SMAG	N/A	N/A	N/A
C1L1V1	0.6	Eq. (56) used	0.05
C1L1V2	0.6	Eq. (56) used	0.5
C1L2V1	0.6	Eq. (57) used	0.05
C1L2V2	0.6	Eq. (57) used	0.5
C2L1V1	1.0	Eq. (56) used	0.05
C2L1V2	1.0	Eq. (56) used	0.5
C2L2V1	1.0	Eq. (57) used	0.05
C2L2V2	1.0	Eq. (57) used	0.5
C3L1V1	1.4	Eq. (56) used	0.05
C3L1V2	1.4	Eq. (56) used	0.5
C3L2V1	1.4	Eq. (57) used	0.05
C3L2V2	1.4	Eq. (57) used	0.5

Other SB model parameters/settings are as follows. $T_\mathrm{B} = 2\Delta t$ is again taken as the backscatter time-scale. For simplicity, the choice is made to impose fully isotropic backscatter acceleration fields for these simulations, i.e. it is assumed that $\overline{a_1^2} = \overline{a_2^2} = \overline{a_3^2}$ everywhere, however it is noted that the imposition of anisotropic backscatter is also possible with the SB model. A point-wise scaling factor (Eq. (43)) is used to scale the backscatter acceleration fields (as opposed to a vertical scaling factor, as used in the neutral ABL simulations), since the street canyon flow-field is not horizontally homogeneous. As done in previous studies

(Mason and Thomson, 1992, Weinbrecht and Mason, 2008), the instantaneous dissipation field is filtered prior to the calculation of the expected point-wise energy backscatter rates (Eq. (55)) to ensure that variations in ϵ occur on a similar spatial scale to variations in the backscatter accelerations. To do this, the same filter used on the $\hat{\phi}$ fields during the backscatter generation procedure is applied to the ϵ field, with the key difference that the filter weights are normalised (i.e. scaled to sum to unity at each grid point) to ensure that ϵ is conserved. Figure 5.2 demonstrates the effect of filtering the dissipation field in this way (where $l_{\mathrm{B}} = \left(\Delta x_i \Delta y_j \Delta z_k\right)^{1/3}$ has been used).

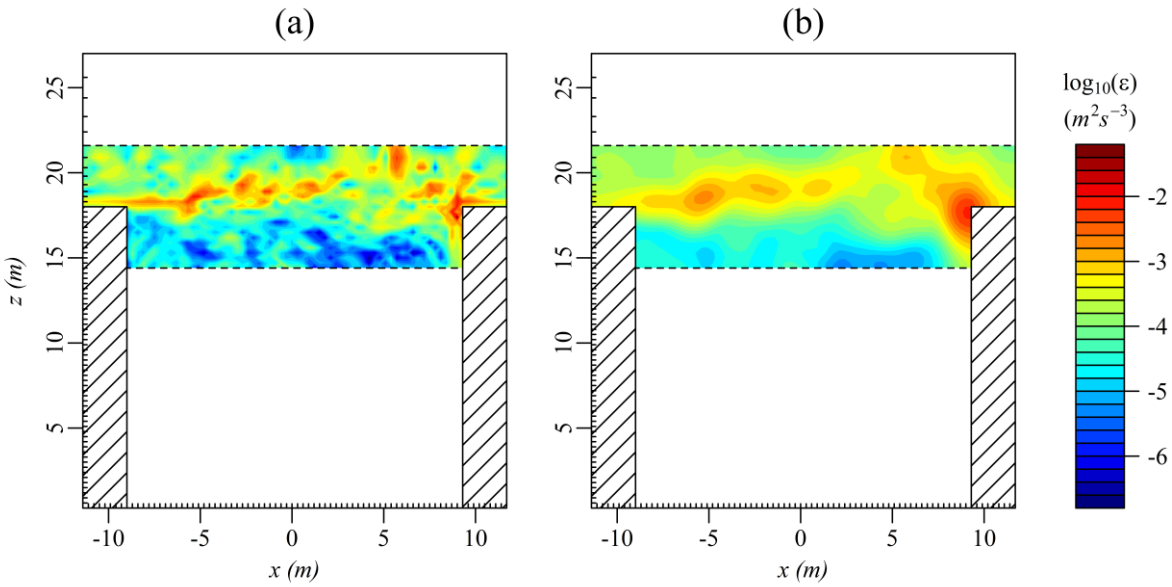

Figure 5.2 – Unfiltered and filtered dissipation field
An x-z contour slice of the logarithm (base 10) of an instantaneous dissipation field, for the area of the domain in which backscatter accelerations are added, with: (a) no filter applied; (b) the SB model filter applied, as done before calculating the point-wise energy backscatter rates.

Finally, for computational efficiency, it is sensible to apply the backscatter accelerations only in regions of the flow where ϵ (and therefore the energy backscatter rate) is large. Here, attention shall be confined to the region of the energetic roof-level shear layer only. It is noted that the backscatter model might also be applied in the regions adjacent to each solid surface,

where ϵ will again become large. Although this would certainly affect the local dynamics (and any scalar dispersion), these effects are unlikely to have any significant impact on the primary eddy intensity, which is largely controlled by the flux of momentum through the roof-level shear layer. Horizontal- and time-averaged vertical profiles of the dissipation rate, $\langle\overline{\epsilon}\rangle$, (not shown, although Figure 5.2(a) provides an instantaneous example) reveal a peak at roof-level that drops off sharply in both directions such that $\langle\overline{\epsilon}\rangle$ is at least a factor of 10 smaller by $z = 0.8H$ and $z = 1.2H$. The backscatter accelerations are thus only applied within this bounded region, i.e. within $0.8 \leq z/H \leq 1.2$ (as indicated by the shaded region in the schematic Figure 5.1).

5.2.3 Wind-tunnel data

The WT experiment used for validation was conducted by Brown *et al.* (2000). It consisted of six adjacent 'street canyons' formed by seven solid rectangular blocks, each measuring $0.15\ \text{m} \times 0.15\ \text{m} \times 3.8\ \text{m}$, placed with their long face perpendicular to the oncoming wind direction x and spaced equally apart to form street canyons of unity aspect ratio. Among other variables, the mean streamwise and vertical velocity components (u and w) and the turbulence intensity were calculated from high-temporal-resolution measurements taken at various heights along five separate transects within the furthest-downwind (i.e. the sixth) street canyon. Each transect was at a different along-width location, namely at $x/W = -0.4, -0.12, 0, 0.25$ and 0.4, where $x = 0$ corresponds to the street canyon centre-point (see Figure 5.1). Measurements from the last street canyon best represent the equilibrium flow regime observed in the limit of an infinite number of canyons, which is arguably of greater interest than the flow regime observed in more isolated street canyons, since large urban areas often consist of many such repeating 'blocks' of buildings. A photo of the WT set-up is shown in Figure 5.3.

Figure 5.3 – Wind-tunnel photo
Photo of the wind-tunnel set-up for the experiment by Brown *et al.* (2000). Photo provided directly by A. R. Brown.

5.3 Results and discussion

5.3.1 Primary eddy intensity

Figures 5.4 and 5.5 show normalised profiles of mean vertical velocity, $\overline{w}/\hat{u}$, and mean streamwise velocity, $\bar{u}/\hat{u}$, respectively, for the simulations in Table 5.1 and the WT experiment, at each of the five across-canyon measurement locations. Here, $\hat{u}$ is the average of $\bar{u}$ between $z/H = 1.0 - 1.5$ over all five locations for any given simulation.

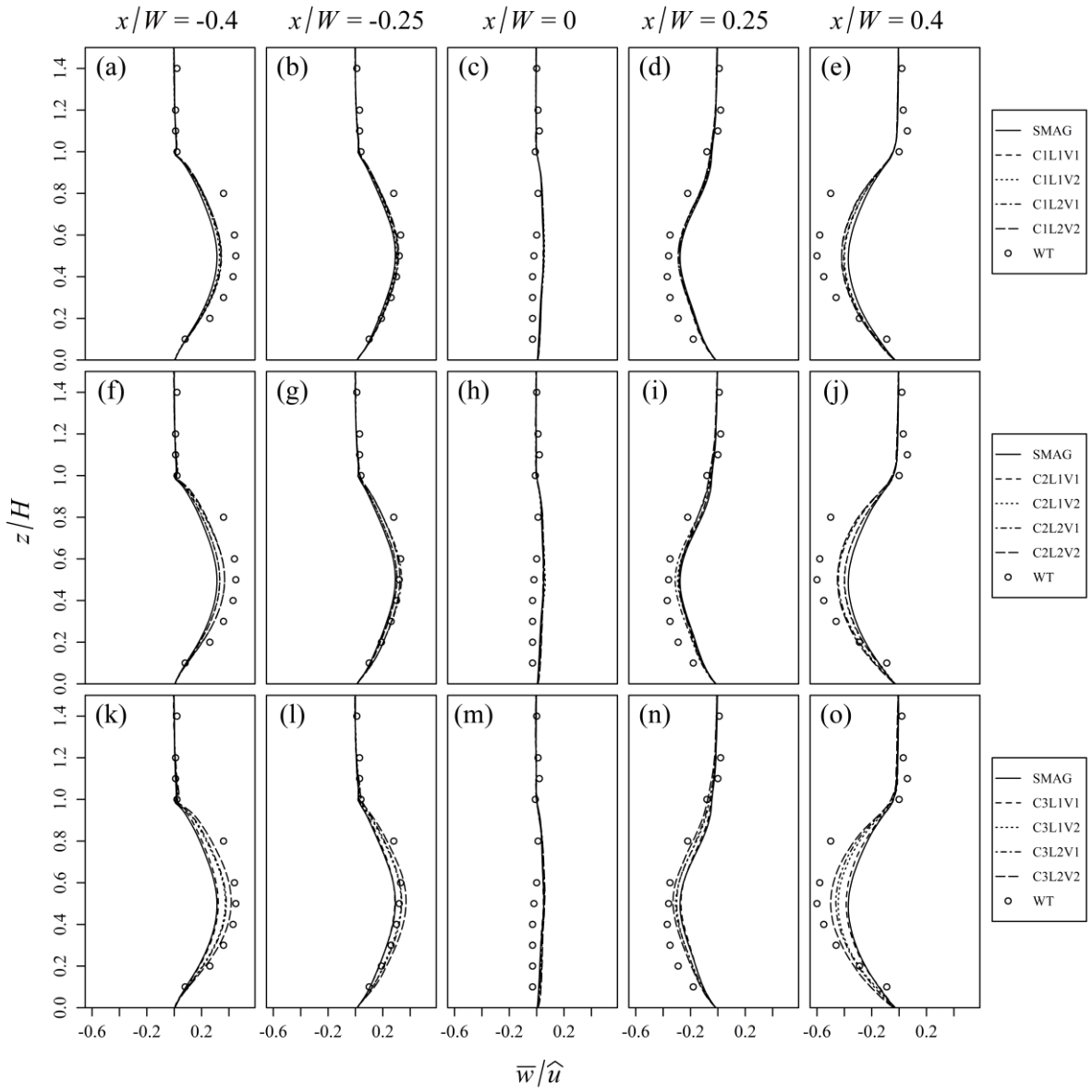

Figure 5.4 – Vertical velocity profiles

Normalised profiles of mean vertical velocity, $\overline{w}/\widehat{u}$, at locations (from left to right) $x/H = -0.4, -0.25, 0, 0.25, 0.4$, respectively. Circles show wind-tunnel data and curves show LES results: solid black lines – Smagorinsky model only; short-dashed lines – smaller l_B and VMF_B values; dotted lines – smaller l_B value, larger VMF_B value; dot-dash lines – larger l_B value, smaller VMF_B value; long-dashed lines – larger l_B and VMF_B values. Top row (panels (a)-(e)) – $C_B = 0.6$; middle row (panels (f)-(j)) – $C_B = 1.0$; bottom row (panels (k)-(o)) – $C_B = 1.4$.

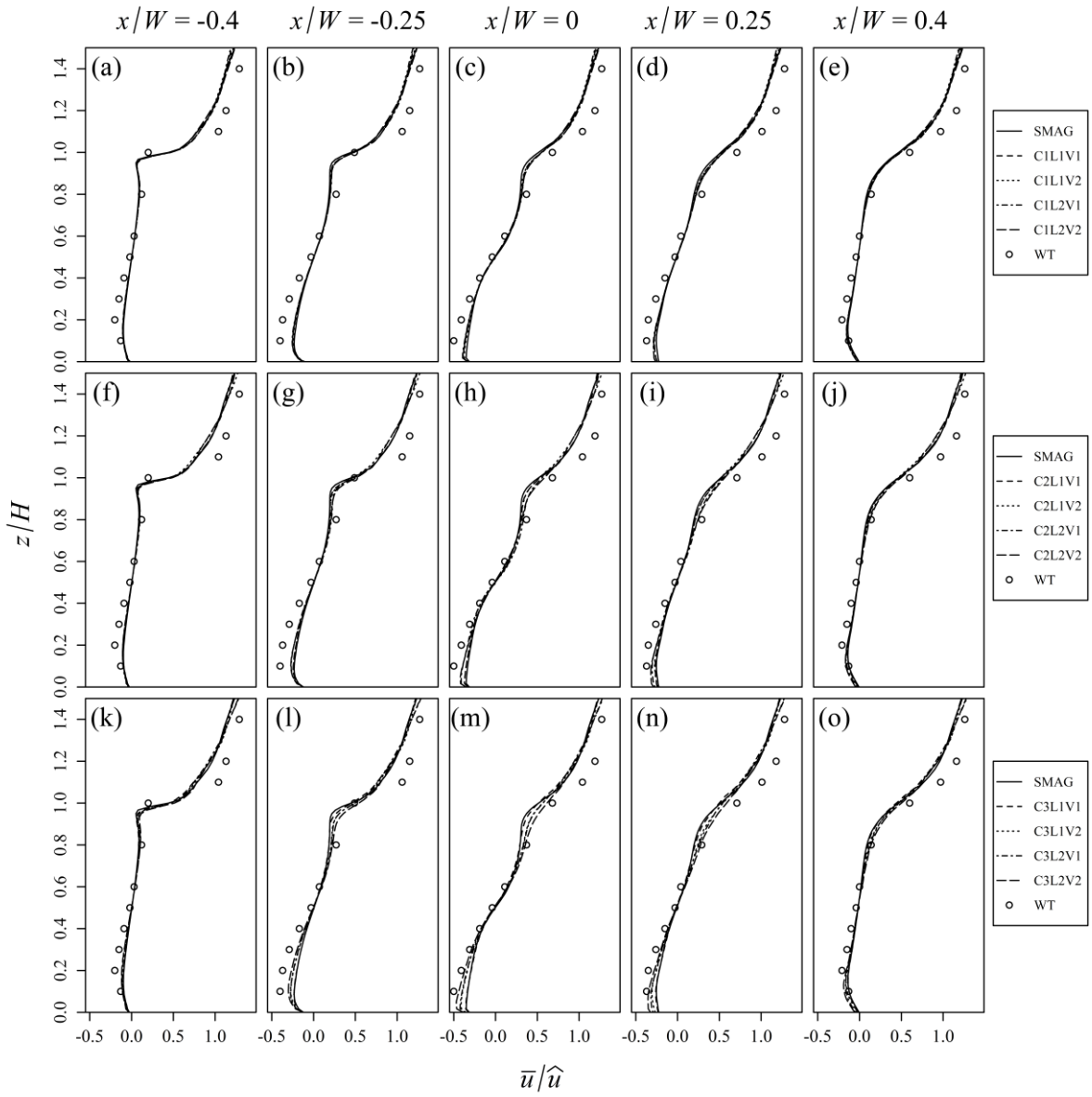

Figure 5.5 – Streamwise velocity profiles
As Figure 5.4 but for normalised profiles of mean streamwise velocity, $\bar{u}/\hat{u}$.

An initial inspection suggests that the SB model acts to intensify the primary eddy compared with the Smagorinsky model in all simulations performed, bringing it closer towards that observed in the WT experiment, but that the effectiveness of the SB model is rather sensitive to the chosen model parameters. Quantification of the PE intensity, from the WT data and each simulation, is attempted to aid inter-comparison. Since the time-averaged spanwise velocity component is zero everywhere, the mean vorticity field is a 2-D scalar field given by

$\omega = \partial_z \bar{u} - \partial_x \bar{w}$. Taking $\bar{u} = \bar{u}(x/W, z/H)$ and $\bar{w} = \bar{w}(x/W, z/H)$, the following non-dimensional value is used as a metric for the PE intensity, ω_{PE}:

$$\omega_{\mathrm{PE}} = \frac{1}{\hat{u}}\left(\left[\frac{\bar{u}(0{,}0.8) - \bar{u}(0{,}0.1)}{0.7}\right] - \left[\frac{\bar{w}(0.4{,}0.5) - \bar{w}(-0.4{,}0.5)}{0.8}\right]\right). \tag{58}$$

Note that the change in $\bar{u}$ is evaluated over a distance of $\Delta z/H = 0.7$, whereas the change in $\bar{w}$ is evaluated over a distance of $\Delta x/W = 0.8$, since no WT measurements were taken at $z/H = 0.9$ but were at $z/H = 0.8$. It should be noted that this metric only provides a general indication of the PE intensity; in particular, it is not possible to infer whether certain regions of the street canyon flow are better simulated (with reference to the WT experiment) than others – for this, the five spatially distinct vertical profiles should be analysed. The ω_{PE} values for each simulation are given in Table 5.2, both in absolute terms and as a percentage of the WT ω_{PE} value. The results confirm that the SB model helps to intensify the PE from that simulated with the Smagorinsky model alone; ω_{PE} is around 30% under-predicted with the Smagorinsky model alone, whereas the inclusion of backscatter can help reduce this discrepancy to as low as 10%, depending on the SB model configuration (discussed later).

Table 5.2 – Primary eddy intensities
Primary eddy intensity, ω_{PE}, for the WT experiment and each LES run.

Case	ω_{PE}	% of WT ω_{PE}
WT	2.56	100
SMAG	1.75	69
C1L1V1	1.90	74
C1L1V2	1.85	72
C1L2V1	1.94	76
C1L2V2	1.92	75
C2L1V1	1.85	72
C2L1V2	1.85	72
C2L2V1	2.05	80
C2L2V2	2.04	80
C3L1V1	1.78	70
C3L1V2	2.06	81
C3L2V1	2.10	82
C3L2V2	2.28	89

Figure 5.5 also shows that a discrepancy between the WT and LES velocity profiles above roof-level ($1 < z/H \leq 1.5$) is largely unaltered by the choice of SGS model (i.e. by the presence or not of backscatter). The WT profile shows a steeper gradient nearer $z/H = 1$, indicating a larger amount of mixing in the WT free-stream flow than in the LES flow that brings higher-momentum air down towards roof-level. This is believed to be largely attributable to the inclusion of only one explicitly modelled street canyon within the LES domain (due to available computational resources) whereas the WT experiment had five street canyons upstream of the test canyon; this limits the size of the largest eddies that can form within the LES free-stream flow compared with in the WT experiment. Of course, additional simulations utilising larger computation resources would be required to confirm this. Although the domain size may also explain part of the remaining discrepancy between the WT and LES velocity profiles within the street canyon when backscatter is modelled, results from a LES study with 12 explicitly modelled street canyons (Liu and Wong, 2014) suggest that the under-predicted PE intensity cannot be remedied by an increase in domain size alone, reemphasising the importance of the SGS model in this regard.

The fairly wide range of ω_{PE} values in Table 5.2 indicates that the effectiveness of the SB model is rather sensitive to the chosen model configuration. To help isolate the effect of each varied SB model parameter (C_{B}, l_{B} and $\mathrm{VMF}_{\mathrm{B}}$) on the PE intensity, ω_{PE} is plotted against each parameter in turn, with one series of points per set of fixed values for the other two parameters. The resulting multi-series plots are shown in Figure 5.6(a)-(c), and discussed in turn below.

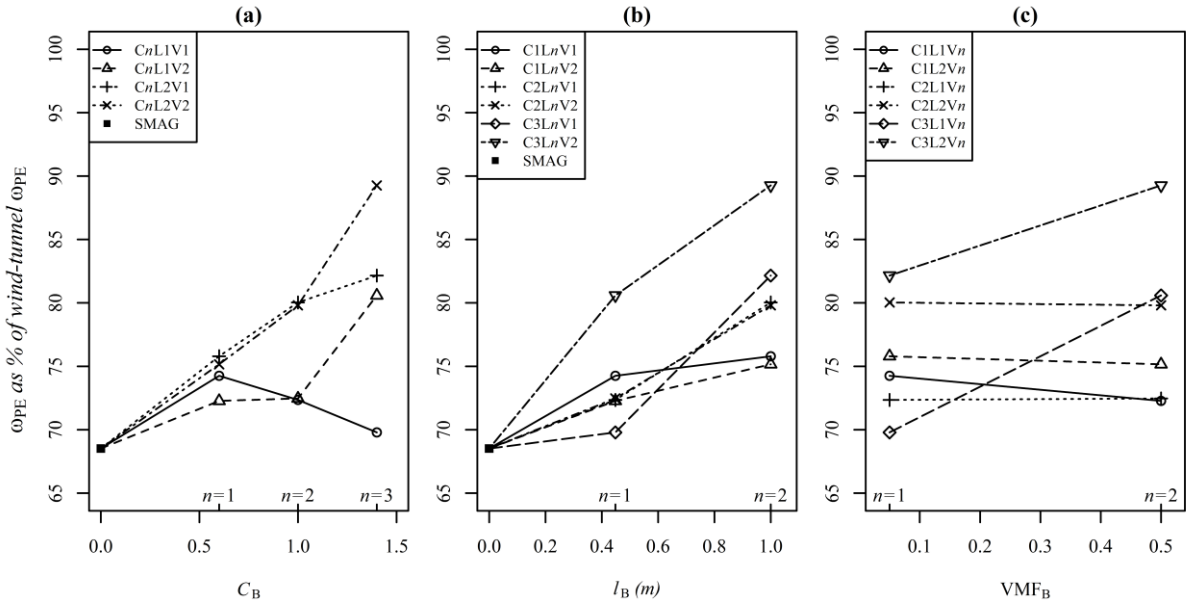

Figure 5.6 – Primary eddy intensities
Multi-series line plots of ω_{PE} (as a % of ω_{PE} from the WT experiment) versus (a) C_B, (b) l_B, (c) VMF_B. Each series shows a set of runs for which the main parameter varies whilst the other two parameters are held fixed. The value of n on the lower axis should be inserted into the relevant legend entry to give the corresponding run name (see Table 5.1). Note that in panel (b), $l_B = 0.45$ m refers to the value of $(\Delta x_i \Delta y_j \Delta z_k)^{1/3}$ within the street canyon (i.e. below roof level), where $\Delta x, \Delta y, \Delta z = 0.3$ m, 1 m, 0.3 m are fixed.

Backscatter coefficient, C_B

Figure 5.6(a) shows that increasing C_B leads to a monotonic increase in ω_{PE} in three of the four series. An intensification of the PE with increasing C_B might be expected on the presumption that increasing the magnitude of the backscatter fluctuations would act to increase the turbulence flux across the roof-level shear layer, thus increasing the transfer of higher (lower) momentum air into (out of) the street canyon. However, for the simulations using the smaller values of l_B and VMF_B (series CnL1V1), it is seen that although ω_{PE} initially increases with C_B (compare the value at $C_B = 0$, i.e. no backscatter, with the value at $C_B = 0.6$), it then decreases with further increases in C_B (although it still remains larger than the value without any backscatter). A proposed explanation for this non-monotonic relationship is as follows. It is noted that, since the backscatter accelerations have zero mean

and (with the current isotropic set-up) random direction, they should act to dissipate any *isolated* coherent structure that they are applied to in favour of randomness (isotropy). Thus, if applied to the *shear-layer alone*, the backscatter accelerations should act to smooth out the sharp velocity gradients within the shear layer, bringing higher momentum flow into the street canyon, which in turn should drive an intensification of the PE. However, if applied to the *primary eddy alone*, the backscatter accelerations should act to reduce the intensity of the primary eddy. (In both cases, an increase in C_{B} would enhance the dissipation of that isolated structure.) Thus, whether the PE intensity increases due to the indirect effect of the backscatter accelerations on the shear layer or decreases due to the direct dissipative effect of the backscatter accelerations depends on the relative influence of each of these processes. Thus, with the smaller values of l_{B} and $\mathrm{VMF}_{\mathrm{B}}$ selected, it seems that while smaller backscatter accelerations (smaller C_{B}) favour an intensification of the PE due to the larger (indirect) influence of vertical mixing of the shear layer over the (direct) influence of PE dissipation, larger backscatter accelerations (larger C_{B}) favour a reduction in PE intensity for the opposite reason. Of course, these arguments should be treated with caution without a more rigorous analysis.

Backscatter length-scale, l_B

Figure 5.6(b) shows that increasing l_{B} leads to an intensification of the PE in all the simulations performed. This is rather more expected; larger (in length) backscatter fluctuations will allow higher-momentum flow further above roof-level to be mixed down through the shear layer and into the street canyon, which in turn will drive an intensification of the PE. As the larger tested length-scale gives a simulated PE intensity that is closer to the wind-tunnel PE intensity in all cases tested, it might be inferred that Eq. (57) is a better measure of the effective grid resolution than Eq. (56) (at least for the LES grid used here),

although this inference should be treated with caution as it is not possible to know what fraction of the PE intensity deficit is attributable to other factors, such as the limited domain size, without further testing.

***Backscatter vertical momentum flux factor,* $\mathbf{VMF_B}$**

Figure 5.6(c) suggests that the effect of increasing $\mathrm{VMF_B}$ on the PE intensity depends on the magnitude of the backscatter accelerations: when $C_\mathrm{B} = 0.6$, increasing $\mathrm{VMF_B}$ leads to a slight decrease in PE intensity (although it remains larger than the value without any backscatter); when $C_\mathrm{B} = 1$, increasing $\mathrm{VMF_B}$ does not significantly change the PE intensity; and when $C_\mathrm{B} = 1.4$, increasing $\mathrm{VMF_B}$ leads to a significant intensification of the PE – by around 10% of the wind-tunnel PE intensity in one case (series C3L1V*n*). Following the same reasoning as previously discussed, this suggests that with smaller-magnitude backscatter accelerations, an increase in grid-scale VMF enhances the influence of direct dissipation of the PE over the indirect influence of extra vertical mixing across the shear layer, and thus the PE intensity is reduced, whereas with larger-magnitude backscatter accelerations, the opposite is true and so the PE intensifies (with a transition from one regime to the other for intermediate magnitudes).

5.3.2 Turbulent kinetic energy

Figure 5.7 shows normalised profiles of mean RS-TKE, $\bar{E}/\hat{E}$ for short, for the simulations in Table 5.1 and the WT experiment, at each of the five across-canyon measurement locations, where $\hat{E}$ is the average RS-TKE between $z/H = 1.0 - 1.5$ over all five locations. $\hat{E}$ is equal to $0.022\ \mathrm{m^2\ s^2}$ for the Smagorinsky model run. Given that the backscatter fluctuations constitute a direct energy source in the roof-level region, values of $\hat{E}$ for the SB model runs are all larger, and range from 0.027 to 0.043 $\mathrm{m^2\ s^2}$ depending on the selected model

parameters. It is first noted that the SB model helps to reduce the spurious RS-TKE bump seen in the centre of the street canyon, at $(x/W, z/H) \approx (0,0.5)$, when the Smagorinsky model alone is used. This bump implies that, with the Smagorinsky model, the PE centre has a tendency to move around too much over time. As the backscatter accelerations act to intensify the PE, the additional angular momentum imparted helps stabilise it, thus helping to correct this tendency. Other than this, for $C_{\mathrm{B}} \leq 1$, there are no striking differences between the RS-TKE profiles observed with the SB model and with the Smagorinsky model alone, apart from at roof-level where there is a slightly better prediction close to the downwind building wall of the street canyon for $C_{\mathrm{B}} = 0.6$, and a slightly worse (over) prediction close to the upwind building wall for $C_{\mathrm{B}} = 1$. For $C_{\mathrm{B}} = 1.4$, however, over-predictions at roof-level, and within the upper half of the street canyon close the downwind building wall, become more noticeable. Interestingly, comparing the profiles of the two simulations with the larger l_{B} value (i.e. C3L2V1 and C3L2V2), it is seen that the *larger* $\mathrm{VMF_B}$ value actually helps *reduce* the over-prediction of RS-TKE; this is particularly noticeable close to the downwind building wall, in panels (m)-(o) of the plot. This provides further encouragement that providing the ability of the SB model to increase grid-scale VMF is well-founded. Even with this reduction, however, RS-TKE is still slightly over-predicted in these regions, which suggests that the backscattered energy is perhaps too large with a backscatter coefficient of $C_{\mathrm{B}} = 1.4$. An alternative explanation for this apparent over-prediction might be an issue of scaling in combination with an under-prediction of the large-scale free-stream eddies in the LES domain. It is noted that with larger RS-TKE values in the region just above roof-level (used for scaling the values within the street canyon) as a result of larger free-stream eddies, the normalised RS-TKE profiles below roof-level would be shifted towards smaller values.

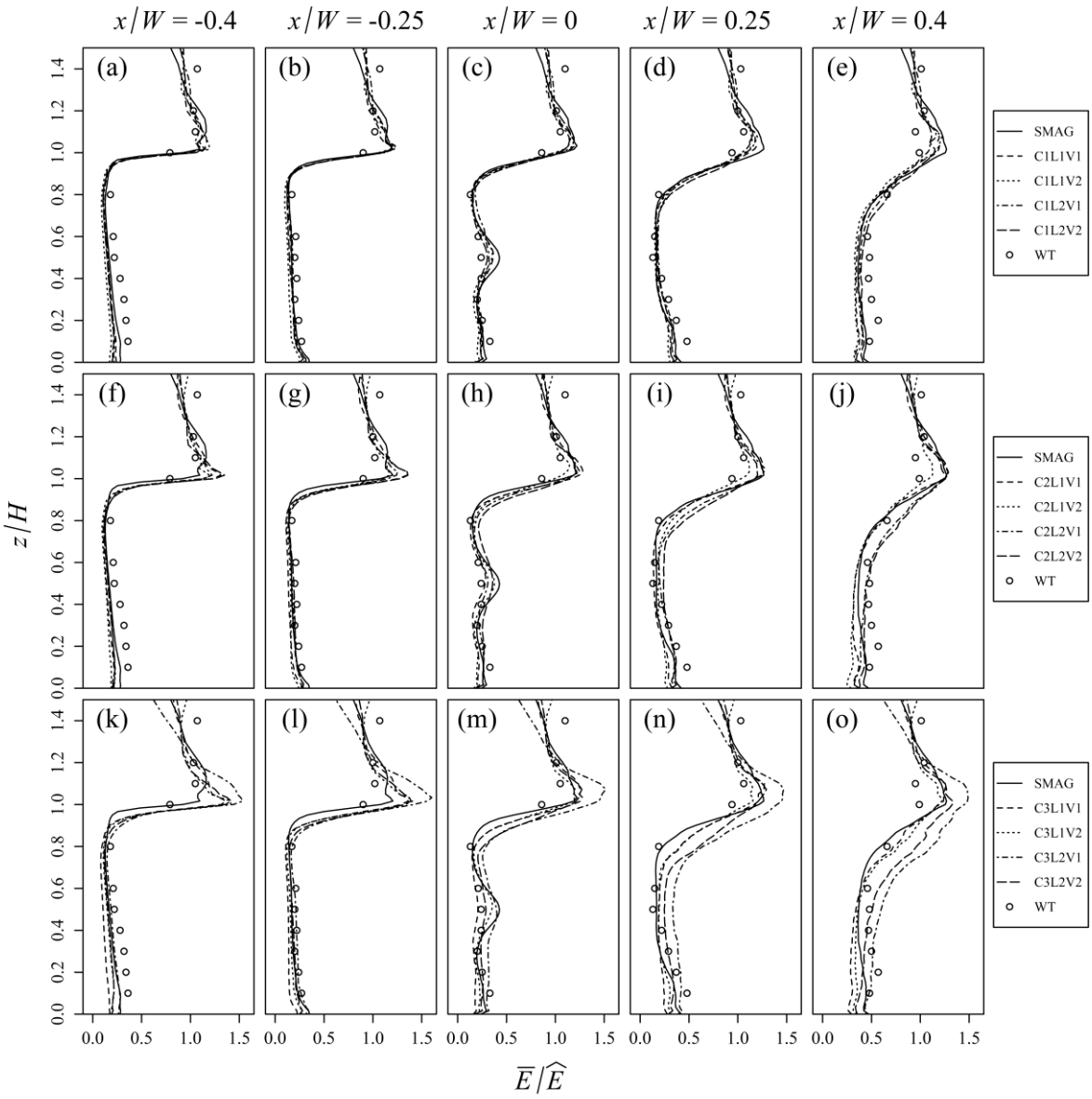

Figure 5.7 – RS-TKE profiles
As Figure 5.4 but for normalised profiles of resolved-scale turbulent kinetic energy, $\overline{\boldsymbol{E}}/\widehat{\boldsymbol{E}}$.

5.3.3 Shear layer entrainment: air exchange rate

The effect of the SB model on the rate of entrainment through the shear layer can be assessed by looking at the air exchange rate (ACH). First proposed by Liu *et al.* (2005), the ACH describes the rate of air exchange between the street canyon and the free-stream flow above (units $\mathrm{m^3 s^{-1}}$). It thus also provides an assessment of the air ventilation efficiency, with a

higher ACH implying a better ventilated street canyon. Continuity dictates that, for an incompressible gas, the volume of air entrained into the street canyon (ACH_+) should be equal to the volume removed from it (ACH_-) over any given period. ACH may thus be calculated at a particular time by integrating only the positive vertical velocities over the street canyon opening, i.e.:

$$\mathrm{ACH}_+(\mathrm{t}) = \int_{z=H} w_+(t)\ \mathrm{d}A_{\mathrm{SC}}, \tag{59}$$

where $w(t)$ is the instantaneous vertical velocity component at time t, the + subscript implies that only positive values are considered, and A_{SC} is the area at the top of the street canyon, at $z = H$. Similarly, ACH_- can be calculated by integrating only the negative vertical velocities over the street canyon opening.

The resulting time-averaged values of normalised ACH_+ for each simulation are given in Table 5.3 (recall that LES statistics are calculated from the last 15 minutes of each simulation, when the flow is quasi-steady). ACH has been normalised by V/T, where $V = HWL_y$ is the volume of the street canyon within the LES domain, and $T = H/U_{\mathrm{ref}}$ is a time-scale associated with the free-stream flow. Here, $U_{\mathrm{ref}} = \bar{u}(z = 1.5H)$ is used to aid comparison of the results obtained here with Liu *et al.* (2005), who used a LES domain height of $1.5H$. However, this scaling is somewhat arbitrary, and since ACH has not yet (to the author's knowledge) been measured by WT experiment, the key concern here is the relative differences in ACH among the simulations rather than their exact values. The rate of entrainment through the shear layer is confirmed to be higher with the SB model than with the SMAG model, which is consistent with the observed intensification of the primary eddy within the street canyon (§5.3.1). The Smagorinsky model value of $\overline{\mathrm{ACH}_+}/(V/T) = 0.035$ is slightly below the value of 0.05 reported by Liu *et al.* (2005), who used a dynamic SGS

model. With the SB model, normalised ACH is as much as doubled (0.07 for case C3L2V2), demonstrating that the additional grid-scale fluctuations imparted by the SB model within the roof-level shear layer can cause a significant increase in the amount of air entrained into the street canyon from the free-stream flow. The ACH values also illustrate why an increase in the backscatter vertical momentum flux can be effective; comparing runs C3L2V1 and C3L2V2, the time-averaged entrainment rate has been increased by a further 20% (from 0.058 to 0.07), providing the additional momentum needed to drive a further intensification of the primary eddy. A larger backscatter length-scale also increases the rate of entrainment; e.g., comparing runs C3L1V1 and C3L2V1, normalised ACH is increased by a further 16% (from 0.05 to 0.058).

Table 5.3 – ACH values
Normalised air exchange rate ($\overline{\mathbf{ACH_+}}$) for the WT experiment and each LES run. (Note that $\overline{\mathbf{ACH_+}}$ was not calculated in the WT experiment).

Case	$\overline{\mathbf{ACH_+}}/(\mathbf{V/T})$
WT	N/A
SMAG	0.035
C1L1V1	0.043
C1L1V2	0.044
C1L2V1	0.047
C1L2V2	0.046
C2L1V1	0.046
C2L1V2	0.044
C2L2V1	0.051
C2L2V2	0.054
C3L1V1	0.050
C3L1V2	0.056
C3L2V1	0.058
C3L2V2	0.070

5.4 Summary and conclusions

The results in this chapter demonstrate that the new SB model can help improve the accuracy of LES of street canyon flow compared with the Smagorinsky model. This result supports the theory that there is significant backscatter of energy within the roof-level shear layer that,

when under-resolved by the LES grid, should be directly accounted for by the SGS model. The specific case tested was LES of skimming flow within a street canyon of unity aspect ratio, in which the approaching wind is perpendicular to the street axis and neutrally stratified. It was observed that the SB model could lead to an increase in the intensity of the primary eddy within the street canyon, compared with a simulation using the (purely dissipative) Smagorinsky model, thus bringing it significantly closer towards the PE intensity observed in a corresponding (reduced-scale) WT experiment. The simulated value of ω_{PE}, a metric for the PE intensity based on the 2-D vorticity field, was increased from approximately 70% of wind-tunnel ω_{PE} value (with the Smagorinsky model) to as much as 90% (with the SB model). The additional grid-scale backscatter encourages more turbulent mixing across the roof-level shear layer that separates the PE from the free-stream flow above, thus entraining more momentum into the canyon, which in turn drives an intensification of the PE. An increased rate of entrainment with the inclusion of backscatter was confirmed via calculation of the air exchange rate across the roof-level opening of the street canyon.

The simulations in this chapter also serve to demonstrate the merit in the ability to control the backscatter vertical moment flux with the new SB model. It was seen that by increasing the backscatter VMF alone, the simulated PE intensity metric ω_{PE} could be increased by as much as 10% of the WT ω_{PE} value. Furthermore, it was observed that larger grid-scale VMF can help reduce any over-prediction of RS-TKE within the upper half of the street canyon.

The sensitivity of the simulated PE intensity to other SB model configuration changes was also investigated; namely, the backscatter coefficient, C_{B}, and backscatter length-scale, l_{B}, were both varied. For the simulations performed here, larger backscatter fluctuations typically (but not always) led to a larger PE intensity, whereas wider backscatter fluctuations always led to a larger PE intensity. A measure for the local LES filter width (used to set l_{B}) based on

the maximum of the local grid spacings in each dimension thus gave a better simulated PE intensity than a measure based on the geometric mean of these local grid spacings. It is also worth noting that the ability to test different values of l_{B}, as done here, would not have been possible with the previous (MT92 and WM08) SB models. The largest tested value of C_{B} (namely, 1.4) gave the best match to the wind-tunnel PE intensity, but an over-prediction of RS-TKE in the upper half of the street canyon suggests that this value might be slightly too large. Alternatively, this over-prediction might be a scaling issue resulting from an under-prediction in RS-TKE in the region above roof-level, due to a lack of large-scale eddies in the free-steam flow as a result of the limited size of the modelling domain.

Limitations of the work performed in this chapter include the fact that the tested case, of a neutrally stratified flow within a 2-D street canyon of unity aspect ratio, represents only one (albeit important) example of the many street canyon configurations (and atmospheric conditions) found in the real urban canopy layer. In future work, other configurations for which field or laboratory data are available for validation should be tested to confirm whether similar improvements in simulation accuracy are observed. With the availability of more computational resources, the effect of the limited LES domain extent employed here should also be determined, although it is again noted that results from previous studies with larger LES domains (Liu and Wong, 2014) suggest that the under-predicted PE intensity cannot be remedied by an increase in domain size alone, reemphasising the importance of the SGS model in this regard.

To sum up, simulation accuracy of street canyon flow has been shown to improve with the SB model, satisfying the third research objective (§2.4). The next step is to test whether the SB model can also help improve the prediction of scalar (pollutant) transport and removal from the street canyon in a LES-driven dispersion modelling study. If confirmed, this result will

have positive implications for operational urban dispersion models that employ parameters derived from LES output.

6. STREET CANYON DISPERSION

6.1 Introduction

This chapter addresses research objective #4, as stated at the end of §2.4 and repeated below for convenience:

> **Objective #4**: Examine the effect of the SB model on improving LES of the dispersion of a passive tracer inside the street canyon, again comparing simulation accuracy against that obtained with the Smagorinsky model and using a wind-tunnel dataset for validation.

Since the findings in Chapter 5 indicate that the accuracy of the simulated street canyon flow dynamics can be improved with the use of the SB model, it is worth testing whether similar improvements are also observed for the subsequent dispersion of a passive tracer released into the simulated flow-field. Furthermore, the effects of an SB model on tracer dispersion have, to the author's knowledge, never been studied previously, and so a knowledge gap exists. Positive results would also be potentially beneficial to operational urban dispersion models that use parameters derived from LES output (Salizzoni *et al.*, 2009).

This chapter is structured as follows. As in the previous two chapters, a methodology section (§6.2) is used to give the configuration settings for both the LES model (§6.2.1) and the new SB model (§6.2.2). Results are then presented and discussed (§6.3); two separate validation studies are first performed to assess the simulation accuracy achieved with the Smagorinsky and SB models separately. In the first, the exchange velocity of the escaping pollutant across the street canyon opening is calculated for each LES and compared with a WT dataset (§6.3.1). In the second, the LES wall concentration profiles are calculated and compared with a separate WT dataset (§6.3.2). Other dispersion and transport properties from the two LES

are then compared against each other; namely, the mean 2-D fields of pollutant concentration (§6.3.3) and turbulent pollutant flux (§6.3.4), and the pollutant exchange rate (§6.3.5 – defined therein). Finally, the results are summarised and conclusions drawn (§6.4).

It is noted that some of the materials in this section appear in the following paper, which is currently under review for publication in a peer-reviewed journal: O'Neill *et al.* (under review).

6.2 Methodology

6.2.1 LES model configuration

The same computational domain, model grid, boundary conditions, initial profiles, Smagorinsky coefficient and time-step are used for the street canyon dispersion simulations as were used for the street canyon flow simulations (see §5.2.1 and Figure 5.1). In addition, vehicular emissions from two lanes of traffic are modelled using two slightly elevated line sources running parallel with the y axis along the full length of the street. The first source is located at $(x/W, z/H) = (-1/6, 1/20)$ and the second source at $(x/W, z/H) = (1/6, 1/20)$. A passive (neutrally buoyant and chemically inert) scalar is emitted from each source at a constant rate of $Q_s = 500\ \mu g\ m^{-1}\ s^{-1}$. Each source is given a small finite extent (5 grid points) in x and z, with a 2-D Gaussian concentration profile, in order to minimise issues associated with near-source numerical dispersion. A Schmidt number of $Sc = 0.7$ is used. A periodic boundary condition for the scalar field is employed only in the y direction. An open boundary condition is used in the x direction (above the street canyon), which corresponds to the situation in which escaped pollutants leave the downwind boundary and do not re-enter the upwind boundary, at which a zero background concentration is specified. This is achieved through the specification of the following conditions at these boundaries:

$$C = 0 \qquad \text{at } x = -\frac{L_x}{2}, \tag{60}$$

$$\frac{\partial C}{\partial t} + u\frac{\partial C}{\partial x} = 0 \qquad \text{at } x = \frac{L_x}{2}. \tag{61}$$

The above information is schematised in Figure 6.1.

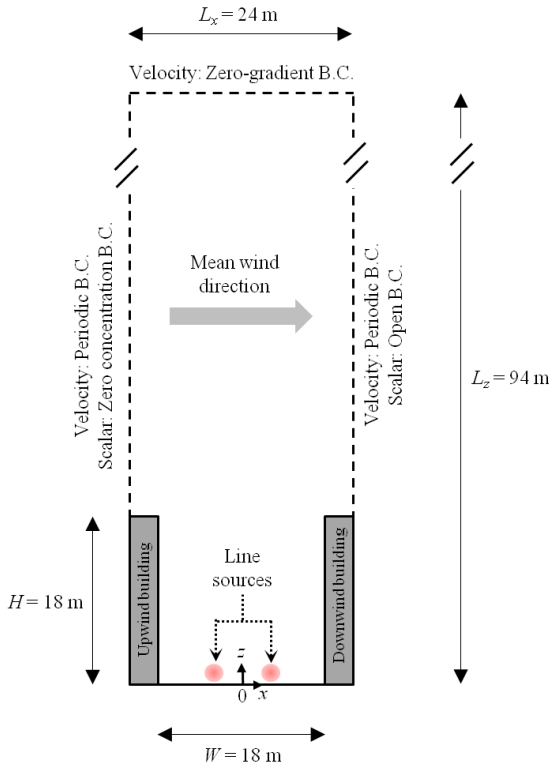

Figure 6.1 – LES domain (with sources)
Schematic of the LES computational domain, including sources, for the street canyon dispersion simulations (B.C. = boundary condition).

The model is initially run without any source emissions, for a period of 60 min (around 20 primary-eddy turnover times). This gives the flow dynamics sufficient time to reach a quasi-steady state. Source emissions are then started and the model is run for a further 120 min; this gives sufficient time for a quasi-steady state of pollutant transport to be established. Data from the final 30 min of the simulation period are then processed for averaging to obtain the results presented in Chapter 6, with the exception of §6.3.1, which uses data obtained after further turning off the source and recording subsequent time-series of decaying concentration (further details given therein).

Other than the addition of the sources, the only difference between the street canyon dispersion simulation and the street canyon flow (i.e. dynamics-only) simulations (Chapter 5) is that for the dispersion simulations, a constant pressure gradient force is applied (above roof-level only) throughout the simulation period in order to approximately conserve the total momentum in the system. This is done because the longer simulation time here means that total momentum loss is no longer insignificant, which makes it difficult to attain a quasi-steady state without the imposition of the constant PGF.

6.2.2 SB model configuration

For the street canyon dispersion simulations, the new SB model is (like with the street canyon flow simulations) compared against the Smagorinsky SGS model only, using different WT datasets for validation. The SB model parameters are selected based on the street canyon flow analysis (Chapter 5); the set of parameters that resulted in the best agreement between the (dynamical) LES output and the WT data are carried forward to analyse the subsequent effects on tracer dispersion. Namely, these parameters are: a backscatter coefficient of $C_{\mathrm{B}} = 1.4$; a local backscatter length-scale of $l_{\mathrm{B}} = \max\{\Delta x_i, \Delta y_j, \Delta z_k\}$; and a backscatter vertical momentum flux factor of $\mathrm{VMF}_{\mathrm{B}} = 0.5$. This is summarised in Table 6.1. All other SB model parameters/settings are as described in §5.2.2.

Table 6.1 – SB model configuration
Configuration of new SB model for the street canyon dispersion simulations. Symbols are as in Table 5.1.

Run Name	C_{B}	l_{B}	$\mathrm{VMF}_{\mathrm{B}}$
SMAG	N/A	N/A	N/A
SB	1.4	Eq. (57) used	0.5

6.3 Results and discussion

6.3.1 Model validation: Pollutant exchange velocity

The LES output is first validated against the WT dataset of Salizzoni *et al.* (2009), in which the pollutant exchange velocity, v_e, (alternatively the transfer or ventilation velocity) was estimated via 'wash-out' curves, i.e. measured time-series of decaying pollutant concentrations after an emissions shutdown. This value is of particular interest to urban dispersion modellers, as it forms the key parameter that describes the pollutant mass transfer between the urban canopy and the flow above it in many simplified operational models. Long bars with a square cross-section of 6×6 cm were spaced equally apart inside the WT test section to form repeating street canyons of unit aspect ratio perpendicular to a fully-developed neutral boundary flow. Within the measurement canyon, passive tracer was released at a constant rate from a central ground-level line source, until a quasi-steady state of pollutant transport was reached. The source was then turned off and concentration time-series recorded (using flame ionisation detection) at two separate points within the street canyon: at point *a*, located at the centre of the street canyon; and at point *b*, located left of centre at a radial distance of $H/3$. The experiment was repeated 50 times. An analytical model was then fitted to the ensemble-averaged wash-out curves[1] to obtain the value for v_e.

Decaying concentrations are recorded for each LES in an equivalent manner; however, rather than repeating each simulation 50 times, the concentration at a particular x, z location and time t is calculated by averaging in the homogeneous spanwise (y) direction (a total of 40 values). It is noted that although the LES source configuration is different to that of the WT (two line sources compared with one, and slightly elevated rather than at ground-level), this

[1] The relative volumes of the central core and outer region were chosen *a priori*; here a comparison is made with the $\beta = 0.85$ case.

has negligible effect on the calculated exchange velocity. As the WT wash-out curves in Salizzoni *et al.* (2009) were reported in absolute time, the data must be normalised to allow for comparison with the simulations performed here. The street canyon height H provides the reference length-scale, and the far-field free-stream velocity U_∞ provides the reference velocity-scale ($U_\infty = 6.75\ \mathrm{m\ s^{-1}}$ and $2.6\ \mathrm{m\ s^{-1}}$ in the WT and LES, respectively); the reference time-scale T is thus given by H/U_∞.

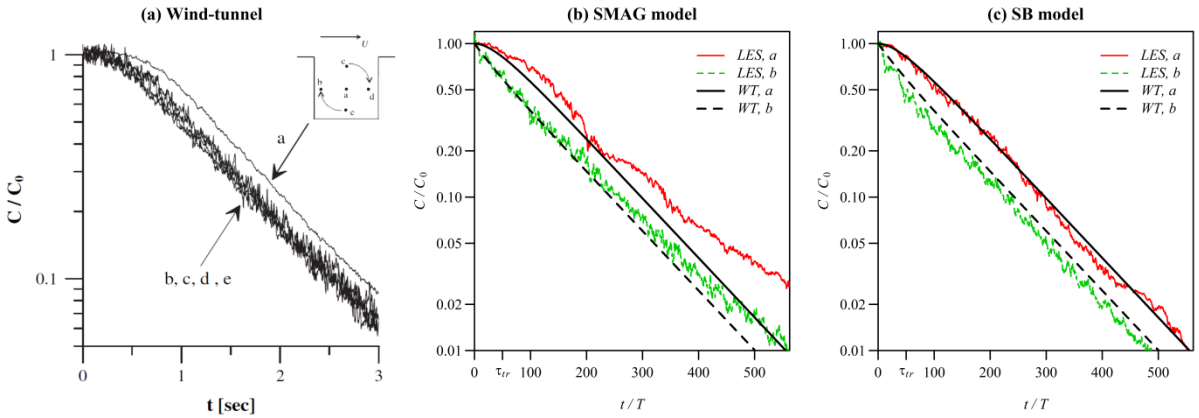

Figure 6.2 – Wash-out curves
Pollutant wash-out curves from: (a) the WT experiment (Fig. 8 from Salizzoni *et al.* (2009)); (b) LES with the SMAG model; (c) LES with the SB model. LES curves shown for points *a* (centre) and *b* (outer vortex) only, along with the analytical model that fits the WT data at each of these points in normalised time (black lines). τ_{tr} on lower axis denotes the transition period time-scale (see text for details).

Figure 6.2 shows the pollutant wash-out curves from: (a) the WT experiment (reproduced from Salizzoni *et al.* (2009)); (b) LES with the SMAG model; and (c) LES with the SB model. Concentrations are plotted on a logarithmic axis and are normalised by the initial (quasi-steady) concentration at that given location, C_0, and in (b) and (c) time is normalised by T as discussed above. Each LES plot also shows the fitted analytical two-box model from the WT experiment. The two boxes represent the primary eddy core and the recirculating ring outside of the core, respectively. The analytical model assumes that the turbulent transport of pollutants from the primary eddy core towards the outer regions is slow; this argument has been supported by their measured data (i.e. the concentration in the core represented by point

a, denoted by C_a, is much higher than that in the ring, say, C_b) as quoted here in Figure 6.2(a). The LES wash-out curves are generally consistent with the WT fitted analytical model, in that there is an initial transient during which C_b drops fast *and* that C_a falls much less rapidly than C_b (shown by the *WT* lines in Figure 6.2(b) and (c)). As elucidated by Salizzoni *et al.* (2009), this is due to the fact that the time-scale associated with the turbulent transport of pollutants from the primary eddy core towards the outer ring is slower than the time-scale associated with the removal of pollutants from the top of the primary eddy through the turbulent roof-level shear layer. A careful examination of the analytical model yields that the time-scale of this transient period, denoted by τ_{tr}, is approximately $50T$; when $t \gg \tau_{tr}$, the analytical model gives a solution asymptotically approaching a pure exponential decaying, which appears as a straight line on the log-linear coordinates, illustrated in Figure 6.2(b) and (c). In addition, the slope of the line can be used to estimate the asymptotic "retention time" of pollutants (DePaul and Sheih, 1985). Because the WT data were inevitably contaminated by the experimental settings during an early part of the transition period (see the discussions in Salizzoni *et al.* (2009)), the fast decrease of C_b is not seen in the WT data (Figure 6.2(a)). However, the asymptotic exponential decaying data matched the analytical model very well and can be used to assess the current LES results. Figure 6.2(b) shows that the asymptotic slopes of LES-derived C_a and C_b based on the SMAG model are too gentle (i.e. C_a and C_b decay slower) compared with the WT data fitted curves. However, Figure 6.2(c) demonstrates that the gradients of the wash-out curves for C_a and C_b with the SB model are in better agreement with the WT data fitted curves; in other words, the pollutant retention time within the street canyon is better represented, thus indicating a more accurate exchange velocity, v_{e}. Table 6.2 gives the values of v_{e} for each SGS model, obtained in the same way as in Salizzoni *et al.* (2009) (i.e. by fitting the analytical model to the measured time-series using the least-

squares method, over the time period shown in Figure 6.2(b) and (c)). The exchange velocity with the SB model is 14% higher than with the SMAG model. With the inclusion of backscatter, the increased turbulence at roof-level causes a more efficient ventilation of air, and thus removal of pollutants, from the street canyon.

Table 6.2 – Exchange velocities
LES-predicted exchange velocity, v_e, using the SMAG or the SB SGS model, and the % difference.

	v_e (m s^{-1})	% difference
SMAG	0.0239	
SB	0.0273	+14%

6.3.2 Model validation: Wall concentration profiles

The LES output is also validated against the WT data of Meroney *et al.* (1996) and Pavageau (1996). In both studies, mean concentration profiles were measured on the upwind and downwind building walls (see Figure 6.1 for wall naming conventions) of a modelled street canyon of unit aspect ratio. The working section of the WT was 1 m high, 1.5 m wide and 4 m long, preceded by a section in which spires and roughness elements were used to generate a fully-developed neutral boundary layer. 28 identical wooden blocks with square cross-section, each measuring 6 cm × 6 cm × 1.4 m, were placed on the WT floor with the long face perpendicular to the direction of flow, and spaced 6 cm apart to create 27 repeating street canyons. Measurements were taken in the 20th downwind canyon, in which the flow was effectively periodic. Passive and neutrally buoyant tracer gas was emitted at a constant rate from a ground-level line source, placed along the central axis of the street canyon, in order to simulate vehicular exhaust emissions.

Figure 6.3(a) and (b) shows normalised mean concentrations, $\overline{C}/\overline{C}_{\mathrm{norm}}$, on the upwind and downwind building walls of the street canyon, as measured in the WT studies described above and as predicted by the LES with the SMAG or SB model. For a given dataset, $\overline{C}_{\mathrm{norm}}$ is taken

to be the mid-height ($z = 0.5H$) mean concentration on (a) the upwind building wall or (b) the downwind building wall. In previous studies, e.g. Baik and Kim (2002), Walton and Cheng (2002) and Cheng *et al.* (2008), the mean concentration on the upwind building wall at the ground-level has been used for normalisation. However, concentrations on the lower half of the upwind building wall have been shown to be sensitive to the source configuration, namely the distance of the line source from the wall (Kastner-Klein and Plate, 1999, Cai *et al.*, 2008) and the source height (Cai *et al.*, 2008). At the same time, these studies also show that the concentrations in the upper half of the upwind building wall and on the downwind building wall are fairly insensitive to the source configuration, and therefore provide better reference values for normalisation when differences between the LES and WT source setup exist, as they do here. Two separate locations for $\overline{C}_{\mathrm{norm}}$ are used in order to check for consistency.

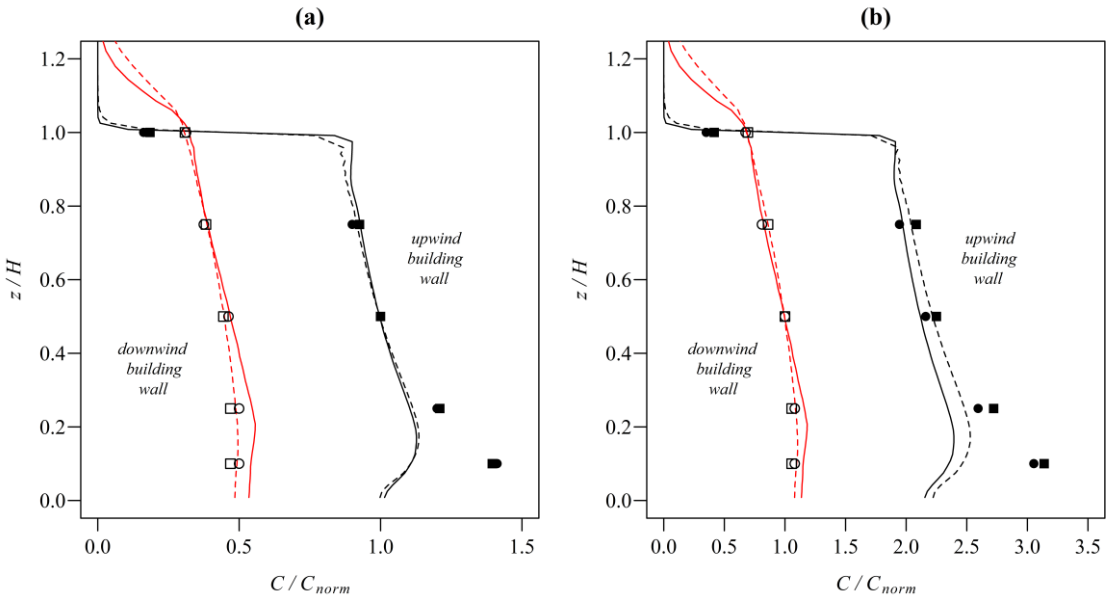

Figure 6.3 – Wall concentration profiles

Normalised mean concentrations, $\overline{C}/\overline{C}_{\mathrm{norm}}$, on the upwind and downwind building walls of the street canyon. $\overline{C}_{\mathrm{norm}}$ is taken as $\overline{C}$ at $z = 0.5H$ on (a) the upwind building wall (b) the downwind building wall. Filled symbols show WT data on the upwind building wall: ■ Pavageau (1996); ● Meroney *et al.* (1996). Unfilled symbols show corresponding data on the downwind building wall. Lines show LES data: —— SMAG model; – – SB model.

The sensitivity of concentrations at the lower part of the upwind building wall on the source configuration is evident in Figure 6.3; the slightly elevated source height in the LES set-up compared with the ground-level line source in the WT experiment gives noticeably lower concentrations in this region. This behaviour is consistent with previously published results (Cai *et al.*, 2008). Along the other regions of the upwind and downwind building walls, both LES profiles exhibit a generally good agreement with the WT data. However, with either normalisation, the slope of the concentration profile with the SB model seems to exhibit a slight improvement over the slope with the SMAG model. This is particularly noticeable on the downwind building wall, where the concentration gradient is (correctly) reduced with the SB model. With the inclusion of backscatter, the additional turbulence at roof-level acts to mix the recirculating pollutant with the cleaner entrained air from outside the canyon more readily; the relatively slower mixing process that then occurs down the downwind building wall as the air re-entrains pollutant from the street canyon core only leads to a small further increase in concentration.

6.3.3 Mean 2-D fields: Pollutant concentration

The mean concentration within the street canyon during the last 30 min of (quasi-steady) simulation, $\overline{C}_{\mathrm{can}}$, for each SGS model is given in Table 6.3. $\overline{C}_{\mathrm{can}}$ is calculated as the average of C in time and space for the volume below $z = H$. $\overline{C}_{\mathrm{can}}$ is approximately 15% lower with the SB model than with the SMAG model. This is a direct result of the increased exchange velocity with the inclusion of backscatter (§6.3.1) as a result of greater mixing across the roof-level shear layer. Figure 6.4(a) and (b) shows the mean 2-D (i.e. time and spanwise average only) concentration fields, $\overline{C}$, for the SMAG and SB model, respectively, normalised by $\overline{C}_{\mathrm{can}}$ in each case. In both cases, one observes the main features typical of the mean 2-D concentration field as reported in previous wind-tunnel (e.g. Pavageau and Schatzmann

(1999), Simoëns and Wallace (2008), Salizzoni *et al.* (2009)) and modelling (e.g., Baik and Kim (1999), Liu and Barth (2002)) studies; the released pollutant is largely transported around the street canyon by the primary recirculation, with some of the pollutant escaping from the top of the canyon through the roof-level shear layer, resulting in larger concentrations near the upwind building than near the downwind building. However, there are also observable differences between the 2-D fields for each SGS model, most notably the vertical extent of the sharp concentration gradient between the street canyon and the free-stream flow, and the near-source magnitudes. The latter is a consequence of using the canyon-averaged concentration for normalisation; since more pollutant escapes from the top of the street canyon with the SB model, the concentration in the lower part of the canyon relative to the upper part increases. The wider vertical extent of the concentration contours at roof-level with the SB model is due to the increased turbulent fluctuations causing a locally faster rate of mixing and thus smoothing out of the concentration gradients there. It is also noted that the small-scale concentration structures close to the ground would likely be modified if the backscatter model was also applied in this region. However, this would not affect the canyon-averaged concentrations.

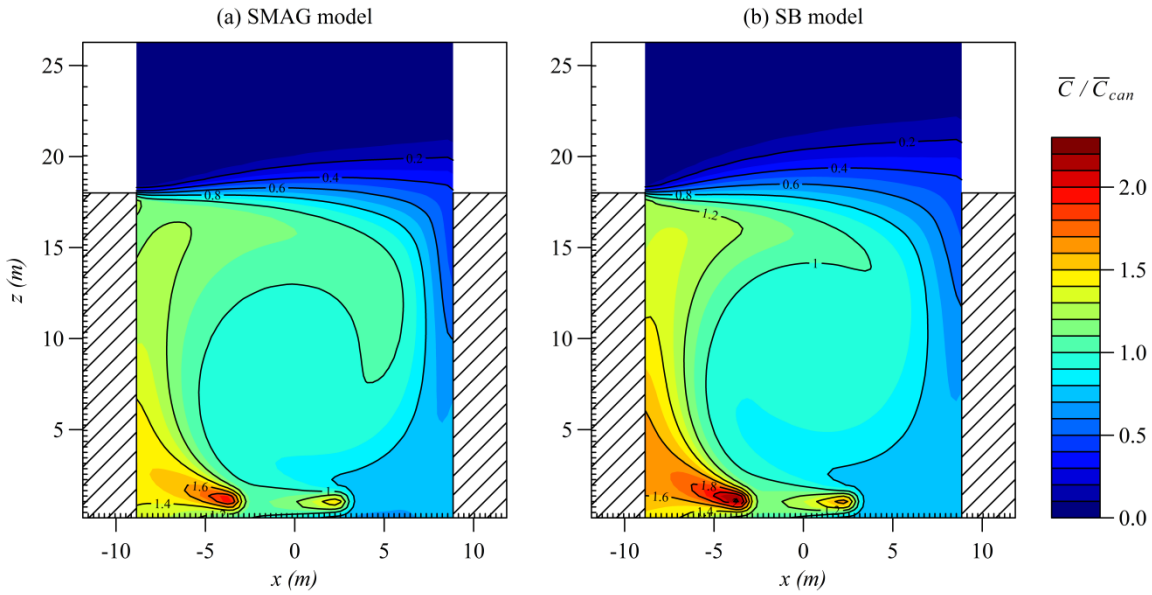

Figure 6.4 – Concentration fields

Normalised mean concentration fields, $\overline{C}/\overline{C}_{\mathrm{can}}$, for (a) the SMAG model, and (b) the SB model.

The mean concentration fields can also be used to look at the relative pollutant distribution within, and above, the street canyon for the given modelling domain. By integrating each 2-D field over the volumes of the domain bounded by $z \leq H$ and $z > H$ separately, one obtains the mean pollutant mass within the street canyon, $\overline{M}_{\mathrm{sc}}$, and the free-stream (background) flow, $\overline{M}_{\mathrm{bg}}$, respectively, i.e.

$$\overline{M}_{\mathrm{sc}} = \int_{z \leq H} \overline{C}\, dV, \qquad \overline{M}_{\mathrm{bg}} = \int_{z > H} \overline{C}\, dV. \tag{62}$$

A measure of the dilution efficiency of a street canyon can then be obtained by comparing the relative pollutant mass in each of these volumes (Liu and Barth, 2002, Liu *et al.*, 2004, Liu *et al.*, 2005). Clearly, the value of $\overline{M}_{\mathrm{bg}}$ depends on the size (specifically, the downwind fetch) of the domain and so is not a useful measure in isolation; however, when the modelling domain is fixed and the SGS model changed, as here, any relative changes become meaningful. Table 6.3 gives the percentage of pollutant retained inside the street canyon with the current

modelling domain for the two simulations performed in this study. It is found that the fraction of pollutant retained inside the canyon with the SB model is slightly reduced from the SMAG model value, again indicating a more efficient ventilation of pollutants from the street canyon. Note that a direct comparison of the current values with those of Liu and Barth (2002) may not be made due to differences in domain size above roof-level.

Table 6.3 – Mean concentrations
Mean concentration within the street canyon, $\overline{C}_{\mathbf{can}}$, and the percentage of pollutant retained inside the street canyon for the current modelling domain, for each SGS model

	$\overline{C}_{\mathbf{can}}$ $(\boldsymbol{\mu g\ m^{-2}})$	$\overline{M}_{\mathbf{can}}/(\overline{M}_{\mathbf{can}}+\overline{M}_{\mathbf{bg}})$ **(%)**
SMAG	2373	95.5
SB	2031	93.0

6.3.4 Mean 2-D fields: Turbulent pollutant flux

Figure 6.5(a) and (b) shows, for the SMAG and SB model respectively, the mean 2-D fields of the vertical pollutant flux by turbulent fluctuations, $\overline{w'C'}$, normalised by the average source flux Q/W, where Q is the total emission rate of the two line sources (1000 μg m^{-1} s^{-1}) and W is the street canyon width (18 m). Also plotted (Figure 6.5(c)) is the streamwise profile of normalised $\overline{w'C'}_{\mathrm{RL}}$ for each SGS model, where the subscript RL indicates 'at roof-level' (i.e. at $z = H$). During a period of quasi-steady pollutant transport, the total pollutant flux out of the street canyon, i.e. $\overline{wC}_{\mathrm{RL}}$ integrated across roof-level, will be equal to Q/W. Here, it is found that the mean value of $\overline{w'C'}_{\mathrm{RL}}/(Q/W)$ across the streamwise profiles is equal to 1.01 for both SGS models. Using a Reynolds decomposition, i.e. taking $w = \overline{w} + w'$ and $C = \overline{C} + C'$, gives $\overline{wC}_{\mathrm{RL}} = \overline{w}\,\overline{C}_{\mathrm{RL}} + \overline{w'C'}_{\mathrm{RL}}$; these results thus indicate that almost all of the total vertical pollutant flux at roof-level is due to fluctuating velocity (i.e. turbulent processes). Conversely, vertical pollutant flux by mean flow ($\overline{w}\,\overline{C}_{\mathrm{RL}}$) is small and negative, i.e. its net effect is actually to transport escaped pollutants back into the canyon. This corroborates

previous findings, e.g. Baik and Kim (2002), Michioka *et al.* (2011), while also serving to highlight why RANS models struggle to accurately predict pollutant removal for skimming flow, as they must rely almost entirely on their turbulence parameterisation scheme.

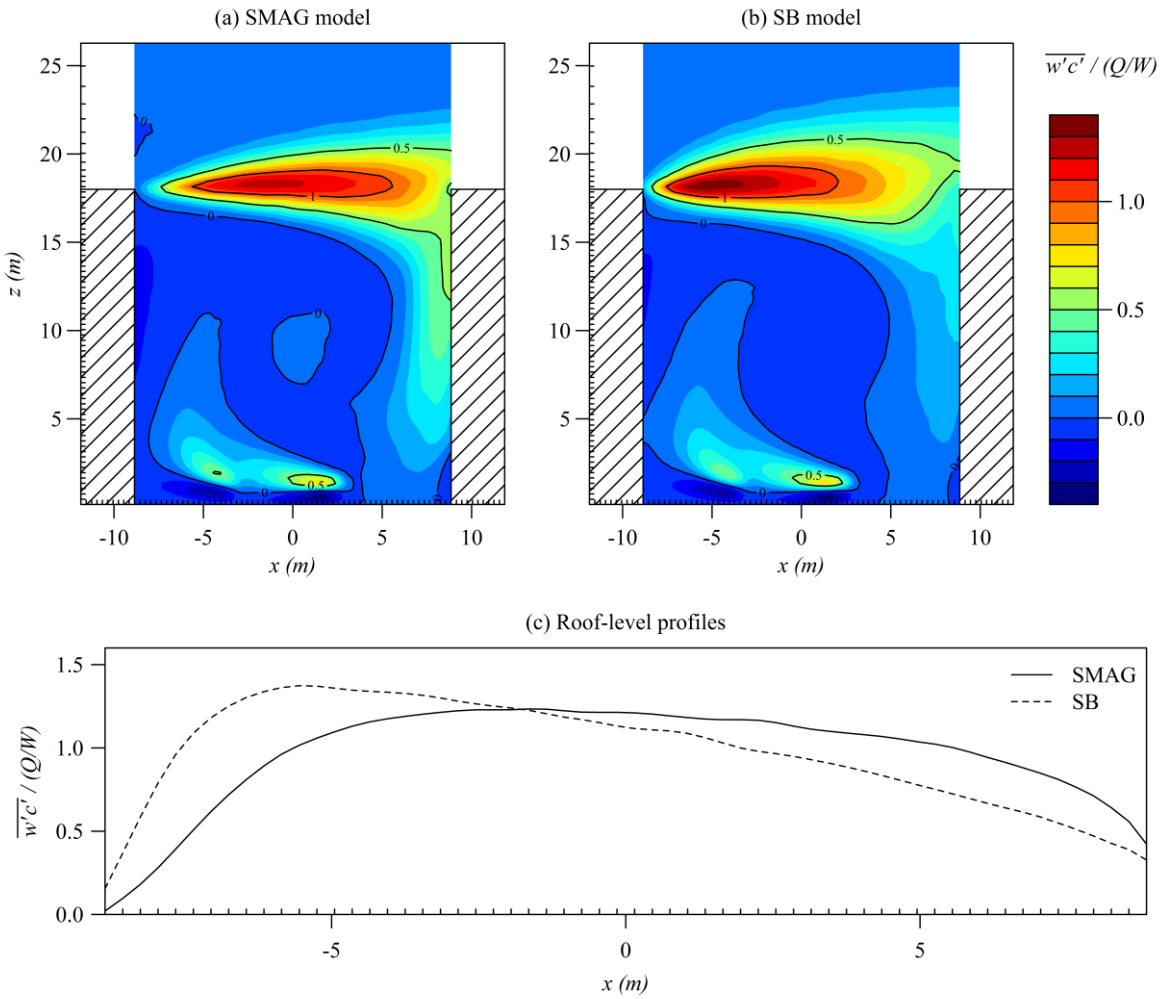

Figure 6.5 – Turbulent pollutant flux fields
Top panels: Normalised mean fields of vertical pollutant flux by fluctuating velocity, $\overline{w'C'}/(Q/W)$, for (a) the SMAG model, and (b) the SB model. Bottom panel (c) shows the streamwise profile of $\overline{w'C'}/(Q/W)$ at roof-level.

The streamwise roof-level profiles also show that with the SB model, a larger proportion of the escaping pollutant is predicted to leave the upwind half of the street canyon and, accordingly, a smaller proportion predicted to leave the downwind half, compared with the SMAG model. Inspection of the mean streamwise profile of dissipation rate ϵ (not shown) indicates that there is no significant difference in the theoretical energy backscatter rate across

roof-level, i.e. the increase in vertical velocity variance at roof-level due to the inclusion of backscatter is fairly constant across the street canyon opening. Thus, the reason for the upwind shift in the pollutant flux profile is simply because pollutant released near ground-level reaches the upwind half of the street canyon opening first; the increased vertical velocity variance causes a larger fraction of pollutant to be mixed out of the canyon at this earlier stage, meaning that a lower fraction is advected towards the downwind half of the canyon by the primary vortex, and so there is less pollutant for the increased vertical velocity variances there to act on.

Substituting C for u to consider vertical flux of horizontal momentum (rather than pollutant), $\overline{w'u'}$, similar behaviour should be expected, since the oncoming wind reaches the upwind half of the street canyon opening first and more momentum can thus be expected to be mixed into the street canyon at this earlier stage with an increase in vertical velocity variance at roof-level. The 2-D fields and roof-level profiles of $\overline{w'u'}$ for each SGS model are plotted in Figure 6.6; indeed, the $\overline{w'u'}_{\mathrm{RL}}$ profile is again shifted towards larger upwind (and corresponding reduced downwind) magnitudes with the SB model.

Finally, it is also noted from Figure 6.5(a) and (b) that the LES with the SB model predicts a thicker shear layer than with the SMAG model. Again, this is a consequence of the increased mixing by the backscatter fluctuations which acts to smooth out the gradients of pollutant flux within the shear layer.

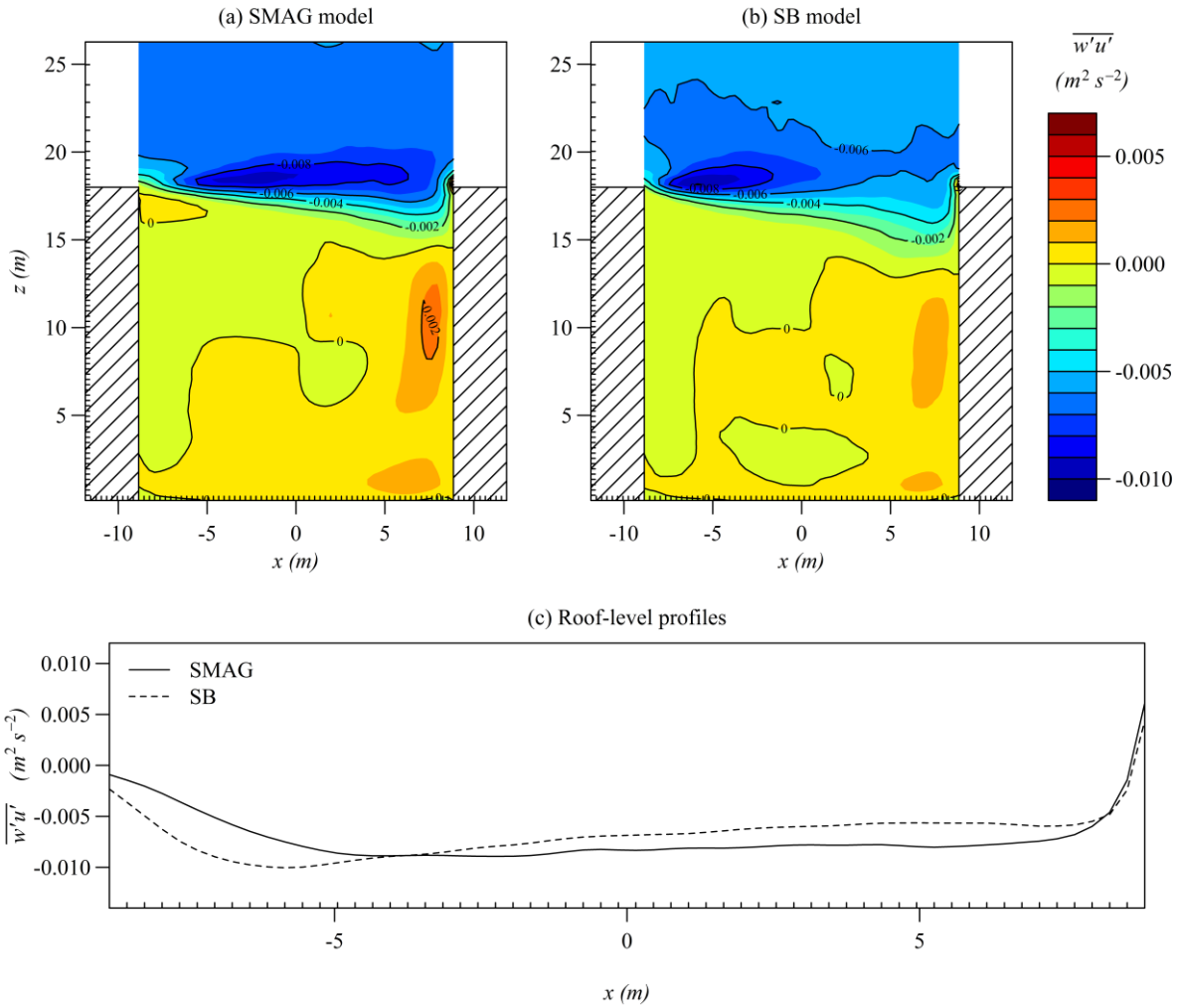

Figure 6.6 – Turbulent momentum flux fields

As Figure 6.5 but for (absolute) vertical momentum flux by fluctuating velocity, $\overline{w'u'}$.

6.3.5 Pollutant exchange rate

The pollutant exchange rate (PCH), first proposed by Liu *et al.* (2005), provides an assessment of the pollutant dilution efficiency of a street canyon. It is typically calculated alongside the air exchange rate (ACH) (Li *et al.*, 2005, Liu *et al.*, 2005, Cheng *et al.*, 2008), which describes the rate of air exchange between the street canyon and the free-stream flow above. It was shown in §5.3.3 that the additional grid-scale fluctuations imparted by the SB model within the roof-level shear layer can cause a significant increase in the air entrainment (removal) rate into (out of) the street canyon, leading to the prediction of a better ventilated street canyon with the SB model than with the SMAG model. For reference, the time-

averaged values of normalised ACH_+ (equal to normalised ACH_- for reasons of mass conservation) for the simulations performed in this chapter are again calculated and given in Table 6.4; the SB model value is approximately 60% larger than the SMAG model value, reconfirming the increased ventilation efficiency predicted with the SB model. In this chapter, the effect of the SB model on pollutant dilution efficiency is further analysed through the calculation of PCH. Like ACH, PCH (units $\mu\mathrm{g\,s^{-1}}$), can be separated into a positive (PCH_+) and negative (PCH_-) part; PCH_+ describes the rate of pollutant removal from the street canyon, and PCH_- describes the rate of pollutant re-entrainment into the street canyon (or total entrainment if the background concentration is non-zero). PCH_+ is calculated as follows:

$$\mathrm{PCH}_+(\mathrm{t}) = \int_{z=H} w_+(t)C(t)\mathrm{d}A_{\mathrm{SC}}, \tag{63}$$

where $C(t)$ is the instantaneous concentration at time t, and the other symbols are as in Eq. (59). Similarly, PCH_- can be calculated by substituting $w_-(t)$ (i.e. negative vertical velocities) for $w_+(t)$ in Eq. (63). Unlike ACH, the difference between positive and negative PCH can be non-zero; in principle, during a period of quasi-steady pollutant transport, the (time-averaged) difference is expected to be equal to the total source emission rate $Q_{\mathrm{tot}} = QL_y$ $[\mu\mathrm{g\,s^{-1}}]$ within the LES domain (otherwise the average concentration within the canyon would not remain steady).

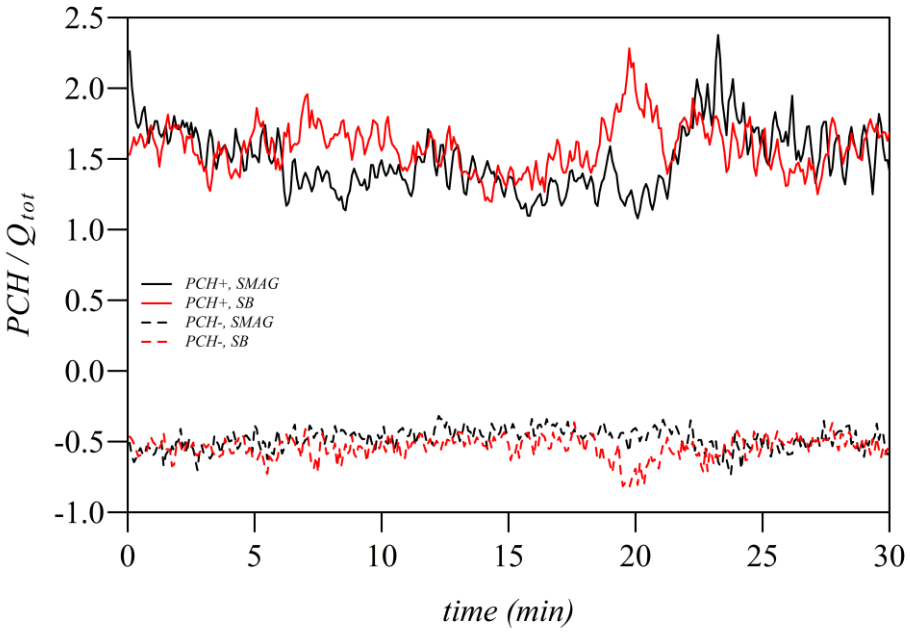

Figure 6.7 – PCH time-series

Time-series of normalised pollutant exchange rate for each SGS model. PCH_+ describes the rate of pollutant removal from the street canyon; PCH_- describes the rate of pollutant entrainment into the street canyon.

Figure 6.7 shows the time series of PCH_+ and PCH_-, normalised by Q_{tot}, during a 30-minute period of quasi-steady pollutant transport, for each SGS model. Time-averaged values are again given in Table 6.4. It is noted that the difference between PCH_+ and PCH_- in each simulation is close to, but not exactly, 1; it would be expected to tend closer to 1 for longer time-averaging period. The results indicate that, unlike ACH, normalised PCH is not significantly affected by the choice of SGS model. Since it is known from the ACH that w_+ increases with the SB model, then in order for PCH to remain largely unchanged between the SB and SMAG model simulations, the roof-level concentrations must decrease by an amount that keeps the integral of their product (w_+C) over A_{SC} approximately the same. This indicates that PCH, in isolation, provides insufficient information to assess for changes in the pollutant dilution efficiency of a street canyon, and should be considered alongside other indicators such as ACH and time-averaged pollutant concentration.

Table 6.4 – ACH and PCH values
Time-averaged air and pollutant exchange rates ($\overline{\mathbf{ACH}}$ and $\overline{\mathbf{PCH}}$) for each SGS model

	$\overline{\mathbf{ACH_+}}/(\mathbf{V/T})$	$\overline{\mathbf{PCH_+}}/\mathbf{Q_{tot}}$	$\overline{\mathbf{PCH_-}}/\mathbf{Q_{tot}}$
SMAG	0.05	1.5	0.5
SB	0.08	1.6	0.6

6.4 Summary and conclusions

In this chapter, two large-eddy simulations of pollutant removal from a street canyon have been compared; one using the widely-adopted Smagorinsky SGS model, and the other using the new SB model. It was shown that simulation accuracy with the SB model was improved, which again highlights the importance in explicitly accounting for grid-scale backscatter within the under-resolved roof-level shear layer when selecting the SGS model.

As in the previous chapter, which looked at the street canyon flow-field dynamics only (Chapter 5), the specific case tested was that of neutrally stratified skimming flow (perpendicular mean wind) over a nominally 2-D street canyon of unit aspect ratio, with two near-ground-level line sources used to represent two lanes of continuous traffic emission; this corresponds to an extreme case in which ventilation, and thus air quality, is poor. The LES output was first validated against WT measurements of decaying pollutant concentrations after an emissions shutdown (Salizzoni *et al.*, 2009). It was found that with the inclusion of backscatter, the asymptotic concentration decay rate was in better agreement with the WT data. The calculated exchange velocity, v_e, between the canyon and the external flow was around 15% faster with the SB model, due to the increased mixing within the roof-level shear layer causing a better ventilated street canyon. This result is potentially important for operational models that use an estimate for v_e to describe the mass transfer between the urban canopy and the overlying flow. A second validation test also indicated that the SB model is

able to better capture the expected mean wall concentration profiles within the street canyon than with the Smagorinsky model.

Other dispersion and transport properties from the two LES were also compared. It was found that the steady-state mean concentration within the street canyon is around 15% lower with the SB model, owing to the higher-predicted ventilation efficiency. It was also shown that almost all of the total vertical pollutant flux at roof-level is due to the fluctuating (rather than mean) velocity component, and that a larger fraction of the escaping pollutant is expected to leave the upwind half of the roof-level opening than the downwind half with the SB model as a result of the increased vertical velocity variance. The shear layer was also seen to be thicker with the SB model due to its tendency to smooth out the sharp velocity, and thus scalar, gradients there. Finally, it was shown that PCH does not significantly change with the inclusion of backscatter, and so, in isolation, provides insufficient information when assessing for changes in a street canyon's dilution efficiency.

It is again noted that the specific case tested here represents only one of the many street canyon configurations (and atmospheric conditions) found in the real urban canopy layer. Thus, in future work, other configurations should be simulated with the aim of generating a more comprehensive database of look-up parameters (e.g. exchange velocities) to be adopted by operational urban dispersion modellers. It is hoped that the work presented here constitutes a first step towards this aim.

7. CONCLUSIONS

A summary of the main findings relating to each research objective, as outlined near the beginning of this thesis (§2.4), is first provided in §7.1. This is followed by an identification of the main limitations of this study and a discussion of future work that might be undertaken to carry the present research forward (§7.2).

7.1 Summary of main findings

In Chapter 3, a new stochastic backscatter model was formulated that allows the local backscatter length-scale, anisotropy and momentum flux associated with the stochastic accelerations to be controlled independently of the model grid. As discussed earlier in the text, the need for such a model existed due to the grid-dependency issues of previous SB models. Neither the model of Mason and Thomson (1992) nor its later implementation by Weinbrecht and Mason (2008) is able to ensure a physically appropriate spatial structure for the backscatter acceleration fields throughout the domain: with the MT92 model, the backscatter length-scale and anisotropy depend on the local grid spacing and aspect ratio; with the WM08 model, the backscatter is unavoidably isotropic with uniform length-scale. The new SB model uses a novel “grid-adaptive” filtering procedure, in which the discrete weights of a 3-D separable Gaussian filter adapt to local changes in grid spacing to ensure that the backscatter length-scale and anisotropy within the resulting acceleration fields are as prescribed. This allows for the backscatter length-scale to be reduced towards surfaces in an appropriate manner, and the backscatter anisotropy to be varied in accordance with the physical anisotropy of the subgrid scales. The new SB model also has wider applicability; it may be used when the LES filter width, and hence the backscatter length-scale, varies spatially with local 3-D grid refinement. In addition, the new SB model is able to control the backscatter vertical momentum flux by prescribing an appropriate degree of correlation

between two of the three filtered fields that are subsequently curled to generate the final acceleration fields. This feature facilitates a better representation of grid-scale vertical momentum flux, which may be known from theory or empirical observations, and which directly affects the local rate of mixing and thus local velocity gradients. The efficacy of the new SB model (in isolation) was confirmed via the generation of a number of example fields on various model grids, in which the backscatter length-scale, anisotropy and/or VMF were checked against their prescribed values.

In Chapter 4, the efficacy of the new SB model when employed as the SGS model within an LES code was tested. The neutral ABL was chosen as the test case, since previous studies had shown that the SB modelling approach is able to achieve significant reduction in excessive velocity shear, as predicted with the widely-used (but purely dissipative) Smagorinsky model, within the surface layer (Mason and Thomson, 1992, Mason and Brown, 1994, Weinbrecht and Mason, 2008). This also allowed the performance of the new SB model to be compared against the performance of the existing (MT92 and WM08) models. Various different grid aspect ratios, ranging from $\Delta_{\mathrm{AR}} = \Delta x/\Delta z = 1$ to 10, were employed to check the grid-independence of the results. The new SB model was found to give a reduction in maximum excessive mean velocity shear (from that obtained with the Smagorinsky model, i.e. without backscatter) of around 80%. Importantly, this reduction was seen to be largely independent of Δ_{AR}. Conversely, with the MT92 model, a significant decline in its ability to reduce excessive velocity shear was observed as the level of near-surface grid anisotropy increased, due to an associated reduction in vertical mixing within the surface layer. With the WM08 model, the reduction in mean velocity shear was similar to that of the new SB model on all grids tested, which, when employing vertical grid refinement only, was expected. However, the improved physical representation of backscatter with the new SB model, as well its wider applicability

to grids with 3-D refinement, still justifies its formulation. The additional CPU time required by the SB model over the Smagorinsky model was shown to be around 50%, which, although not insignificant, was shown to provide a reduction in excessive mean velocity shear that could not be achieved via a simple increase in grid resolution with the Smagorinsky model. This serves to highlight that the inclusion of backscatter in cases of under-resolution of energetic flow is important from a physical perspective.

In Chapter 5, the new SB model was applied – for the first time – to LES of street canyon flow. A 'skimming flow' regime (Oke, 1988) was modelled, under a neutrally stratified atmosphere, in which the approaching wind is perpendicular to the along-street axis of a street canyon of unity aspect ratio. Previous LESs of this type have shown an under-prediction in the intensity of the primary eddy that forms within the street canyon (Liu and Barth, 2002, Cui *et al.*, 2004, Cheng and Liu, 2011a, Liu and Wong, 2014), indicating a lack of momentum transfer across the roof-level shear layer. It was argued that this discrepancy was again due to the omission of backscatter from the SGS model; the highly energetic shear layer that separates the slow-moving primary eddy from the fast-moving external flow is typically under-resolved in most LES set-ups, where backscattered energy is potentially significant. The results showed that the SB model acts to increase the momentum transfer across the shear layer, bringing the simulated PE intensity significantly closer towards that observed in a corresponding wind-tunnel experiment, and thus supporting this theory. A metric for the PE intensity, ω_{PE}, based on the two-dimensional vorticity field, was increased from around 70% of the WT ω_{PE} value (with the Smagorinsky model) to as much as 90% (with the SB model). Calculation of the air exchange rate at roof-level confirmed that the rate of entrainment into the street canyon is increased with the inclusion of backscatter. The results in this chapter also served to highlight the value in controlling the backscatter VMF with the new SB model. It

was seen that by increasing the backscatter VMF alone, the simulated PE intensity metric ω_{PE} could be increased by as much as 10% of the WT ω_{PE} value. The effect of varying the magnitude and length-scale of the imposed backscatter (via the backscatter coefficient and length of the filter used to generate the backscatter acceleration fields, respectively) was also investigated; the best match to the WT dataset was obtained when a backscatter coefficient of $C_{\mathrm{B}} = 1.4$ and a backscatter length-scale equal to the coarsest of the three local grid spacings, i.e. $l_{\mathrm{B}} = \max\{\Delta x_i, \Delta y_j, \Delta z_k\}$, were used.

In Chapter 6, the SB model configuration that gave the best match to WT data in the LES of street canyon flow was carried forward and used to analyse the subsequent dispersion of a passive tracer within the canyon. To the author's knowledge, a LES-driven dispersion study using an SB model had never previously been undertaken. Two near-ground line sources with constant emission rate were used to model vehicular emissions from two lanes of steady traffic. The street canyon configuration tested (unit aspect ratio, perpendicular oncoming wind) represents an important case, in which pollutants emitted inside the canyon become largely trapped and thus susceptible to build up to level that are potentially harmful to human health (DePaul and Sheih, 1985, Xie *et al.*, 2003). It was shown that the pollutant removal process is better simulated with the SB model than with the Smagorinsky model. The additional mixing within the shear layer imparted by the backscatter fluctuations acts to increase the rate of pollutant removal from the street canyon, giving better agreement with a recent WT experiment. The exchange velocity, an important parameter in many operational models that determines the mass transfer between the urban canopy and the external flow, was predicted to be around 15% larger with the SB model; consequently, the steady-state mean pollutant concentration within the street canyon was seen to be around 15% lower. The SB

model was also able to better capture the expected mean wall concentration profiles within the street canyon.

7.2 Limitations and further work

It is important to identify the main limitations of the work undertaken in this thesis so that they can either be taken into account when employing the new SB model, or tackled in future work. Some of these limitations have already been mentioned in the previous chapters, but are revisited and expanded upon in the discussion below. Although it is attempted to cover a wide range of limitations, the list below should not be considered exhaustive.

It is recalled that the backscatter time-scale is currently based on the numerical model time-step, whereas a more physically appropriate time-scale, based on the life-span of grid-scale fluctuations, could be sought. In this regard, guidance may be taken from the work of Schumann (1995), whose SB model imposes stress fluctuations with time-scales that are proportional to the turnover times of the grid-scale eddies, or the work of Xie and Castro (2008), whose turbulent inflow generation procedure also facilitates an appropriate Lagrangian time-scale. In both cases, this is achieved by introducing an appropriate degree of correlation between the contiguous random fields using a prescribed autocorrelation function. A similar extension to the current SB scheme might be explored in future work. It is, however, important to ensure that any such modifications to the SB model do not lead to a violation of the requirement for Galilean invariance (Pope, 2000). Furthermore, it should be checked that any such modification is warranted in terms of its impact on simulation accuracy versus its computational expense (Mason and Brown, 1994).

It is also recalled that, in its current state, the new SB model is specifically formulated for the simulation of neutral atmospheric flows only. Future developments of the model might

therefore focus on increasing the range of atmospheric stabilities over which it can be applied. Again, guidance may be taken from previous work, e.g. Brown *et al.* (1994) who developed the MT92 model towards simulating the stably stratified ABL by imposing a stability dependence via the gradient Richardson number.

Another criticism that could be made of the new SB model is that it presently requires *a priori* specification of the level of backscatter anisotropy and vertical momentum flux, based (typically) on empirical estimates of the grid-scale anisotropy and shear stresses. In order to improve the generality of the model, it may be worth exploring the implementation of a 'dynamic' approach (Germano *et al.*, 1991) in future work, in which these turbulence properties are evaluated locally at each time-step based on the application of an additional test filter.

In Chapter 2, it was discussed how the Smagorinsky SGS model only seeks to represent the net energy drain towards the subgrid scales, whilst the SB modelling approach attempts to represent both the forward and reverse energy transfer processes separately. However, it should be noted that the SB model retains the Smagorinsky scheme for the forward energy transfer part. It may be worth exploring whether there are other (more appropriate) schemes for handling this forward-scatter part. Since the eddy interactions that produce forward-scatter across the LES cut-off scale involve at least one subgrid eddy (about which information is inherently unknown), it seems reasonable to again consider a stochastic approach for handling such interactions.

In the street canyon case, a significant amount of the subgrid-scale TKE within the roof-level shear layer is generated (rather than cascaded) by shear instability. However, the SB model presently specifies that the backscatter energy is proportional to the dissipation rate. If the

shear layer is not spatially developing then the use of the dissipation rate remains valid, since the assumption of equilibrium between TKE production and dissipation still holds. However, there may be scope to develop the SB scheme so that it considers the production rate; the energy backscatter rate would then be proportional to the mean shear.

As previously noted, the street canyon configuration tested in this thesis – of neutrally stratified perpendicular flow over a 2-D street canyon of unity aspect ratio – represents only one (albeit important) example of the many street canyon configurations, and atmospheric conditions, encountered in the real urban canopy layer. In order for the LES (with SB) model output to be used to improve operational urban dispersion models, a more comprehensive database of usable parameters (e.g. exchange velocities) must first be generated by testing a much wider range of street canyon configurations, as well as incorporating a wider-ranging set of physical considerations; some examples are provided below:

- Street canyon aspect ratio: The ratio of the building height to street width can greatly affect the flow regime, and thus pollutant dispersion, within the canyon, with deeper canyons exhibiting counter-rotating vortices that typically lead to heightened ground-level concentrations (Oke, 1987, Liu *et al.*, 2004, Liu *et al.*, 2005, Chung and Liu, 2013, Zhong *et al.*, 2015).
- Asymmetric street canyons: Step-up (downwind building taller than the upwind building) and step-down (vice-versa) canyons can significantly affect the flow-field and pollutant transport (Hoydysh and Dabberdt, 1988, Assimakopoulos *et al.*, 2003).
- Intersection effects: Clearly, real urban street canyons are not infinitely long, and intersection effects will lead to complex flow patterns that include flow separation, thus affecting pollutant dilution, e.g. Soulhac *et al.* (2001)

- Vegetation effects: Trees (and other obstacles) within the street canyon will affect the local wind field (Gu *et al.*, 2010, Gromke and Ruck, 2012), and may also increase pollutant deposition.
- Wind direction and inclination: Channelling effects are encountered when the oncoming wind is not exactly perpendicular to the street canyon (Kim and Baik, 2004), and inflow inclined towards the street has been shown to increase pollutant dilution efficiency (Huang *et al.*, 2000).
- Inflow turbulence intensity: Studies have shown that changes in the characteristics of the turbulent structures transported towards the street canyon from the external flow can affect pollutant removal from the canyon (Kim and Baik, 2003, Salizzoni *et al.*, 2009, Michioka *et al.*, 2011, Michioka and Sato, 2012).
- Thermal effects: Changes in thermal stratifications (Cheng and Liu, 2011b) and differential wall heating (Cai, 2012a, Cai, 2012b) have also been shown to affect dispersion and ventilation within street canyons.
- Vehicle-induced turbulence: Additional turbulence caused by vehicles within the street canyon can contribute to the transport and dispersion of the emitted ground-level pollutants (Solazzo *et al.*, 2008).
- Chemistry effects: For reactive pollutants, the chemical processes that occur within the street canyon will affect pollutant concentrations and should therefore be taken into consideration (Baker *et al.*, 2004, Bright *et al.*, 2013, Zhong *et al.*, 2015).

The versatility of the new SB model, in terms of its ability to control key physical properties of the imposed backscatter independently of numerical aspects (i.e. the model grid), widens its applicability to a range of complex flows, and should thus allow a systematic investigation of other urban configurations to be carried out with relative ease.

APPENDIX: FORTRAN CODE EXTRACTS

As discussed in the main body of the thesis, the new SB model was coded into the RAMS LES model using the FORTRAN programming language. Although the entire code is too long (over 2000 lines) to include here in its entirety, the main calling routine (for the street canyon simulations) is shown below, which is intended to provide the reader with an overall picture of how the SB model is actually implemented.

The code below is inserted near the beginning of the 'DIFFUSE' subroutine in the RAMS model file named 'rturb2a.model'. This subroutine is called once every model time-step and is the sub-driver used to compute tendencies due to subgrid-scale turbulence. First, some variable declarations are given:

```
C ======Backscatter variables=======================
      INTEGER KBSMIN,KBSMAX,IBSMIN,IBSMAX,JBSMIN,JBSMAX,iUseBS,iFLTZ
      INTEGER iFLTX,iFLTY,iUseTB,iFLTET,iTBXOP
      INTEGER iFLTE,iDEFE,NTB,iBSXOP,iSCALE,iPCSF,iDEFLB,iAVERE,nFLDS
      REAL BSLEN,CB,nLB,CBT
      PARAMETER (KBSMIN=49) !\
      PARAMETER (KBSMAX=69) ! \
      PARAMETER (IBSMIN=4)  !  \_ Define 3D box inside which backscatter
      PARAMETER (IBSMAX=78) !  /  is applied (min & max i,j,k indices)
      PARAMETER (JBSMIN=1)  ! /
      PARAMETER (JBSMAX=40) !/
      PARAMETER (iUseBS=1)  !Apply backscatter?
      PARAMETER (iUseTB=0)  !Apply scalar backscatter?
      PARAMETER (CB=1.4)    !Backscatter coefficient
      PARAMETER (iFLTE=1)   !Filter dissipation field (with BS filter)?
      PARAMETER (BSLEN=1.)  !Lambda in BS length-scale equation
      PARAMETER (iDEFLB=1)  !Definition of LB: Lambda*(DX*DY*DZ)^1/3 (0) or
Lambda*max(DX,DY,DZ) (1)
      PARAMETER (NTB=2)     !New BS field generated every NTB timesteps
      PARAMETER (iBSXOP=0)  !Extra BS output files for debugging?
      PARAMETER (iSCALE=0)  !Point-wise (0) or horizontal average (1) pre-
curl scaling factor?
      PARAMETER (nLB=3.1)   !Number of LBs away from filter point for which
weights are calculated
C-----------------------------------------------------------------------
      INTEGER nDims
      PARAMETER (nDims=20)
      REAL BSGRDA(KBSMIN:(KBSMAX+1),IBSMIN:(IBSMAX+1),
     +            JBSMIN:(JBSMAX+1),nDims)
      ! Last dimension:
      ! =1: BS accelerations (x-cpt)
      ! =2: BS accelerations (y-cpt)
      ! =3: BS accelerations (z-cpt)
```

```
       ! =4: LB
       ! =5: LBX
       ! =6: LBY
       ! =7: LBZ
       ! =8: CCX
       ! =9: CCY
       ! =10: CCZ
       ! =11: IIMIN (first non-zero weight in negative x)
       ! =12: IIMAX (first non-zero weight in positive x)
       ! =13: JJMIN
       ! =14: JJMAX
       ! =15: KKMIN
       ! =16: KKMAX
       ! =17: Theoretical BS rate
       ! =18: Pre-curl scaling factor
       ! =19: TB field
       ! =20: Theoretical scalar BS rate
       INTEGER nWgtsX,nWgtsY,nWgtsZ
       INTEGER IFLMIN,IFLMAX,JFLMIN,JFLMAX,KFLMIN,KFLMAX
       !For memory stuff:
       REAL aa(2),BSWGTX(*),BSWGTY(*),BSWGTZ(*),FLGRDA(*)
       INTEGER*8 iadWtX,iadWtY,iadWtZ,iadFGA
       INTEGER*8 length,nwords,malloc
       POINTER (iadWtX, BSWGTX)
       POINTER (iadWtY, BSWGTY)
       POINTER (iadWtZ, BSWGTZ)
       POINTER (iadFGA, FLGRDA)
C-----------------------------------------------------------------------
       REAL MdGrd1(NZP,NXP,NYP)
       REAL MdGrd2(NZP,NXP,NYP)
       LOGICAL FlExst
       INTEGER ITRPBS,IFTRBS
       REAL FLGRDB(*)
       INTEGER*8 iadFGB
       POINTER (iadFGB, FLGRDB)
       REAL CCan,Cbg,Cmax,Cmin
       INTEGER CmaxI,CmaxJ,CmaxK,CminI,CminJ,CminK
C =========================================================
```

Then, straight after the call to MOMENK (which computes the eddy-viscosity coefficients for momentum), the following calls to the backscatter subroutines are added:

```
C ======Backscatter calls=============================================
C ----Calls for things done on first time-step only:
       IF (iUseBS.EQ.1 .AND. ISTP.EQ.1) THEN
         !Calculate backscatter length-scale and correlation coefficient
components:
         CALL CALCLB(BSGRDA,IBSMIN,IBSMAX,JBSMIN,JBSMAX,KBSMIN,
     +         KBSMAX,ZZ,NZPMAX,DELTAX,DELTAY,BSLEN,nLB,
     +         nWgtsX,nWgtsY,nWgtsZ,IFLMIN,IFLMAX,JFLMIN,JFLMAX,
     +         KFLMIN,KFLMAX,iBSXOP,iDEFLB,nDims)
         !Allocate memory for BSWGTX, BSWGTY, BSWGTZ,FLGRDA:
         length=loc(aa(2))-loc(aa(1)) ! size of a floating real variable
         nwords=(KBSMAX-KBSMIN+1)*(IBSMAX-IBSMIN+1)*
     +          (JBSMAX-JBSMIN+1)*(2*nWgtsX+1)
         iadWtX= malloc(nwords*length)
         nwords=(KBSMAX-KBSMIN+1)*(IBSMAX-IBSMIN+1)*
```

```
     +          (JBSMAX-JBSMIN+1)*(2*nWgtsY+1)
        iadWtY= malloc(nwords*length)
        nwords=(KBSMAX-KBSMIN+1)*(IBSMAX-IBSMIN+1)*
     +          (JBSMAX-JBSMIN+1)*(2*nWgtsZ+1)
        iadWtZ= malloc(nwords*length)
        nwords=(KFLMAX-KFLMIN+1)*(IFLMAX-IFLMIN+1)*
     +          (JFLMAX-JFLMIN+1)*nFLDS*2
        iadFGA= malloc(nwords*length)
        iadFGB= malloc(nwords*length)
        !Calculate filter weights at each (backscatter) grid-point:
        CALL FLTWGT(BSGRDA,IBSMIN,IBSMAX,JBSMIN,JBSMAX,KBSMIN,
     +         KBSMAX,ZZ,NZPMAX,DELTAX,DELTAY,nLB,nWgtsX,nWgtsY,nWgtsZ,
     +         BSWGTX,BSWGTY,BSWGTZ,iBSXOP,nDims)
       ENDIF
C ----New backscatter fields created every NTB time-steps:
       IF(iUseBS.EQ.1. .AND. MOD(ISTP,NTB).EQ.1) THEN
         !Generate random fields on filter grid:
         CALL BSRAND(FLGRDA,IFLMIN,IFLMAX,JFLMIN,JFLMAX,KFLMIN,
     +           KFLMAX,IBSMIN,IBSMAX,JBSMIN,JBSMAX,KBSMIN,
     +           KBSMAX,ISTP,iBSXOP,nFLDS)
         !Apply spatial filter and return BS grid values only
         CALL BSFILT(BSGRDA,IBSMIN,IBSMAX,JBSMIN,JBSMAX,KBSMIN,
     +         KBSMAX,FLGRDA,IFLMIN,IFLMAX,JFLMIN,JFLMAX,KFLMIN,
     +           KFLMAX,BSWGTX,BSWGTY,BSWGTZ,nWgtsX,nWgtsY,nWgtsZ,ISTP,
     +         iBSXOP,nFLDS,iFLTZ,iFLTX,iFLTY,nDims)
         !Calculate theoretical BS rate at each BS grid point:
         CALL BSTHR(BSGRDA,IBSMIN,IBSMAX,JBSMIN,JBSMAX,KBSMIN,
     +         KBSMAX,CB,iFLTE,iDEFE,A(IVT3DC),NZP,NXP,NYP,ISTP,
     +         iBSXOP,iAVERE,BSWGTX,BSWGTY,BSWGTZ,nWgtsX,nWgtsY,nWgtsZ,
     +         nDims,1,IH,L3,L4)
         !Scale filtered fields (pre-curl):
         CALL BSSCL1(BSGRDA,IBSMIN,IBSMAX,JBSMIN,JBSMAX,KBSMIN,
     +         KBSMAX,DELTAX,DELTAY,ZZ,NZPMAX,NTB,DTLONG,ISTP,iBSXOP,
     +         iSCALE,nDims)
         !Curl scaled fields
         CALL BSCURL(BSGRDA,IBSMIN,IBSMAX,JBSMIN,JBSMAX,KBSMIN,
     +         KBSMAX,DELTAX,DELTAY,ZZ,NZPMAX,ISTP,iBSXOP,nDims)
         !Scale filtered fields (post-curl):
         CALL BSSCL2(BSGRDA,IBSMIN,IBSMAX,JBSMIN,JBSMAX,KBSMIN,
     +           KBSMAX,NTB,DTLONG,ISTP,iBSXOP,iPCSF,nDims)
         !Check divergences:
         IF (ISTP.EQ.1 .AND. iBSXOP.EQ.1) THEN
           CALL BSDIV(BSGRDA,IBSMIN,IBSMAX,JBSMIN,JBSMAX,KBSMIN,
     +         KBSMAX,DELTAX,DELTAY,ZZ,NZPMAX,nDims)
         ENDIF
       ENDIF
C ----Backscatter fields added to LES fields every time-step:
       IF(iUseBS.EQ.1) THEN
         CALL BSADD(BSGRDA,IBSMIN,IBSMAX,JBSMIN,JBSMAX,KBSMIN,
     +         KBSMAX,A(IFU),A(IFV),A(IFW),NXP,NYP,NZP,ISTP,iBSXOP,nDims,
     +         IH,L3,L4)
       ENDIF
C ============================================================
```

Finally, one of the above called subroutines is presented below as an example. The subroutine ‘BSADD’ is chosen, which is the subroutine that actually augments the LES acceleration

fields, at every time-step, with the (filtered, scaled and divergence-free) stochastic backscatter accelerations:

```
      SUBROUTINE BSADD(BSGRDA,IBSMIN,IBSMAX,JBSMIN,JBSMAX,KBSMIN,
     +         KBSMAX,FU,FV,FW,NXP,NYP,NZP,ISTP,iBSXOP,nDims,
     +         IH,L3,L4)
C=======================================================================
C--------------------Declarations:---------------------
      IMPLICIT NONE
C-----Arguments:
      INTEGER IBSMIN,IBSMAX,JBSMIN,JBSMAX,KBSMIN,KBSMAX,nDims
      REAL BSGRDA(KBSMIN:(KBSMAX+1),IBSMIN:(IBSMAX+1),
     +            JBSMIN:(JBSMAX+1),nDims)
      INTEGER NXP,NYP,NZP,ISTP,iBSXOP,IH,L3,L4
      REAL FU,FV,FW
      DIMENSION FU(NZP,NXP,NYP),FV(NZP,NXP,NYP),FW(NZP,NXP,NYP)
C-----Local:
      INTEGER I,J,K
C-----------------------------------------------------------

      DO(K=KBSMIN,KBSMAX)
        DO(I=IBSMIN,IBSMAX)
          DO(J=JBSMIN,JBSMAX)
            IF(K.GT.IH .OR. (I.GT.L3 .AND. I.LE.L4)) THEN
              FU(K,I,J)=FU(K,I,J)+BSGRDA(K,I,J,1)
              FV(K,I,J)=FV(K,I,J)+BSGRDA(K,I,J,2)
              FW(K,I,J)=FW(K,I,J)+BSGRDA(K,I,J,3)
            ENDIF
          ENDDO
        ENDDO
      ENDDO

      RETURN
      END
```

Publications arising from this thesis

O'Neill, J.J., Cai, X.-M., Kinnersley, R. 2015. A generalised stochastic backscatter model: large-eddy simulation of the neutral surface layer. *Quarterly Journal of the Royal Meteorological Society*. **141**: 2617-2629, doi: 10.1002/qj.2548.

O'Neill, J.J., Cai, X.-M., Kinnersley, R. 2016. Improvement of a stochastic backscatter model and application to large-eddy simulation of street canyon flow. *Quarterly Journal of the Royal Meteorological Society*. **142**: 1121-1132, doi: 10.1002/qj.2715.

O'Neill, J.J., Cai, X.-M., Kinnersley, R. Stochastic backscatter modelling for the prediction of pollutant removal from an urban street canyon: a large-eddy simulation. Submitted to *Atmospheric Environment* in February 2016 (under review).

List of references

Andreas EL, Claffey KJ, Jordan RE, Fairall CW, Guest PS, Persson POG, Grachev AA. 2006. Evaluations of the von Kármán constant in the atmospheric surface layer. *Journal of Fluid Mechanics*. **559**: 117-149, doi: 10.1017/s0022112006000164

Andren A, Brown AR, Graf J, Mason PJ, Moeng CH, Nieuwstadt FTM, Schumann U. 1994. Large-eddy simulation of a neutrally stratified boundary-layer - a comparison of 4 computer codes. *Quarterly Journal of the Royal Meteorological Society*. **120**: 1457-1484, doi: 10.1002/qj.49712052003

Assimakopoulos VD, ApSimon HM, Moussiopoulos N. 2003. A numerical study of atmospheric pollutant dispersion in different two-dimensional street canyon configurations. *Atmospheric Environment*. **37**: 4037-4049, doi: 10.1016/S1352-2310(03)00533-8

Baik J-J, Kim J-J. 1999. A numerical study of flow and pollutant dispersion characteristics in urban street canyons. *Journal of Applied Meteorology*. **38**: 1576-1589, doi: 10.1175/1520-0450(1999)038<1576:ANSOFA>2.0.CO;2

Baik J-J, Kim J-J. 2002. On the escape of pollutants from urban street canyons. *Atmospheric Environment*. **36**: 527-536, doi: 10.1016/s1352-2310(01)00438-1

Baik J-J, Park R-S, Chun H-Y, Kim J-J. 2000. A laboratory model of urban street-canyon flows. *Journal of Applied Meteorology*. **39**: 1592-1600, doi: 10.1175/1520-0450(2000)039<1592:ALMOUS>2.0.CO;2

Baker J, Walker HL, Cai XM. 2004. A study of the dispersion and transport of reactive pollutants in and above street canyons - a large eddy simulation. *Atmospheric Environment*. **38**: 6883-6892, doi: 10.1016/j.atmosenv.2004.08.051

Basu S, Porte-Agel F. 2006. Large-eddy simulation of stably stratified atmospheric boundary layer turbulence: A scale-dependent dynamic modeling approach. *Journal of the Atmospheric Sciences*. **63**: 2074-2091, doi: 10.1175/jas3734.1

Berkowicz R. 2000. OSPM—a parameterised street pollution model. In *Urban Air Quality: Measurement, Modelling and Management*. Springer; 323-331.

Berner J, Doblas-Reyes FJ, Palmer TN, Shutts G, Weisheimer A. 2008. Impact of a quasi-stochastic cellular automaton backscatter scheme on the systematic error and seasonal prediction skill of a global climate model. *Philosophical Transactions of the Royal Society of London A: Mathematical, Physical and Engineering Sciences*. **366**: 2559-2577, doi: 10.1098/rsta.2008.0033

Blackman K, Perret L, Savory E, Piquet T. 2015. Field and wind tunnel modeling of an idealized street canyon flow. *Atmospheric Environment*. **106**: 139-153, doi: 10.1016/j.atmosenv.2015.01.067

Boppana VBL, Xie ZT, Castro IP. 2010. Large-eddy simulation of dispersion from surface sources in arrays of obstacles. *Boundary-Layer Meteorology*. **135**: 433-454, doi: 10.1007/s10546-010-9489-9

Bou-Zeid E, Meneveau C, Parlange M. 2005. A scale-dependent Lagrangian dynamic model for large eddy simulation of complex turbulent flows. *Physics of Fluids*. **17**: 025105, doi: 10.1063/1.1839152

Bowler NE, Arribas A, Beare SE, Mylne KR, Shutts GJ. 2009. The local ETKF and SKEB: Upgrades to the MOGREPS short-range ensemble prediction system. *Quarterly Journal of the Royal Meteorological Society*. **135**: 767-776, doi: 10.1002/qj.394

Brasseur JG, Wei T. 2010. Designing large-eddy simulation of the turbulent boundary layer to capture law-of-the-wall scaling. *Physics of Fluids*. **22**: 021303, doi: 10.1063/1.3319073

Bright VB, Bloss WJ, Cai X. 2013. Urban street canyons: Coupling dynamics, chemistry and within-canyon chemical processing of emissions. *Atmospheric Environment*. **68**: 127-142, doi: 10.1016/j.atmosenv.2012.10.056

Brown AR, Derbyshire SH, Mason PJ. 1994. Large-eddy simulation of stable atmospheric boundary-layers with a revised stochastic subgrid model. *Quarterly Journal of the Royal Meteorological Society*. **120**: 1485-1512, doi: 10.1002/qj.49712052004

Brown MJ, Lawson R, Decroix D, Lee R. 2000. Mean flow and turbulence measurements around a 2-D array of buildings in a wind tunnel. In *Proceedings of the 11th Joint AMS/AWMA conference on the applications of air pollution, Long Beach, CA, USA, January 2000.*

Businger JA, Wyngaard JC, Izumi Y, Bradley EF. 1971. Flux-profile relationships in the atmospheric surface layer. *Journal of the Atmospheric Sciences*. **28**: 181-189, doi: 10.1175/1520-0469(1971)028<0181:fprita>2.0.co;2

Cai X. 2012a. Effects of differential wall heating in street canyons on dispersion and ventilation characteristics of a passive scalar. *Atmospheric Environment*. **51**: 268-277, doi: 10.1016/j.atmosenv.2012.01.010

Cai XM. 1999. Large-eddy simulation of the convective boundary layer over an idealized patchy urban surface. *Quarterly Journal of the Royal Meteorological Society*. **125**: 1427-1444, doi: 10.1256/smsqj.55615

Cai XM. 2012b. Effects of wall heating on flow characteristics in a street canyon. *Boundary-Layer Meteorology*. **142**: 443-467, doi: 10.1007/s10546-011-9681-6

Cai XM, Barlow JF, Belcher SE. 2008. Dispersion and transfer of passive scalars in and above street canyons - Large-eddy simulations. *Atmospheric Environment*. **42**: 5885-5895, doi: 10.1016/j.atmosenv.2008.03.040

Cai XM, Steyn DG. 1996. The von Karman constant determined by large eddy simulation. *Boundary-Layer Meteorology*. **78**: 143-164, doi: 10.1007/bf00122490

Carruthers DJ, Holroyd RJ, Hunt JCR, Weng WS, Robins AG, Apsley DD, Thompson DJ, Smith FB. 1994. UK-ADMS: A new approach to modelling dispersion in the earth's atmospheric boundary layer. *Journal of Wind Engineering and Industrial Aerodynamics*. **52**: 139-153, doi: 10.1016/0167-6105(94)90044-2

Chamecki M. 2010. Modeling subgrid-scale heat fluxes in the neutral and stratified atmospheric boundary layer. *Journal of Turbulence*. **11**: 1-16, doi: 10.1080/14685241003785881

Chasnov JR. 1991. Simulation of the Kolmogorov inertial subrange using an improved subgrid model. *Physics of Fluids A-Fluid Dynamics*. **3**: 188-200, doi: 10.1063/1.857878

Cheng WC, Liu C-H. 2011a. Large-eddy simulation of flow and pollutant transports in and above two-dimensional idealized street canyons. *Boundary-Layer Meteorology*. **139**: 411-437, doi: 10.1007/s10546-010-9584-y

Cheng WC, Liu C-H. 2011b. Large-eddy simulation of turbulent transports in urban street canyons in different thermal stabilities. *Journal of Wind Engineering and Industrial Aerodynamics*. **99**: 434-442, doi: 10.1016/j.jweia.2010.12.009

Cheng WC, Liu C-H, Leung DYC. 2008. Computational formulation for the evaluation of street canyon ventilation and pollutant removal performance. *Atmospheric Environment*. **42**: 9041-9051, doi: 10.1016/j.atmosenv.2008.09.045

Cheng WC, Porte-Agel F. 2015. Adjustment of turbulent boundary-layer flow to idealized urban surfaces: A large-eddy simulation study. *Boundary-Layer Meteorology*. **155**: 249-270, doi: 10.1007/s10546-015-0004-1

Chow FK, Street RL, Xue M, Ferziger JH. 2005. Explicit filtering and reconstruction turbulence modeling for large-eddy simulation of neutral boundary layer flow. *Journal of the Atmospheric Sciences*. **62**: 2058-2077, doi: 10.1175/jas3456.1

Chung TNH, Liu C-H. 2013. On the mechanism of air pollutant removal in two-dimensional idealized street canyons: A large-eddy simulation approach. *Boundary-Layer Meteorology*. **148**: 241-253, doi: 10.1007/s10546-013-9811-4

Cui ZQ, Cai XM, Baker CJ. 2004. Large-eddy simulation of turbulent flow in a street canyon. *Quarterly Journal of the Royal Meteorological Society*. **130**: 1373-1394, doi: 10.1256/qj.02.150

Davidson PA. 2004. *Turbulence: An Introduction for Scientists and Engineers: An Introduction for Scientists and Engineers.* Oxford University Press.

Deardorff J. 1970a. A three-dimensional numerical investigation of the idealized planetary boundary layer. *Geophysical and Astrophysical Fluid Dynamics*. **1**: 377-410, doi: 10.1080/03091927009365780

Deardorff JW. 1970b. A numerical study of three-dimensional turbulent channel flow at large Reynolds numbers. *Journal of Fluid Mechanics*. **41**: 453-480, doi: 10.1017/S0022112070000691

Deardorff JW. 1972. Numerical investigation of neutral and unstable planetary boundary-layers. *Journal of the Atmospheric Sciences*. **29**: 91-115, doi: 10.1175/1520-0469(1972)029<0091:nionau>2.0.co;2

Dejoan A, Santiago JL, Martilli A, Martin F, Pinelli A. 2010. Comparison between large-eddy simulation and Reynolds-averaged Navier-Stokes computations for the MUST field experiment. Part II: Effects of incident wind angle deviation on the mean flow and plume dispersion. *Boundary-Layer Meteorology*. **135**: 133-150, doi: 10.1007/s10546-010-9467-2

DePaul FT, Sheih CM. 1985. A tracer study of dispersion in an urban street canyon. *Atmospheric Environment*. **19**: 555-559, doi: 10.1016/0004-6981(85)90034-4

Di Bernardino A, Monti P, Leuzzi G, Querzoli G. 2015. Water-channel study of flow and turbulence past a two-dimensional array of obstacles. *Boundary-Layer Meteorology*. **155**: 73-85, doi: 10.1007/s10546-014-9987-2

Domaradzki JA, Saiki EM. 1997. Backscatter models for large-eddy simulations. *Theoretical and Computational Fluid Dynamics*. **9**: 75-83, doi: 10.1007/s001620050033

Eyink GL. 1996. Turbulence noise. *Journal of Statistical Physics*. **83**: 955-1019, doi: 10.1007/bf02179551

Frederiksen JS, Davies AG. 1997. Eddy viscosity and stochastic backscatter parameterizations on the sphere for atmospheric circulation models. *Journal of the Atmospheric Sciences*. **54**: 2475-2492, doi: 10.1175/1520-0469(1997)054<2475:evasbp>2.0.co;2

Frenzen P, Vogel CA. 1995. On the magnitude and apparent range of variation of the von Kármán constant in the atmospheric surface-layer. *Boundary-Layer Meteorology*. **72**: 371-392, doi: 10.1007/bf00709000

Garratt JR. 1994. *The atmospheric boundary layer.* Cambridge University Press: Cambridge, UK.

Germano M, Piomelli U, Moin P, Cabot WH. 1991. A dynamic subgrid-scale eddy viscosity model. *Physics of Fluids A-Fluid Dynamics*. **3**: 1760-1765, doi: 10.1063/1.857955

Geurts BJ. 2004. *Elements of direct and large-eddy simulation.* R.T. Edwards: Philadelphia, USA.

Gicquel LYM, Givi P, Jaberi FA, Pope SB. 2002. Velocity filtered density function for large eddy simulation of turbulent flows. *Physics of Fluids*. **14**: 1196-1213, doi: 10.1063/1.1436496

Grant ALM. 1986. Observations of boundary layer structure made during the 1981 KONTUR experiment. *Quarterly Journal of the Royal Meteorological Society*. **112**: 825-841, doi: 10.1002/qj.49711247314

Gromke C, Ruck B. 2012. Pollutant concentrations in street canyons of different aspect ratio with avenues of trees for various wind directions. *Boundary-Layer Meteorology*. **144**: 41-64, doi: 10.1007/s10546-012-9703-z

Grooms I, Lee Y, Majda AJ. 2015. Numerical schemes for stochastic backscatter in the inverse cascade of quasigeostrophic turbulence. *Multiscale Modeling & Simulation*. **13**: 1001-1021, doi: 10.1137/140990048

Gu Z, Zhang Y, Lei K. 2010. Large eddy simulation of flow in a street canyon with tree planting under various atmospheric instability conditions. *Science China-Technological Sciences*. **53**: 1928-1937, doi: 10.1007/s11431-010-3243-x

Hinze JO. 1972. *Turbulence. Second Edition.* McGraw-Hill: USA.

Hoydysh WG, Dabberdt WF. 1988. Kinematics and dispersion characteristics of flows in asymmetric street canyons. *Atmospheric Environment (1967)*. **22**: 2677-2689, doi: 10.1016/0004-6981(88)90436-2

Huang H, Akutsu Y, Arai M, Tamura M. 2000. A two-dimensional air quality model in an urban street canyon: evaluation and sensitivity analysis. *Atmospheric Environment*. **34**: 689-698, doi: 10.1016/S1352-2310(99)00333-7

Inagaki A, Castillo MCL, Yamashita Y, Kanda M, Takimoto H. 2012. Large-eddy simulation of coherent flow structures within a cubical canopy. *Boundary-Layer Meteorology*. **142**: 207-222, doi: 10.1007/s10546-011-9671-8

Jeong SJ, Andrews MJ. 2002. Application of the *k–ε* turbulence model to the high Reynolds number skimming flow field of an urban street canyon. *Atmospheric Environment*. **36**: 1137-1145, doi: 10.1016/S1352-2310(01)00569-6

Kaimal JC, Wyngaard JC, Izumi Y, Coté R. 1972. Spectral characteristics of surface-layer turbulence. *Quarterly Journal of the Royal Meteorological Society*. **98**: 563-589, doi: 10.1002/qj.49709841707

Kastner-Klein P, Plate EJ. 1999. Wind-tunnel study of concentration fields in street canyons. *Atmospheric Environment*. **33**: 3973-3979, doi: 10.1016/s1352-2310(99)00139-9

Keller L, Friedmann A. Differentialgleichungen für die turbulente Bewegung einer kompressiblen Flüssigkeit. In *Proceedings of the Proc. First. Int. Congr. Appl. Mech, 1924.*

Kim J-J, Baik J-J. 2003. Effects of inflow turbulence intensity on flow and pollutant dispersion in an urban street canyon. *Journal of Wind Engineering and Industrial Aerodynamics*. **91**: 309-329, doi: 10.1016/S0167-6105(02)00395-1

Kim J-J, Baik J-J. 2004. A numerical study of the effects of ambient wind direction on flow and dispersion in urban street canyons using the RNG k–ε turbulence model. *Atmospheric Environment*. **38**: 3039-3048, doi: 10.1016/j.atmosenv.2004.02.047

Kim Y, Castro IP, Xie Z-T. 2013. Divergence-free turbulence inflow conditions for large-eddy simulations with incompressible flow solvers. *Computers & Fluids*. **84**: 56-68, doi: 10.1016/j.compfluid.2013.06.001

Kirkil G, Mirocha J, Bou-Zeid E, Chow FK, Kosovic B. 2012. Implementation and evaluation of dynamic subfilter-scale stress models for large-eddy simulation using WRF. *Monthly Weather Review*. **140**: 266-284, doi: 10.1175/mwr-d-11-00037.1

Klein M, Sadiki A, Janicka J. 2003. A digital filter based generation of inflow data for spatially developing direct numerical or large eddy simulations. *Journal of Computational Physics*. **186**: 652-665, doi: 10.1016/s0021-9991(03)00090-1

Kolmogorov AN. The local structure of turbulence in incompressible viscous fluid for very large Reynolds numbers. In *Proceedings of the Dokl. Akad. Nauk SSSR, 1941.* JSTOR:

Kosović B. 1997. Subgrid-scale modelling for the large-eddy simulation of high-Reynolds-number boundary layers. *Journal of Fluid Mechanics*. **336**: 151-182, doi: 10.1017/s0022112096004697

Kosović B, Pullin DI, Samtaney R. 2002. Subgrid-scale modeling for large-eddy simulations of compressible turbulence. *Physics of Fluids*. **14**: 1511-1522, doi: 10.1063/1.1458006

Kravchenko AG, Moin P, Moser R. 1996. Zonal embedded grids for numerical simulations of wall-bounded turbulent flows. *Journal of Computational Physics*. **127**: 412-423, doi: 10.1006/jcph.1996.0184

Laval JP, Dubrulle B. 2006. A LES-Langevin model for turbulence. *European Physical Journal B*. **49**: 471-481, doi: 10.1140/epjb/e2006-00082-4

Lee IY, Park HM. 1994. Parameterization of the pollutant transport and dispersion in urban street canyons. *Atmospheric Environment*. **28**: 2343-2349, doi: 10.1016/1352-2310(94)90488-x

Leith CE. 1990. Stochastic backscatter in a subgrid-scale model - plane shear mixing layer. *Physics of Fluids A-Fluid Dynamics*. **2**: 297-299, doi: 10.1063/1.857779

Leslie DC, Quarini GL. 1979. Application of turbulence theory to the formulation of sub-grid modeling procedures. *Journal of Fluid Mechanics*. **91**: 65-91, doi: 10.1017/s0022112079000045

Letzel MO, Krane M, Raasch S. 2008. High resolution urban large-eddy simulation studies from street canyon to neighbourhood scale. *Atmospheric Environment*. **42**: 8770-8784, doi: 10.1016/j.atmosenv.2008.08.001

Li X-X, Leung DYC, Liu C-H, Lam KM. 2008a. Physical modeling of flow field inside urban street canyons. *Journal of Applied Meteorology and Climatology*. **47**: 2058-2067, doi: 10.1175/2007jamc1815.1

Li X-X, Liu C-H, Leung DYC. 2008b. Large-eddy simulation of flow and pollutant dispersion in high-aspect-ratio urban street canyons with wall model. *Boundary-Layer Meteorology*. **129**: 249-268, doi: 10.1007/s10546-008-9313-y

Li X-X, Liu C-H, Leung DYC. 2009. Numerical investigation of pollutant transport characteristics inside deep urban street canyons. *Atmospheric Environment*. **43**: 2410-2418, doi: 10.1016/j.atmosenv.2009.02.022

Li X-X, Liu C-H, Leung DYC, Lam KM. 2006. Recent progress in CFD modelling of wind field and pollutant transport in street canyons. *Atmospheric Environment*. **40**: 5640-5658, doi: 10.1016/j.atmosenv.2006.04.055

Li XX, Liu CH, Leung DYC. 2005. Development of a k–ε model for the determination of air exchange rates for street canyons. *Atmospheric Environment*. **39**: 7285-7296, doi: 10.1016/j.atmosenv.2005.09.007

Lilly DK. 1967. The representation of small-scale turbulence in numerical simulation experiments. *Proceedings of IBM Scientific Computing Symposium on Environmental Sciences*. 195-210

Lilly DK. 1992. A proposed modification of the Germano subgrid-scale closure method. *Physics of Fluids A*. **4**: 633-635, doi: 10.1063/1.858280

Liu C-H, Wong CCC. 2014. On the pollutant removal, dispersion, and entrainment over two-dimensional idealized street canyons. *Atmospheric Research*. **135**: 128-142, doi: 10.1016/j.atmosres.2013.08.006

Liu CH, Barth MC. 2002. Large-eddy simulation of flow and scalar transport in a modeled street canyon. *Journal of Applied Meteorology*. **41**: 660-673, doi: 10.1175/1520-0450(2002)041<0660:lesofa>2.0.co;2

Liu CH, Barth MC, Leung DYC. 2004. Large-eddy simulation of flow and pollutant transport in street canyons of different building-height-to-street-width ratios. *Journal of Applied Meteorology*. **43**: 1410-1424, doi: 10.1175/jam2143.1

Liu CH, Leung DYC, Barth MC. 2005. On the prediction of air and pollutant exchange rates in street canyons of different aspect ratios using large-eddy simulation. *Atmospheric Environment*. **39**: 1567-1574, doi: 10.1016/j.atmosenv.2004.08.036

Louka P, Belcher S, Harrison R. 2000. Coupling between air flow in streets and the well-developed boundary layer aloft. *Atmospheric Environment*. **34**: 2613-2621, doi: 10.1016/S1352-2310(99)00477-X

Lu H, Porté-Agel F. 2014. On the development of a dynamic non-linear closure for large-eddy simulation of the atmospheric boundary layer. *Boundary-Layer Meteorology*. **151**: 429-451, doi: 10.1007/s10546-013-9906-y

Mason PJ. 1994. Large-eddy simulation - A critical-review of the technique. *Quarterly Journal of the Royal Meteorological Society*. **120**: 1-26, doi: 10.1002/qj.49712051503

Mason PJ, Brown AR. 1994. The sensitivity of large-eddy simulation of turbulent shear flow to subgrid models. *Boundary-Layer Meteorology*. **70**: 133-150, doi: 10.1007/bf00712526

Mason PJ, Brown AR. 1999. On subgrid models and filter operations in large eddy simulations. *Journal of the Atmospheric Sciences*. **56**: 2101-2114, doi: 10.1175/1520-0469(1999)056<2101:osmafo>2.0.co;2

Mason PJ, Callen NS. 1986. On the magnitude of the subgrid-scale eddy coefficient in large-eddy simulations of turbulent channel flow. *Journal of Fluid Mechanics*. **162**: 439-462, doi: 10.1017/s0022112086002112

Mason PJ, Thomson DJ. 1987. LARGE-EDDY SIMULATIONS OF THE NEUTRAL-STATIC-STABILITY PLANETARY BOUNDARY-LAYER. *Quarterly Journal of the Royal Meteorological Society*. **113**: 413-443, doi: 10.1256/smsqj.47601

Mason PJ, Thomson DJ. 1992. Stochastic backscatter in large-eddy simulations of boundary-layers. *Journal of Fluid Mechanics*. **242**: 51-78, doi: 10.1017/s0022112092002271

Meroney RN, Pavageau M, Rafailidis S, Schatzmann M. 1996. Study of line source characteristics for 2-D physical modelling of pollutant dispersion in street canyons. *Journal of Wind Engineering and Industrial Aerodynamics*. **62**: 37-56, doi: 10.1016/s0167-6105(96)00057-8

Michioka T, Chow FK. 2008. High-resolution large-eddy simulations of scalar transport in atmospheric boundary layer flow over complex terrain. *Journal of Applied Meteorology and Climatology*. **47**: 3150-3169, doi: 10.1175/2008jamc1941.1

Michioka T, Sato A. 2012. Effect of incoming turbulent structure on pollutant removal from two-dimensional street canyon. *Boundary-Layer Meteorology*. **145**: 469-484, doi: 10.1007/s10546-012-9733-6

Michioka T, Sato A, Takimoto H, Kanda M. 2011. Large-eddy simulation for the mechanism of pollutant removal from a two-dimensional street canyon. *Boundary-Layer Meteorology*. **138**: 195-213, doi: 10.1007/s10546-010-9556-2

Mirocha J, Kirkil G, Bou-Zeid E, Chow FK, Kosović B. 2012. Transition and equilibration of neutral atmospheric boundary layer flow in one-way nested large-eddy simulations using the Weather Research and Forecasting model. *Monthly Weather Review*. **141**: 918-940, doi: 10.1175/mwr-d-11-00263.1

Mirocha JD, Lundquist JK, Kosovic B. 2010. Implementation of a nonlinear subfilter turbulence stress model for large-eddy simulation in the Advanced Research WRF model. *Monthly Weather Review*. **138**: 4212-4228, doi: 10.1175/2010mwr3286.1

Moeng CH. 1984. A large-eddy-simulation model for the study of planetary boundary-layer turbulence. *Journal of the Atmospheric Sciences*. **41**: 2052-2062, doi: 10.1175/1520-0469(1984)041<2052:alesmf>2.0.co;2

O'Neill JJ, Cai X-M, Kinnersley R. 2015. A generalised stochastic backscatter model: large-eddy simulation of the neutral surface layer. *Quarterly Journal of the Royal Meteorological Society*. **141**: 2617-2629, doi: 10.1002/qj.2548

O'Neill JJ, Cai X-M, Kinnersley R. 2016. Improvement of a stochastic backscatter model and application to large-eddy simulation of street canyon flow. *Quarterly Journal of the Royal Meteorological Society*. **142**: 1121-1132, doi: 10.1002/qj.2715

O'Neill JJ, Cai X-M, Kinnersley R. under review. Stochastic backscatter modelling for the prediction of pollutant removal from an urban street canyon: a large-eddy simulation. *Atmospheric Environment*.

Oke TR. 1987. *Boundary Layer Climates. Second Edition.* Methuen: London, UK.

Oke TR. 1988. Street design and urban canopy layer climate. *Energy and buildings*. **11**: 103-113, doi: 10.1016/0378-7788(88)90026-6

Palmer T, Buizza R, Doblas-Reyes F, Jung T, Leutbecher M, Shutts G, Steinheimer M, Weisheimer A. 2009. *Stochastic Parametrization and Model Uncertainty. ECMWF Technical Memorandum **598***. European Centre for Medium-Range Weather Forecasts: Reading, UK.

Palmer TN. 2001. A nonlinear dynamical perspective on model error: A proposal for non-local stochastic-dynamic parametrization in weather and climate prediction models. *Quarterly Journal of the Royal Meteorological Society*. **127**: 279-304, doi: 10.1002/qj.49712757202

Park SB, Baik JJ. 2013. A large-eddy simulation study of thermal effects on turbulence coherent structures in and above a building array. *Journal of Applied Meteorology and Climatology*. **52**: 1348-1365, doi: 10.1175/jamc-d-12-0162.1

Pavageau M. 1996. Concentration fluctuations in urban street canyons—groundwork for future studies. *Technical report, Meteorological Institute of the University of Hamburg*. **97**

Pavageau M, Schatzmann M. 1999. Wind tunnel measurements of concentration fluctuations in an urban street canyon. *Atmospheric Environment*. **33**: 3961-3971, doi: 10.1016/S1352-2310(99)00138-7

Pielke R, Cotton W, Walko R, Tremback C, Lyons W, Grasso L, Nicholls M, Moran M, Wesley D, Lee T, Copeland J. 1992. A comprehensive meteorological modeling system—RAMS. *Meteorology and Atmospheric Physics*. **49**: 69-91, doi: 10.1007/BF01025401

Pielke RA. 2002. *Mesoscale meteorological modeling. 2nd.* Academic Press.

Piomelli U, Balaras E. 2002. Wall-layer models for large-eddy simulations. *Annual Review of Fluid Mechanics*. **34**: 349-374, doi: 10.1146/annurev.fluid.34.082901.144919

Piomelli U, Kang S, Ham F, Iaccarino G. 2006. Effect of discontinuous filter width in large-eddy simulations of plane channel flow. *Center for Turbulence Research, Proceedings of the Summer Program 2006*. 151-162

Pope SB. 2000. *Turbulent Flows.* Cambridge Universiy Press: Cambridge, UK.

Porté-Agel F, Meneveau C, Parlange MB. 2000. A scale-dependent dynamic model for large-eddy simulation: application to a neutral atmospheric boundary layer. *Journal of Fluid Mechanics*. **415**: 261-284, doi: 10.1017/s0022112000008776

Richardson LF. 1920. The supply of energy from and to atmospheric eddies. *Proceedings of the Royal Society of London. Series A, Containing Papers of a Mathematical and Physical Character*. 354-373

Salim SM, Buccolieri R, Chan A, Di Sabatino S. 2011a. Numerical simulation of atmospheric pollutant dispersion in an urban street canyon: Comparison between RANS and LES. *Journal of Wind Engineering and Industrial Aerodynamics*. **99**: 103-113, doi: 10.1016/j.jweia.2010.12.002

Salim SM, Cheah SC, Chan A. 2011b. Numerical simulation of dispersion in urban street canyons with avenue-like tree plantings: Comparison between RANS and LES. *Build. Environ.* **46**: 1735-1746, doi: 10.1016/j.buildenv.2011.01.032

Salizzoni P, Soulhac L, Mejean P. 2009. Street canyon ventilation and atmospheric turbulence. *Atmospheric Environment*. **43**: 5056-5067, doi: 10.1016/j.atmosenv.2009.06.045

Santiago JL, Dejoan A, Martilli A, Martin F, Pinelli A. 2010. Comparison between large-eddy simulation and Reynolds-averaged Navier-Stokes computations for the MUST field experiment. Part I: Study of the flow for an incident wind directed perpendicularly to the front array of containers. *Boundary-Layer Meteorology*. **135**: 109-132, doi: 10.1007/s10546-010-9466-3

Schumann U. 1975. Subgrid scale model for finite difference simulations of turbulent flows in plane channels and annuli. *Journal of Computational Physics*. **18**: 376-404, doi: 10.1016/0021-9991(75)90093-5

Schumann U. 1995. Stochastic backscatter of turbulence energy and scalar variance by random subgrid-scale fluxes. *Proceedings of the Royal Society-Mathematical and Physical Sciences*. **451**: 293-318, doi: 10.1098/rspa.1995.0126

Shutts G. 2005. A kinetic energy backscatter algorithm for use in ensemble prediction systems. *Quarterly Journal of the Royal Meteorological Society*. **131**: 3079-3102, doi: 10.1256/qj.04.106

Shutts G. 2009. Stochastic backscatter in the Unified Model. *MOSAC-14*. **14.5**

Simoëns S, Wallace JM. 2008. The flow across a street canyon of variable width—Part 2: Scalar dispersion from a street level line source. *Atmospheric Environment*. **42**: 2489-2503, doi: 10.1016/j.atmosenv.2007.12.013

Smagorinsky J. 1963. General circulation experiments with the primitive equations. *Monthly Weather Review*. **91**: 99-164, doi: 10.1175/1520-0493(1963)091<0099:gcewtp>2.3.co;2

Solazzo E, Cai X, Vardoulakis S. 2008. Modelling wind flow and vehicle-induced turbulence in urban streets. *Atmospheric Environment*. **42**: 4918-4931, doi: 10.1016/j.atmosenv.2008.02.032

Soulhac L, Mejean P, Perkins R. 2001. Modelling the transport and dispersion of pollutants in street canyons. *International journal of environment and pollution*. **16**: 404-413, doi: 10.1504/ijep.2001.000636

Stull RB. 1988. *An introduction to boundary layer meteorology.* Kluwer Academic Publishers: Dordrecht.

Sullivan PP, Horst TW, Lenschow DH, Moeng CH, Weil JC. 2003. Structure of subfilter-scale fluxes in the atmospheric surface layer with application to large-eddy simulation modelling. *Journal of Fluid Mechanics*. **482**: 101-139, doi: 10.1017/s0022112003004099

Sullivan PP, McWilliams JC, Moeng CH. 1994. A subgrid-scale model for large-eddy simulation of planetary boundary-layer flows. *Boundary-Layer Meteorology*. **71**: 247-276, doi: 10.1007/bf00713741

Talbot C, Bou-Zeid E, Smith J. 2012. Nested mesoscale large-eddy simulations with WRF: Performance in real test cases. *Journal of Hydrometeorology*. **13**: 1421-1441, doi: 10.1175/jhm-d-11-048.1

Tominaga Y, Stathopoulos T. 2010. Numerical simulation of dispersion around an isolated cubic building: Model evaluation of RANS and LES. *Build. Environ.* **45**: 2231-2239, doi: 10.1016/j.buildenv.2010.04.004

Vanella M, Piomelli U, Balaras E. 2008. Effect of grid discontinuities on large-eddy simulation statistics and flow fields. *Journal of Turbulence*. **9**: 1-23, doi: 10.1080/14685240802446737

Vardoulakis S, Fisher BEA, Pericleous K, Gonzalez-Flesca N. 2003. Modelling air quality in street canyons: a review. *Atmospheric Environment*. **37**: 155-182, doi: 10.1016/s1352-2310(02)00857-9

Von Kármán T. 1931. *Mechanical similitude and turbulence.* National Advisory Committee for Aeronautics: Washington, USA.

Wallace JM, Hobbs PV. 2006. *Atmospheric science: an introductory survey. 2nd.* Academic press: Canada.

Walton A, Cheng AYS. 2002. Large-eddy simulation of pollution dispersion in an urban street canyon - Part II: idealised canyon simulation. *Atmospheric Environment*. **36**: 3615-3627, doi: 10.1016/s1352-2310(02)00260-1

Weinbrecht S, Mason PJ. 2008. Stochastic backscatter for cloud-resolving models. Part I: Implementation and testing in a dry convective boundary layer. *Journal of the Atmospheric Sciences*. **65**: 123-139, doi: 10.1175/2007jas2166.1

Westbury PS, Dunn DC, Morrison JF. 2004. Analysis of a stochastic backscatter model for the large-eddy simulation of wall-bounded flow. *European Journal of Mechanics B-Fluids*. **23**: 737-758, doi: 10.1016/j.euromechflu.2004.01.003

WHO. 2015. *World health statistics 2015.* World Health Organization: Printed in Luxembourg.

Wirjadi O, Breuel T. Approximate separable 3D anisotropic Gauss filter. *Image Processing, IEEE International Conference, 11-14 September 2005.* doi: 10.1109/ICIP.2005.1530013

Xie S, Zhang Y, Qi L, Tang X. 2003. Spatial distribution of traffic-related pollutant concentrations in street canyons. *Atmospheric Environment*. **37**: 3213-3224, doi: 10.1016/S1352-2310(03)00321-2

Xie Z-T. 2011. Modelling Street-Scale Flow and Dispersion in Realistic Winds-Towards Coupling with Mesoscale Meteorological Models. *Boundary-Layer Meteorology*. **141**: 53-75, doi: 10.1007/s10546-011-9629-x

Xie Z-T, Castro IP. 2008. Efficient generation of inflow conditions for large eddy simulation of street-scale flows. *Flow Turbulence and Combustion*. **81**: 449-470, doi: 10.1007/s10494-008-9151-5

Xie Z-T, Castro IP. 2009. Large-eddy simulation for flow and dispersion in urban streets. *Atmospheric Environment*. **43**: 2174-2185, doi: 10.1016/j.atmosenv.2009.01.016

Xie Z, Voke P, Hayden P, Robins A. 2004. Large-eddy simulation of turbulent flow over a rough surface. *Boundary-Layer Meteorology*. **111**: 417-440, doi: 10.1023/b:boun.0000016599.75196.17

Xie ZT, Castro IP. 2006. LES and RANS for turbulent flow over arrays of wall-mounted obstacles. *Flow Turbulence and Combustion*. **76**: 291-312, doi: 10.1007/s10494-006-9018-6

Zhong J, Cai X-M, Bloss WJ. 2015. Modelling the dispersion and transport of reactive pollutants in a deep urban street canyon: Using large-eddy simulation. *Environmental Pollution*. **200**: 42-52, doi: 10.1016/j.envpol.2015.02.009

Zidikheri MJ, Frederiksen JS. 2009. Stochastic subgrid parameterizations for simulations of atmospheric baroclinic flows. *Journal of the Atmospheric Sciences*. **66**: 2844-2858, doi: 10.1175/2009jas3036.1